POLITECNICO DI TORINO

Master of Science's Degree in Aerospace Engineering

Accademic year 2020/21

Master Thesis

Preliminary design of deployable Martian habitat made by innovative material

Politecnico di Torino

1859

CoRe

Polytechnic rapporteur
Giacomo Frulla
Polytechnic co-rapporteur
Enrico Cestino

CoRe external supervisors
Nicola Giulietti
Eugenio Fossat

Student
Alessio Piccolo

Dedicated to my parents

Summary

In the history of space exploration, human beings always thought about how to expand over the Earth's horizon. The limits were a lot but the way to go over them was always found. The structures created since the beginning were a complex of engineering and imagination that put in great difficulty the realization. Mars was obviously the next step for human beings since the first step on the Moos. The goal of this thesis is to suggest an easy solution for a structure for the future colonization of extraterrestrial places. A habitat for humans in future missions is necessary to put a start for a colony. This easy solution is proposed by using an innovative material called MadFlex, which has the incredible behavior to be rigid on a side and flexible on the other one, allowing the production of a structure that can be compacted and then deployed. This job focuses on the structural aspect of a Martian habitat analyzing the feasibility of the proposal with different load conditions, how to shield the astronauts from the extreme envirornment, the overall volume and total mass.

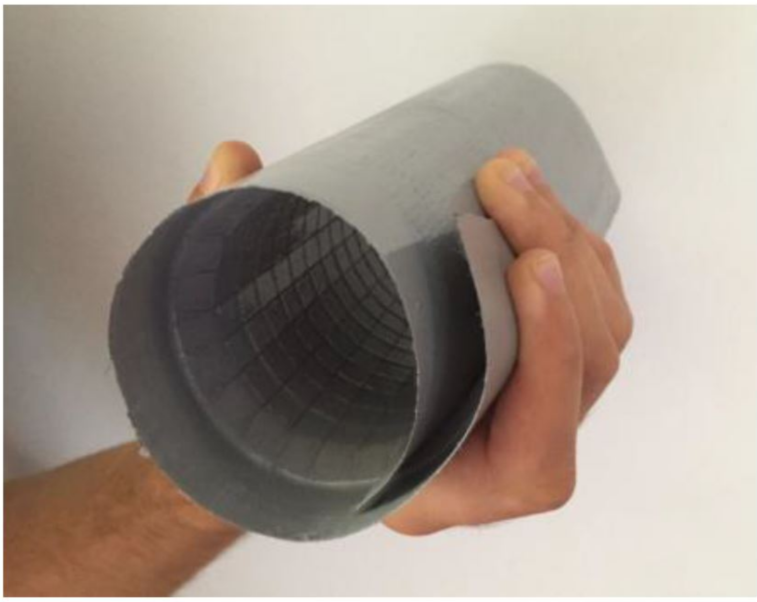

List of Figures

List of Tables

Contents

Chapter 1

The Red Planet

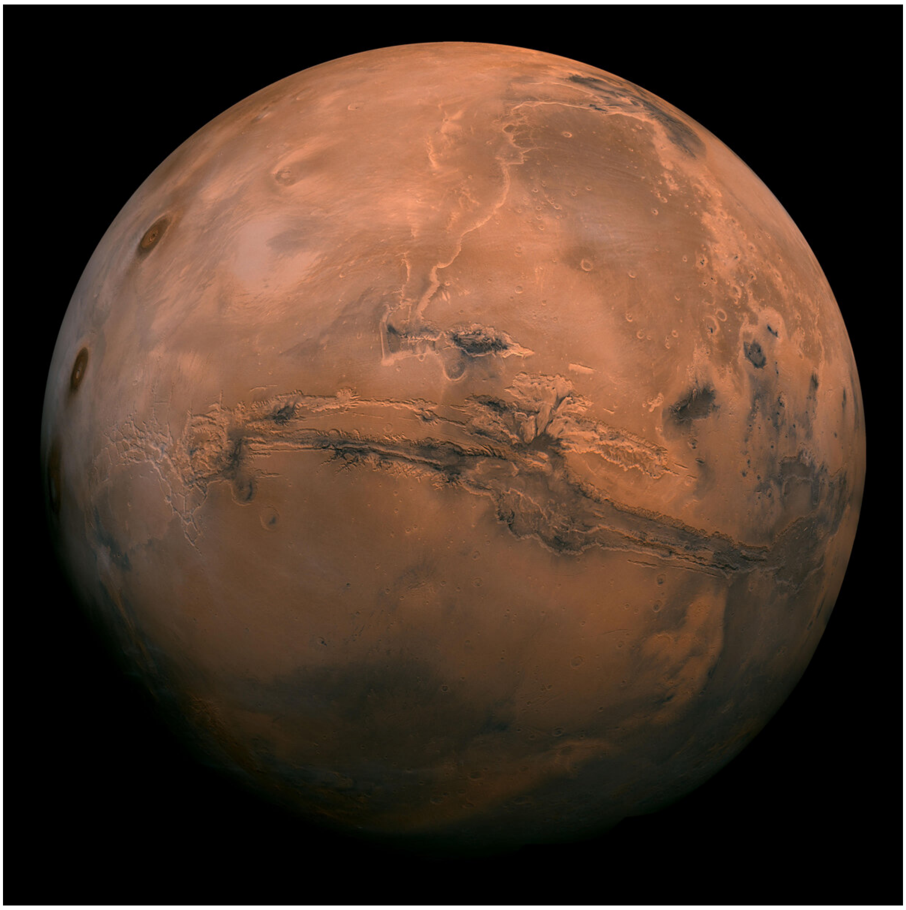

Figure 1.1: Mars. (Image Credit: NASA/JPL-Caltech)

Subsequent to the United States successfully landed humans on the Moon, there were debates at NASA that promoted sending humans to Mars by the mid-1980s. Given the intense speed at which the Moon landings were achieved, this purpose didn't seem all that bizarre. In the decades that followed, several Mars designs have been developed but none have completely emerged. Mars is an evident target for exploration because it is nearby in our Solar System, but there are many more incentives to explore the Red Planet. The precise reasons for advancing to Mars can be summed by the research for life, understanding the surface and the planet's evolution, and planning for future human exploration. The presence of life beyond Earth is a fundamental question of humankind. Mars is an excellent place where look for life, especially for its similar characteristic to Earth, in the entire Solar System. There is the suggestion that Mars once was full of water, warmer and with a thicker atmosphere, making it a probably habitable place. Given serious climate change, the planet changed drastically. But there is interest in the history of water to understand how life could have survived. Costs and risks for human exploration on Mars were huge so robotic missions gave a good alternative to substitute astronauts in studying the planet. Before sending astronauts it is important to understand the hazard, but the day that the first man will walk on Mars is close and for that day is important to have a habitat where to live safely.

1.1 Mars environment

With a radius of 3389 km, Mars is the seventh-largest planet in our solar system and nearly half the diameter of Earth. Its gravity acceleration, on the surface, is 37.5% of Earth's which means 3,711 m/s^2. Mars revolves on its axis every 24.6 Earth hours, defining the length of a Martian day, called "*sol*" (short for "*solar day*"). Mars's axis of rotation is tilted 25.2° relative to the plane of the planet's orbit round about the sun, which helps give Mars seasons like those on Earth. So the hemisphere tilted closer to the sun experiences spring and summer, while the hemisphere tilted away gets autumn and winter. At two specific moments annually, referred to as the equinoxes, both hemispheres receive equal illumination, so an identical mechanism as on our Earth.

But for diverse causes, the seasons on Mars are different from those on Earth. For one, Mars is on medium about 50% distant from the sun than Earth is, with an average orbital distance of 228 million *km*. This implies that it requires Mars longer to complete a single orbit, extending out its year and the lengths of its seasons. On Mars, a year persists 669.6 sols or 687 Earth days, and a single season can last in time 194 sols, or just over 199 Earth days.

Furthermore, the angle of Mars's axis of rotation changes much more frequently than Earth's, which has led to fluctuations in the Martian climate on timescales of thousands to millions of years. Besides, Mars's orbit is less circular than Earth's, which indicates that its orbital velocity varies moreover a Martian year. This year-long variation influences the timing of the red planet's solstices and equinoxes. As consequence, the northern hemisphere's spring and summer are longer than autumn and winter.

1.2 The atmosphere

As indicated in [1] the Martian atmosphere is about 100 times thinner than Earth's, and it is 95% CO_2. Here's a breakdown of its composition, according to a NASA fact sheet [2]:

- Carbon dioxide: 95.32%
- Nitrogen: 2.7%
- Argon: 1.6%
- Oxygen: 0.13%
- Carbon monoxide: 0.08%
- Plus, minor quantities of: water, nitrogen oxide, neon, hydrogen-deuterium-oxygen, krypton and xenon

1.2.1 Surface Pressure

Surface pressure provides a close indication of the column-integrated mass of the atmosphere. Surface pressure has been measured by spacecraft using pressure sensors on the *Viking* and *Pathfinder* landers, and by the retrieval of CO_2 column from the orbit. Because of their precision, frequency sampling and longevity, the data reported by the two *Viking* lander pressure sensors provide the most complete idea of the variation of surface pressure, permitting the study of changes on timescales from hours to interannual. In **Fig. 1.2** it is shown the daily averaged surface pressure registred by the two Viking Landers. The difference between the two curves is due to the elevation difference, about 1.2 km, between the two landing sites. Over a Martian year, the surface pressure varies by approximately 30%, reducing due to CO_2 condensation on the ice cap at the winter pole, while rising due to CO_2 sublimation from the ice cap during the summer pole. The timing and differing amplitude of the two minima and maxima, during the year, are caused by the relative phasing of the seasons concerning the date of perihelion and aphelion in the orbit of Mars around the sun.

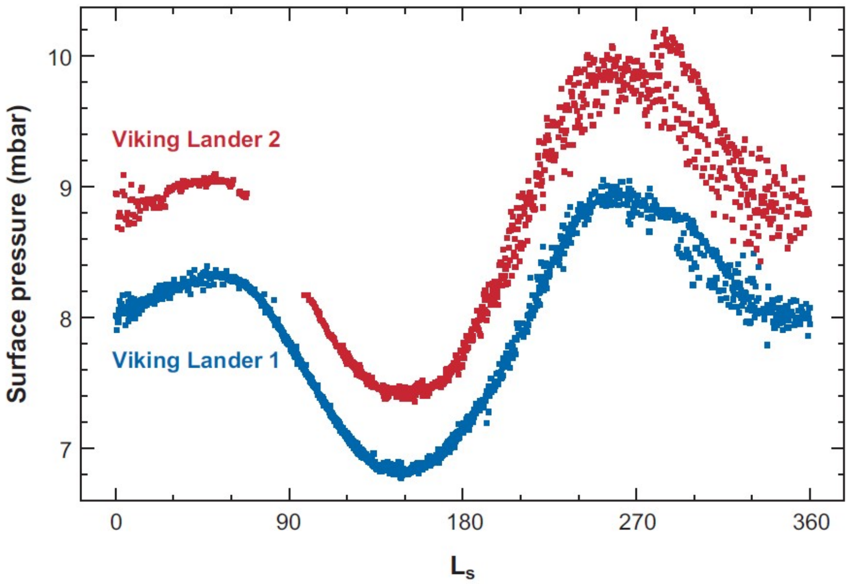

Figure 1.2: Daily averages of surface pressure (mbar) from *Viking Landers.*

On Mars, the annual dates are normally given in respect of areocentric longitude, or L_s, which represents the position of Mars in its orbit around the Sun. Ls = 0 ∘ indicate Northern Hemisphere spring equinox (Southern Hemisphere fall equinox), with L_s = 90°, 180°, and 270°, following as Northern Hemisphere summer solstice, autumn equinox, and winter solstice, sequentially. Martian months are defined as spanning 30° in areocentric longitude. Due to the eccentricity of the orbit, months are thus from 46 to 67 sols long.

In **Fig. 1.2**, the differences superimposed on the annual cycle are the result of Martian atmospheric traveling waves, comparable to the passage of storm systems on Earth. These waves are most salient in the autumn and winter seasons. Diurnal and semidiurnal solar thermal tides produce additional shifts in surface pressure on timescales of a day or less, the sunlight heats the surface and atmosphere on the dayside of the planet, letting air to expand upwards. At higher levels within the atmosphere, this excess of a mass of air then expands outward, to the edges of the planet, in order to equalize the pressure, as shown by the red arrows in **Fig. 1.3**. with the results of the lower pressure of air flows out of the mass of air felt at the surface below. As Mars rotates, this mass of air moves over the planet each day, from east to west. The amplitude of these tides has been observed to increase significantly during massive dust storms.

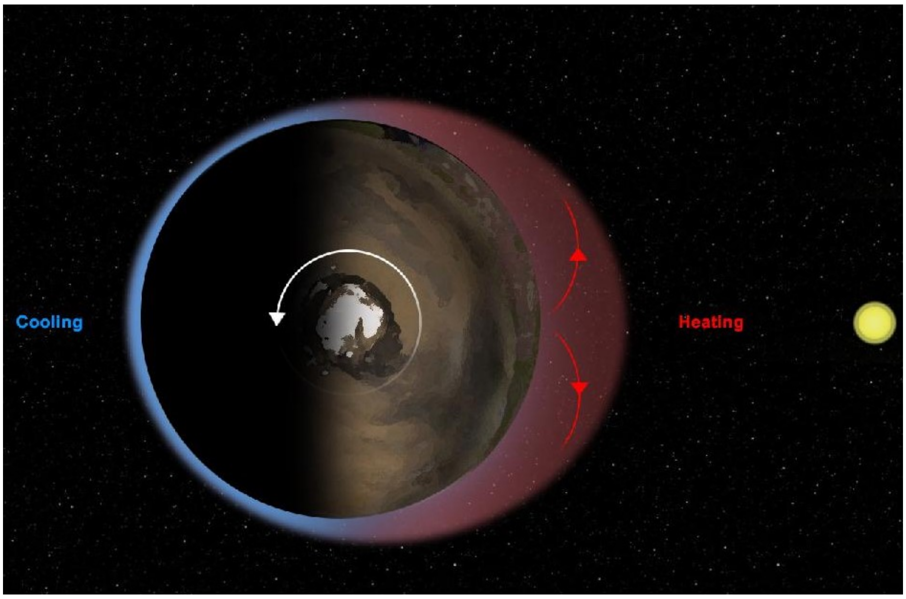

Figure 1.3: Thermal Tides at Mars (Image credit: NASA/JPL-Caltech/Ashima Research/SWRI).

1.2.2 Atmospheric temperature

Atmospheric temperature is one of the most significant measures that describe the atmospheric state, and was measured using several different observational techniques. A wide way to deduce the atmospheric temperatures is by the thermal infrared 15-micron CO_2 band. The shift in known optical depth as a function of frequency over the band is used to examine atmospheric temperatures at different layers within the atmosphere. Thermal infrared spectra from the *Mariner 9 (IRIS)*, *MGS Thermal Emission Spectrometer (TES)*, *Mars Express Planetary Fourier Spectrometer (PFS)*, and *MRO Mars Climate Sounder (MCS)* instruments have used this method to retrieve atmospheric temperature profiles. The common vertical range of sensitivity from the surface is around 40 km from a nadir viewing, and as high as 65 km with limb-geometry observations. In **Fig. 1.4**, there is an example of the differences. *Viking Orbiter Infrared Thermal Mapper (IRTM)* and *Mars Odyssey Thermal Emission Imaging System (THEMIS)* instruments allowed a single "average" atmospheric temperature representation of approximately 25 km above the surface. The benefit of thermal infrared profiling is that it lets the measurement of temperatures over a wide vertical range to be settled systematically on a global scale from a spacecraft around the planet. At moment, the best single data set was obtained by the *TES* instrument, which gave a near-continuous atmospheric temperatures profiles at two different local times (2:00 a.m. and 2:00 p.m.) daily for almost three Martian years (March 1999 to August 2004).

Fig. 1.5 shows latitude-height cross-sections acquired from daytime (2:00 p.m. local time) *TES* spectra in the four seasons, L_s = 0°, 90°, 180°, and 270°. In the cross-sections shown in **Fig. 1.5**, temperatures (represented with isotherm line) are generally found to significantly start from radiative equilibrium, indicating strong variations of the thermal structure by dynamical processes. Under solstice conditions (L_s = 90°and 270°), maximum solar heat occurs at the summer pole, and near-surface temperatures reach a maximum there. In the summer hemisphere, the temperatures at all layers increase toward the pole. In the summer hemisphere, the temperatures of all layers increase toward the pole. During the winter hemisphere, there is a really strong latitudinal gradient caused by downward motions and therefore the very cold temperatures of the polar night. The latitude area of this cold front features a characteristic inclination with the front more poleward at higher altitudes above the surface. This produces a temperature inversion at altitudes below the 1-mbar level at mid-latitudes as cold polar air is transported toward the equator near the surface. During the perihelion (L_s = 251°) near the Northern Hemisphere winter solstice (L_s = 270°) there is a significantly larger latitudinal temperature

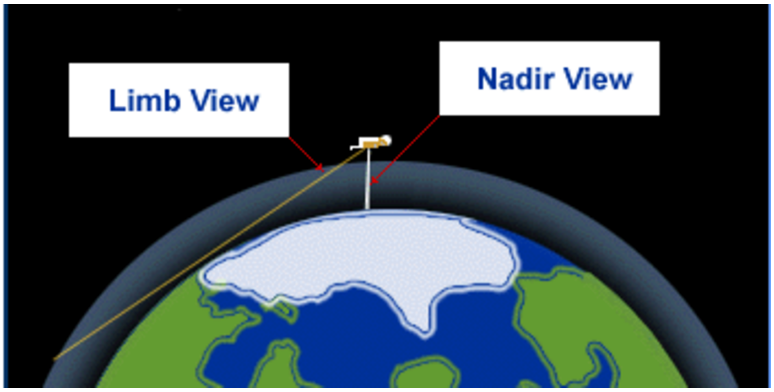

Figure 1.4: Nadir viewing and limb-geometry observation (Image credit: NASA)

.

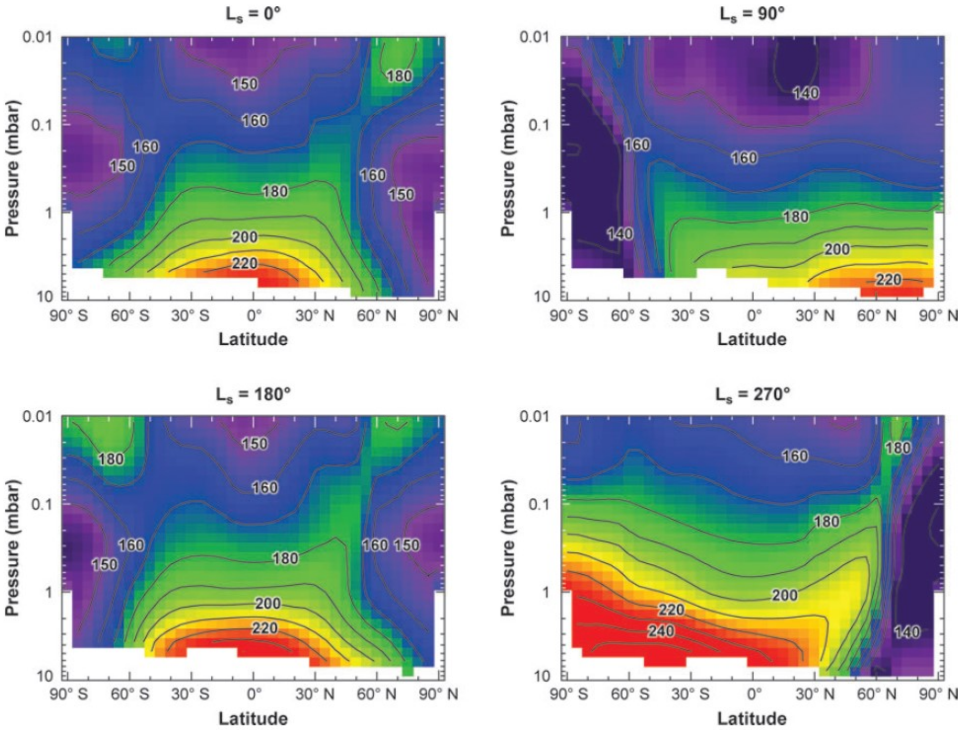

Figure 1.5: Mean temperatures as a function of latitude and pressure as observed by *TES*. (Image credit: Michael D. Smith, Spacecraft observations of the martian atmosphere)

.

gradient in winter mid-latitudes in the north than in the south (at $L_s = 90°$). It also guides to warmer temperatures overall through the Southern Hemisphere summer than through the Northern Hemisphere summer. The thermal profile during the two equinox periods ($L_s = 0°$ and 180°) is similar to each other and is almost symmetric about the equator. The warmest temperatures are approximately near the surface at the equator. In each hemisphere, temperatures decrease moving toward the pole at altitudes below 0.3 mbar (approximately 30 km). Above that pressure level (no less than the 0.01 mbar level), there is a temperature minimum at the equator and a temperature maximum at the middle to high latitudes in each hemisphere. Traveling planetary waves, solar thermal tides, and the interaction of the atmosphere with the Mars topography are the causes of temperature fluctuations. Another way to study the atmosphere temperature is by radio occultation that works by monitoring the signal sent from a spacecraft as it moves behind a planet as viewed from Earth. At both the ingress and exit points, the signal passes within the atmosphere, which both (very slightly) refracts the beam and creates a Doppler shift in the observed frequency. The vast advancement in vertical resolution obtainable using thermal infrared spectra is especially useful for examining near-surface temperatures and for determining the vertical structure of waves. The disadvantage to the radio occultation is their relatively sparse coverage in space and time, due to limitation in times and places in relation to the spacecraft orbital geometry allows an occultation.

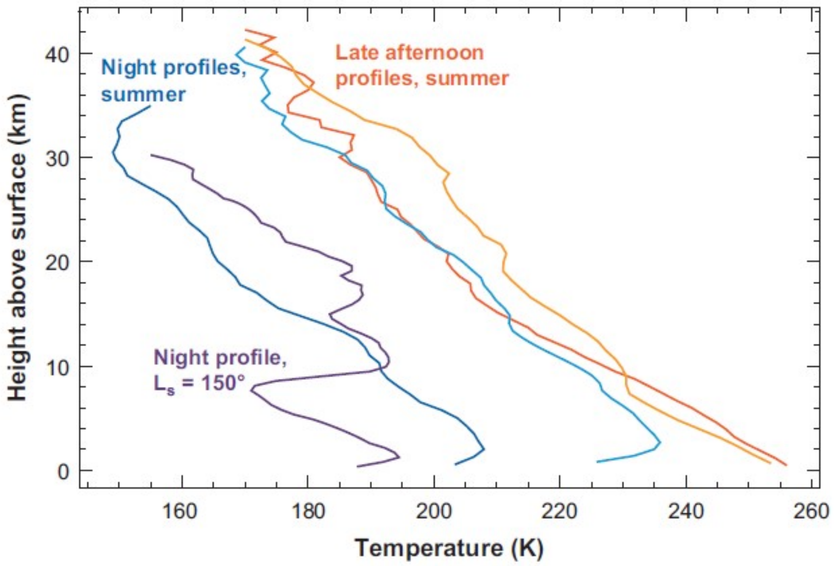

Figure 1.6: Temperature profiles related to height as derived from *MGS*. (Image credit: Michael D. Smith, Spacecraft observations of the martian atmosphere)

.

Fig. 1.6 shows temperature profiles obtained from *MGS* radio occultations. In the afternoon (red profiles), the temperatures nearly agree with the *TES* results when related to the vertical resolution of the thermal infrared profiles. At night (blue and purple profiles), the radio occultation temperature profiles permit the characterization of a near-surface inversion level, which is not apparent in *TES* profiles data. Radio occultation profiles exhibit large-amplitude waves (purple profile), which may be affected by the presence of water ice clouds. Stellar occultation, when a spacecraft observes as a star disappears or reappears from behind the horizon of Mars, has been used to obtain middle-atmospheric (50– 130 km) temperatures utilizing UV observations with the *Mars Express SPICAM* instrument. These observations are significant because of the insufficiency of data at these higher altitudes.

PBL temperatures have been measured using thermocouples mounted on the *Viking* and *Pathfinder* landers directly on the Martian surface, and have been regained from thermal infrared spectra taken by the *Mini-TES* instrument onboard the *Spirit MER* rover and planetary boundary layer (PBL) is the part of the atmosphere that directly interacts with the surface. Both the thermocouple and thermal infrared spectra measurements show a consistent diurnal pattern in **Fig. 1.7**. The atmosphere is coolest and firmly stratified before the dawn. Soon after the sunrise, the warming surface heats the atmosphere from the bottom. There is a very steep, superadiabatic vertical temperature gradient through the lowest 100 m of the atmosphere by mid-morning. Turbulent convection starts throughout this lowest layer, with temperature variations of 15 to 20 K in the lowest meter over the surface and up to 5 K under 100 m in 30–60 seconds. Turbulent convection continues until afternoon (around 16:30) when the surface becomes cooler than the near-surface atmosphere, convection stops, and the near-surface temperature gradient is inverted. The inversion layer grows during the nighttime hours in a depth of 1 km before rapidly reversing in the morning.

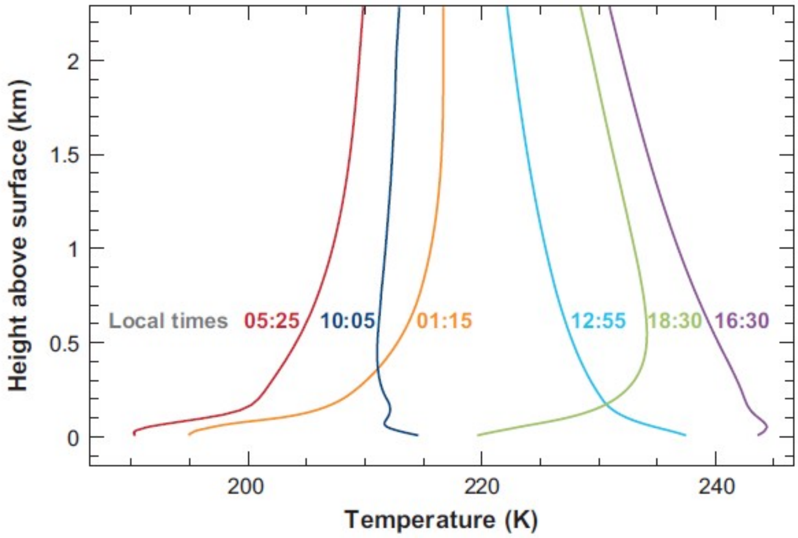

Figure 1.7: Atmospheric temperatures as a function of height from *Spirit MER* rover data. (Image credit: Michael D. Smith, Spacecraft observations of the martian atmosphere)

.

1.2.3 Atmosphere vertical structure

Temperatures decrease with height in the Martian atmosphere as they do on Earth. As shown in **Fig. 1.8**, Mars temperature rises in the troposphere, mesosphere, and thermosphere. There is no stratosphere because Mars lacks an ozone layer. The troposphere on Mars is higher compared to the one on Earth deep 12 km. From *Viking* and *Pathfinder* lander entry data, the troposphere on Mars is almost 60 km with an average lapse rate of -2.5 K km^{-1} than the lapse rate of -6.5 K km^{-1} on Earth. On both planets, the moist lapse rates are much less than the dry adiabatic lapse rate, precisely -4.3 K km^{-1} for Mars and -9.8 K km^{-1} for Earth. On Earth is because of the latent heat release correlated to the condensation of water vapor. On Mars, the extra heating comes from the engrossment of solar radiation by suspended dust particles. On both planets, vertical heat fluxes associated with large-scale circulation systems stabilize the temperature. Above 15 km from the surface, temperatures decrease with height, but are regulated almost completely by radiation rather than convection. In the mesosphere, temperatures are nearly constant. In the thermosphere, as on the Earth, temperatures rise due to the heating absorption of solar radiation in the far and extreme ultraviolet part of the spectrum as reported in [3].

1.2.4 Winds and dust storms

There are few direct measurements of wind on Mars. *Viking landers* and *Pathfinder* were provided with hot-wire anemometers that measured wind speed and direction. *Pathfinder* also had a set of three windsocks mounted at different heights to measure wind direction. From these observations typical near-surface wind speeds vary in a range from 0–10 m/s, with a daily rotation of the wind direction due to the sequence of downhill drainage flow and the solar thermal tide. Wind speeds are usually light in the night and rise with maximum values during the morning. Also, gusts were registered with higher speeds. From the orientation and movement of distinct clouds and with the orientation of surface eolian features it was possible the estimation of wind velocity. However, this estimation is seriously limited due to the sporadic appearance of clouds and the difficulty of cloud height calculation. The connection between winds and the structure of eolian features is not completely clear and may only reflect the winds during specific seasons. A better indirect estimation of wind speeds is by gradient balance, combining latitudinal

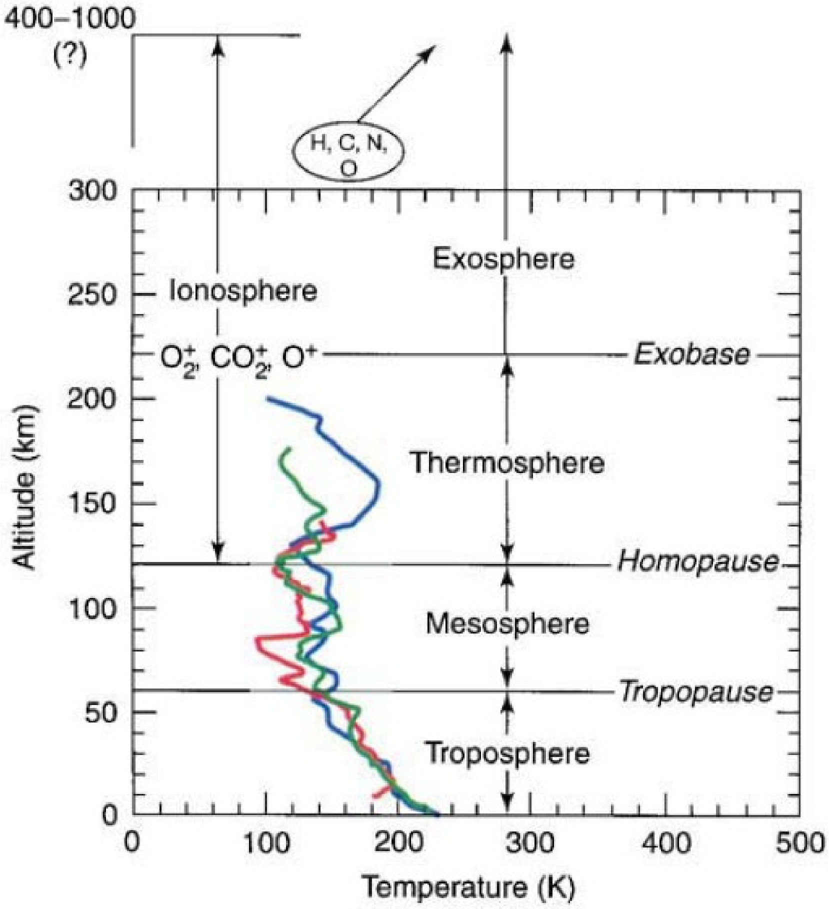

Figure 1.8: Vertical structure of the Martian atmosphere. Colored curves are temperatures entry data aboard the *Viking 7* (blue), *Viking 2* (green), and *Pathfinder* (red) landers. (Image credit: R M Haberle. Planetary atmospheres).

gradients in the thermal structure with vertical gradients in local wind speed assuming equilibrium between horizontal pressure gradient force, the Coriolis force, and centrifugal forces. The problem with the gradient wind method is the requirement of a boundary condition on the local wind speed, generally imposed zero at the surface. In solstice conditions, the latitudinal gradient in temperature between the warm mid-latitudes and the cold winter polar night generates a strong eastward jet, reaching speeds of 100 m/s, generally called polar vortex. In the summer hemisphere winds are usually light and westward. The polar vortex in the Northern Hemisphere winter (L_s = 270°) is more powerful than the one during Southern Hemisphere winter.

Dust aerosols are a constant presence in the Martian atmosphere. This significantly influences the thermal structure of the atmosphere and drives the atmospheric circulations. MGS observed dust optical profundity for three Martian years with thermal infrared spectra from TES and daily images from the *Mars Orbiter Camera* (MOC). At present, spacecraft continue to observe dust aerosols. Observations of the Sun from the surface of Mars by the *Viking landers* and *Pathfinder lander* gave dust optical profundity at the two lander sites. The data collected by all the instruments aboard spacecrafts had given a good overview of the dust cycle in the current Martian climate. The orbiter investigations show a clear seasonal pattern of dust storms. In the annual cycle, there is the intermittent occurrence of regional, or planetary-scale, dust storms and it can take a couple of months for the dust to settle out back to a nominal level. The largest dust storms happen almost only during the dusty season between L_s = 180°–360°when the whole surface and atmospheric temperatures are most heated. In **Fig. 1.9** a visible wavelength images taken by the *MGS Mars Orbiter Camera* show just before and near the height of the 2001 planetary-scale dust storm.

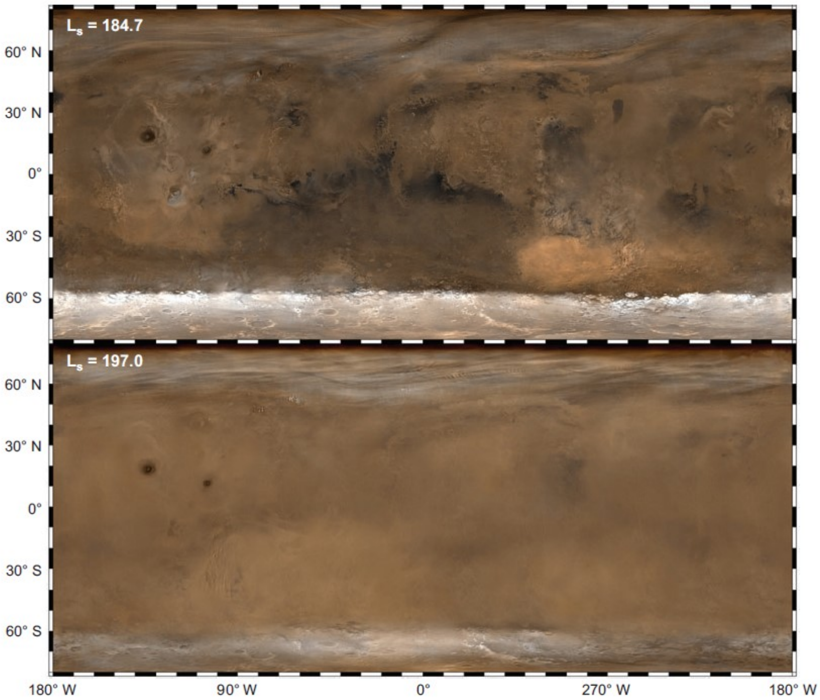

Figure 1.9: The top images were taken just before the planet-encircling dust storm event of 2001 while the bottom represents the moment at the height of the dust event. (Image credit: NASA).

This kind of dust storms happen at random intervals that average about once every three Martian years. Regional-scale dust storms happen every Martian year in the dusty season, especially near L_s = 225°and 315°, with cross-equatorial flushing dust storms and typically last a few weeks. Smaller, local-scale dust storms do occur during the year and related to either topographic features, such as *Valles Marineris*, or the retreating edge of the seasonal polar ice cap in the spring for both hemispheres. The opposite, clear season (L_s = 0°–180°) is marked by a much lower level of dust optical depth with no very large dust storms.

Additionally to dust, aerosols in the form of condensate clouds frequently form on Mars. The condensate clouds are made up of water ice and CO_2 ice. The global transport of water vapor is altered by the ice clouds with the water cycle, and their location is often indicative of regions of upward-moving air. The nucleations of water ice aerosols on dust particles also appear to purify the atmosphere of dust and to drop water ice and dust to the surface in the polar regions. There are many forms of water ice clouds and it is observed to be caused by the topographic features of the surface during the aphelion season between L_s = 40°–140°. Since large dust storms form preferentially during the dusty period, in perihelion season (L_s = 180°–360°), the biggest extent of water ice clouds does occur during the colder aphelion season (L_s = 0°–180°) and in the polar regions in the winter hemisphere. The formation of the cloud belt begins around L_s = 0°, reaching the maximum intensity and spatial coverage at L_s = 80°. At L_s = 140°, the cloud belt quickly dissipates due to the atmospheric temperatures rising, although clouds over the volcanoes remain for the vast majority of the year. The other cloud features are the polar covering that forms over the polar regions in the winter hemisphere , with the one over the northern polar is much more extensive than the southern polar one, reaching down to nearly 30°N latitude at its greatest extension.

1.3 Marsquakes and meteorite impacts

Quakes on earth happened many times a day, largely due to continental plates shifting as they float on the mantle below and that's called plate tectonics. Mars does not seem to have plate tectonics, but other things can make the ground shake too, like cracking caused by contraction from the planet cooling and magma moving from the center of the planet and creating pressure deep underground. Meteorite impacts generate a kind of seismic waves around and through the planet with the possibility to study how those waves bounce off layers deep underground to help understand what a planet's interior is like. The *NASA InSight* mission to Mars expects to use seismology to understand the structure and how Mars formed. To achieve this, InSight is equipped with the *Seismic Experiment for Interior Structure* (SEIS).

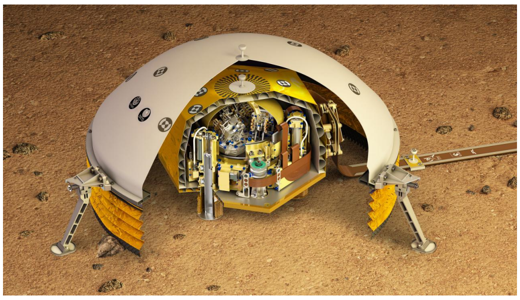

Figure 1.10: Cutaway illustration showing InSight's SEIS (Image credit:NASA/JPL-Caltech/CNES/IPGP).

When an asteroid smashes on our planet, it first encounters dense layers of the atmosphere at more than 10 km/s. Air friction causes considerable heating up, and most are completely vaporized before they touch the ground. When an impacting body descends, it produces an acoustic shock wave that propagates and strongly hits the ground, leaving a visible trace on seismographs. If the impacting body survives in the atmosphere and remains partially integer, it reaches the surface and creates a crater. New shock waves are generated by the collision, and it is a different phenomenon from the atmospheric blast, but also important to study. The described mechanism changes with the nature of the planet. On Mars, these meteorites produce a shock wave that propagates in the atmosphere but also different seismic waves and a consequent crater due to the impact. The energy from the impact could travel a long distance over the surface being an advantage for the study of the internal structure of Mars. Small impacts are statistically more numerous and they generate craters of a few meters in diameter. An impact related to a crater of 100 m in diameter, on Mars, occurs roughly every 10 years. It is therefore probably that *InSight* will see such an event during its stay on Mars. On the other hand, it must count on much smaller impacts that will only help to understand the near-surface structure between the lander and the crater [4].

1.4 Mars magnetic field

It is known that Earth's magnetism comes from its core, where molten, electrically conducting iron flows below the crust. The generated magnetic field is global and it surrounds the entire planet. Considering that Mars is a rocky, terrestrial planet like Earth, it is normal to assume that there is the same kind of phenomena there too. Nevertheless, Mars does not create a magnetic field on its own.

The formation of a magnetosphere does occur when a flowing plasma (for example, the solar wind) deflects around an object of planetary dimension, due to the presence of a magnetic field and the associated currents induced in the interaction. Induced currents form in both intrinsic and induced magnetospheres but the intrinsic magnetic fields of intrinsically magnetized planets (such as the Earth, with a melted core) govern the nature of the interaction and the establishment of the resulting current systems. Due to the lack of Earth-like global magnetic field dipole, the Martian upper atmosphere is ionized by X-rays coming from the sun and extreme ultraviolet radiation. Because of that, the ionosphere is a highly conductive obstacle to the magnetized solar wind plasma flow. Induces electric currents in the ionosphere are created by the interaction, and in consequence to that, they create sufficient magnetic pressure to reduce speed, shock-thermalize and deflect the solar wind around the ionosphere, creating an induced magnetosphere. Recent studies have proved the Martian induced magnetosphere to be an efficient screen for the ionosphere, even more than the Earth's intrinsic magnetosphere. There is also enough energy to escape Martian gravity potential and create an induced magnetotail behind the planet, as shown in **Fig. 1.11**.

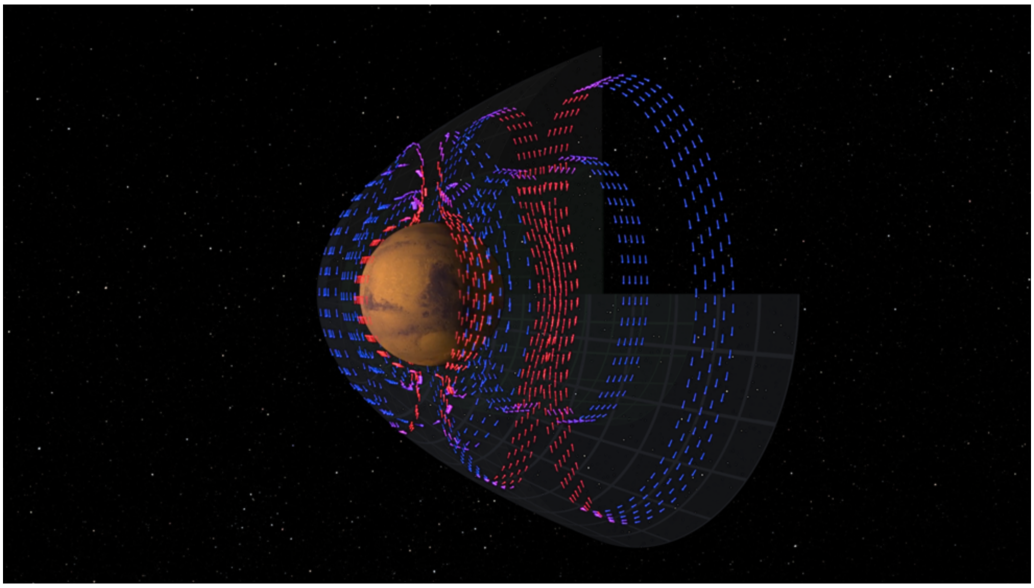

Figure 1.11: Scientific visualization of the electric currents around Mars. (Image credit: Credits: NASA/Goddard/MAVEN/CU Boulder/SVS/Cindy Starr).

This atmospheric ion escape is also linked to the gradual reduction of volatiles and greenhouse gases and the collapse of the water cycle. The absence of a global magnetic field around Mars, let the currents induced in the solar wind to form a direct electrical connection to the upper atmosphere of Mars. The energy from the solar wind is converted into magnetic and electric fields that accelerate the charged particles in the atmosphere letting them escape into outer space.This process permitted the transformation, for billions of years, of Mars from a heated and humid able to host life into the cold desert nowadays known [5].

1.5 Mars soil

On July 4, 1997, *Pathfinder* landed at the mouth of Ares Vallis. The Alpha-Proton-X-ray-Spectrometer (APXS) was activated on the first day on Mars to study the atmosphere and soil properties. During the 83 days on Mars, until radio contact was lost, Sojourner encircled the lander within a 12 m radius. Through this time the sensor of APXS was located on 9 rocks and on soils at 7 locations. Though, mainly because of electronic noise, not all of the acquired data were useful. These instrumentations made chemical analyses of Martian rocks for the first time. *Viking* Landers 1 and 2 only made in-situ X-ray fluorescence (XRF) analyses of soil, as no rocks were in the range of the arms.

The spectrometer's sensor, **Fig. 1.12**, simply had to be put on the sample in order to irradiate it with α particles emitted by ^{244}Cu sources. There are three modes of operation: 1. Alpha-back-scattering (Rutherford scattering). α particles energy scattered by about $180\circ$ is a direct measure of the mass of the nucleus on which the scatter happens, 2. In rare cases the nuclei of the target experience α-proton reactions. The protons emitted have specific energies to the target nucleus. This mode requires counting times to compete with the other two modes for accuracy. 3. The α particles additionally interact with the electron shell of the target nuclei generating X-rays that are analyzed. The alpha-back-scatter mode is very useful to find elements like C, N and O, while the X-ray mode is helpful for all elements heavier

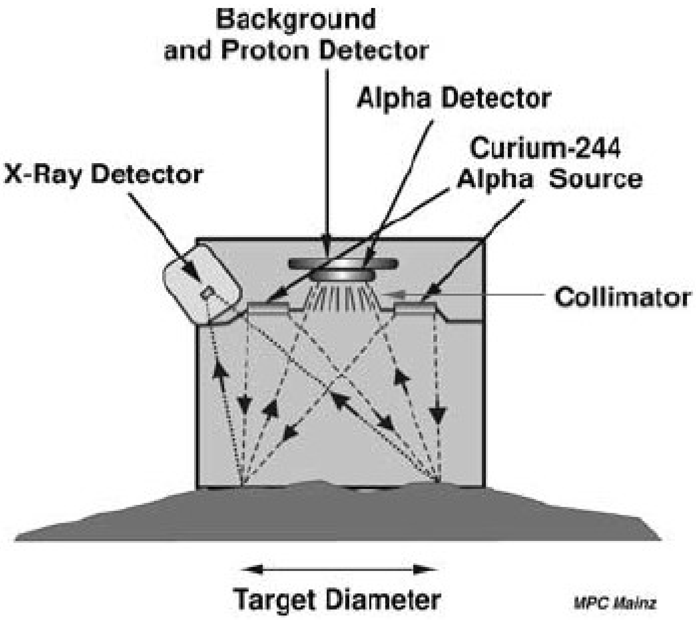

Figure 1.12: APXS sensor head. (Image credit: H. Wanke, CHEMICAL COMPOSITION OF ROCKS AND SOILS AT THE PATHFINDER SITE)

than Na. All measurements were performed with a sampled area of 50 mm in diameter. The depth of analysis is generally in the order of a few µm. All elements, except H, were analyzed. **Fig. 1.13** shows the X-ray spectra taken from the dark soil of the Mermaid Dune and the rock Half Dome, this was possible thanks to the mobility of the rover [6].

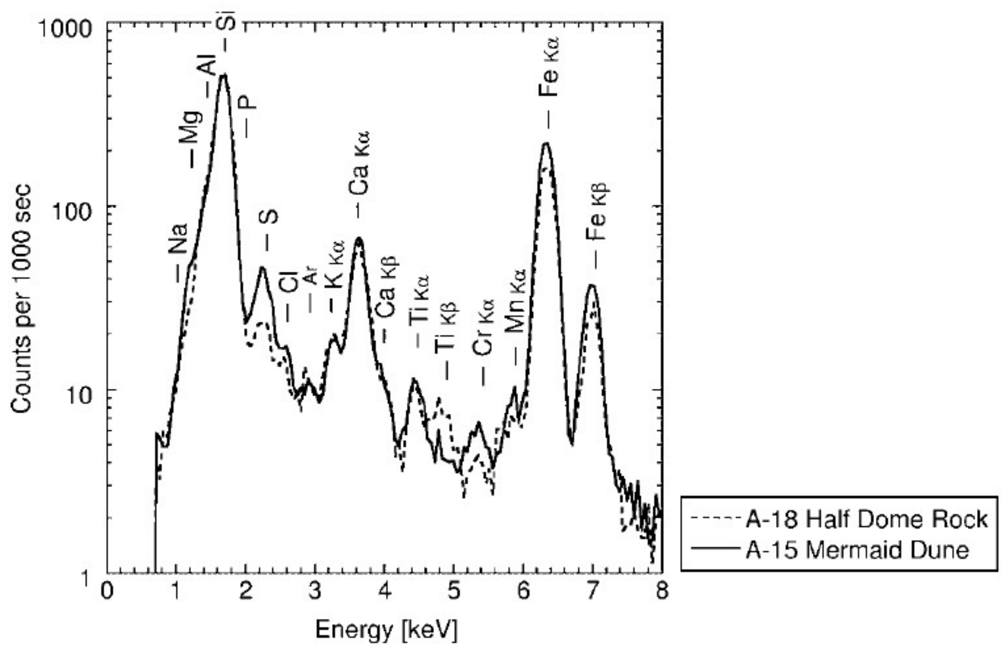

Figure 1.13: X-ray spectra of rock Half Dome and the dark soil of Mermaid Dune. The Ar peak is due to the 1.6% Ar in the Martian atmosphere within the APXS sensor head. (Image credit: H. Wanke, CHEMICAL COMPOSITION OF ROCKS AND SOILS AT THE PATHFINDER SITE)

Minor revisions due to more accurate recalibrations lead to higher Fe concentrations for all samples by ∽25%, while the Si concentration was reduced by ∽10%. In the case of K, emerging to the left of the Ca peak, a considerable mistake was recognized in the separation procedure of the two peaks. The data recorded in figure are the corrected ones.

Sample	Na_2O	MgO	Al_2O_3	SiO_2	P_2O_5	SO_3	Cl	K_2O	CaO	TiO_2	Cr_2O_3	MnO	Fe_2O_3
A-4 soil	1.00	9.95	8.22	42.5	1.89	7.58	0.57	0.60	6.09	1.08	0.2	0.76	19.6
A-5 soil	1.05	9.20	8.71	41.0	1.55	6.38	0.55	0.51	6.63	0.75	0.4	0.34	23.0
A-10 soil	1.32	8.16	7.41	41.8	0.95	7.09	0.53	0.45	6.86	1.02	0.3	0.51	23.6
A-15 soil	0.97	7.46	7.59	44.0	1.01	6.09	0.54	0.87	6.56	1.20	0.3	0.46	23.0
Mean Soil	1.09	8.69	7.98	42.3	0.98	6.79	0.55	0.61	6.53	1.01	0.3	0.52	22.3

Table 1.1: Composition of soils and rocks at the Mars PF landing site.

Tab. 1.1 contains the data of the soil samples A4, A5, A10, and A15. All data were normalized to 100%, though in some cases the sums give only about 80% because of inadequate positioning of the APXS sensor head. The chemical composition of all the soil samples was almost identical, even if the color and appearance on the ground were different. All the soil composition at Ares Vallis was very comparable to the landing sites of *Viking* 1 and 2 landers at Chryse and Utopia. This lead to the idea that the Martian soil is homogeneous on a global scale, probably having been spread and mixed by impacts and storms. Carbonates should not be suspected in the Martian soil because of the abundance of SO3.

Shergottites, the most abounding group of Martian meteorites, contain mantle-derived concentrations of ∽200 ppm H_2O, ∽100 ppm CO_2, and between 1200 and 5600 ppm SO_2. Terrestrial MORB contains ∽2000 ppm H_2O and similar concentrations of SO_2 and CO_2. On Mars, which is much more impoverished in H_2O and CO_2 but similar or richer in SO_2, it is suspected that SO_2 dominates the volcanic gases. At least part of SO_2 will be immediately transformed into SO_3, which combined with water vapor will produce sulfuric acid which will decompose carbonates and return CO_2 to the atmosphere [6]. The parameters used to describe the mechanical properties of the regolith from the *InSight* landing site are now considered. The Martian regolith is suspected to be a combined mix of weathered, indurated, and windblown material. Matching with data from other landed missions and orbiters shows that the regolith is principally cohesionless, has an angle of internal friction near to that of sand (30–40°), and particles are presumed to be rounded due to erosion by wind. Surely, eolian activity on Mars has occurred during geologic time. The surface layer has encountered eolian activity and impacts: after each impact sand-size grains have been blown up, rounded and sorted, and the entire material has rounded (sub-rounded) grains. The values of thermal inertia (200 J/(m^2 K $s^{1/2}$)), albedo (0.25) and dust cover index (0.94) estimated by *InSight* and based on correlation with the thermal inertias of previous landing sites, indicate that surfaces are composed of cohesionless sand or low cohesion soils with particle sizes of ∽ 0.15–0.25 mm. In summary, the first 5 m of regolith at the landing site supposed to be dominantly formed of nearly cohesionless fine basaltic sand, which includes few rocks.

Physical properties of regoliths, like thermal conductivity, seismic velocity, penetration resistance, shear strength, compressibility and dielectric constant, are a function of bulk density, which is related to grain size, grain shape, particle surface composition and grain arrangement. In dust powders, due to electrostatic forces effects densities can be as low as 1000 kg/m^3; in fine sand, inter-particle forces are principally ruled by gravity and inter-granular friction, resulting in higher densities. However, the lower gravity on Mars could likely result in looser arrangements of grains of the same shape and size distribution, related to the gravity on the earth. Possible values of the regolith density can be estimated considering typical features of granular assemblies and sands, together with the physical properties of some terrestrial sands and regolith simulants. Simple first order calculations can be obtained from geometrical considerations of arrangements of spherical particles of the same diameter. In the densest possible arrangement (tetrahedral), with a minimum void ratio $\epsilon_{min} = 0.351$, with terrestrial sands, usually composed of quartz fragments with a density of 2670 kg/m^3, this value corresponds to a maximum bulk density of 1980 kg/m^3, a high density for (non-basaltic) sands on Earth. For basaltic sands, as on Mars and in some regions on the earth, the resulting density would be 2230 kg/m^3 with a grain density of 3310 kg/m^3 for basalt. On the other hand, the most disadvantaged possible assembly of spheres (simple cubic) has a maximum void ratio $\epsilon_{\ max} = 0.908$, leading to a minimum bulk density of 1400 kg/m^3 for quartz sands and of 1580 kg/m^3 for basaltic sands. For non-spherical grain shapes, other shapes are possible anyway. On the Moon, regolith density increases in a drastic way at depths below 20 cm. This increase is related to the effects of continuing small meteoroid impacts, for the absence of the atmosphere. Best estimates give typical densities values from 1450 to 1550 kg/m^3 at depths between 0 and 15 cm and 1690 to 1790 kg/m^3 at depths between 30 and 60 cm. The situation is quite different on Mars because micrometeorites are destroyed by the atmosphere. The primary superficial processes are wind transport and saltation of regolith particles. In natural sands, a non-uniform grain size distribution gives compacter arrangements, with smaller grains in the voids between larger grains, if they are enough spherical. This is supposed to be the case for the *InSight* landing site, with surface densities calculated to be around 1300 kg/m^3 [7].

1.5.1 Regolith Elastic Properties

Thanks to the SEIS (Seismic Experiment for Interior Structure) instrument, calculation of elastic properties was possible and the procedure, reported in [7], to calculate them it is now reported. Poisson's ratio ν can be derived from compressional wave velocity v$_P$ and shear wave velocity v$_S$ these velocities. In compressional waves, the particle motion is in the direction of propagation. In shear waves, the particle motion is perpendicular to the direction of propagation. Elastic modulus E can be formulated in terms of the above quantities and density ρ. Poisson's ratio ν is the relation between transverse strain $\epsilon_\perp$ and axial strain $\epsilon_\parallel$ when uniaxial stress is applied

$$\nu = -\frac{d\epsilon_\perp}{d\epsilon_\parallel} \tag{1.1}$$

Considering the static elastic deformation of materials in the stress-strain relationship, and by adding the dynamic behavior it is possible to calculate the velocity of elastic waves, v$_P$ and v$_S$, through materials

$$v_P = \sqrt{\frac{E(1-\nu)}{\rho(1-2\nu)(1+\nu)}} \tag{1.2}$$

$$v_S = \sqrt{\frac{E}{\rho 2(1+\nu)}} \tag{1.3}$$

Then, Poisson's ratio linked to the seismic P- and S-wave velocities v$_P$ and v$_S$ by

$$\nu = \frac{(\frac{v_P}{v_S})^2 - 2}{2((\frac{v_P}{v_S})^2 - 1)} \tag{1.4}$$

There are no in situ measurements of seismic velocities of the Martian surface yet. Estimates thus have to be done in the laboratory with experiments using analog materials on Earth, also considering field and lab data gathered for lunar regolith and terrestrial sands. Both v$_P$ and v$_S$ were decided for three Martian regolith soil simulants under various confining pressures corresponding to lithostatic stresses from 5 m to more than 60 m depth on Mars. The Mojave simulant, given by JPL, is a mix of MMS simulant, including alluvial sedimentary and igneous grains from the Mojave Desert, with basaltic pumice. The Eifelsand simulant from DLR is a mix of smashed basalt and volcanic pumice sand. The MSS-D simulant, also from DLR, is artificial sand made of a 50/50 mix of smashed olivine and quartz sand, with a bimodal grain-size distribution, and olivine particles tinier than presumed at the *InSight* landing site. The ejecta that forms the Martian regolith are expected to be rounded due to long term exposure to wind action in low atmospheric pressure conditions. The Mojave simulant includes both rounded and more angular grains and their particle dimension distribution is closer to the landing site estimates. The Poisson's ratio ν calculated via (1.4) accordingly is 0.22.

From Hooke's law, the elastic or Young's modulus E expresses the ratio between uniaxial tensile stress σ and the proportional deformation, ϵ, and consequently the stiffness of a material:

$$\sigma = E\epsilon \tag{1.5}$$

It can also be formulated as a function of the shear wave velocity v_S , Poisson's ratio ν and density ρ as

$$E = 2(v_S)^2\rho(1+\nu) \tag{1.6}$$

Depth profiles of Young's modulus for the three distinct models of regolith compaction are shown in **Fig. 1.14**.

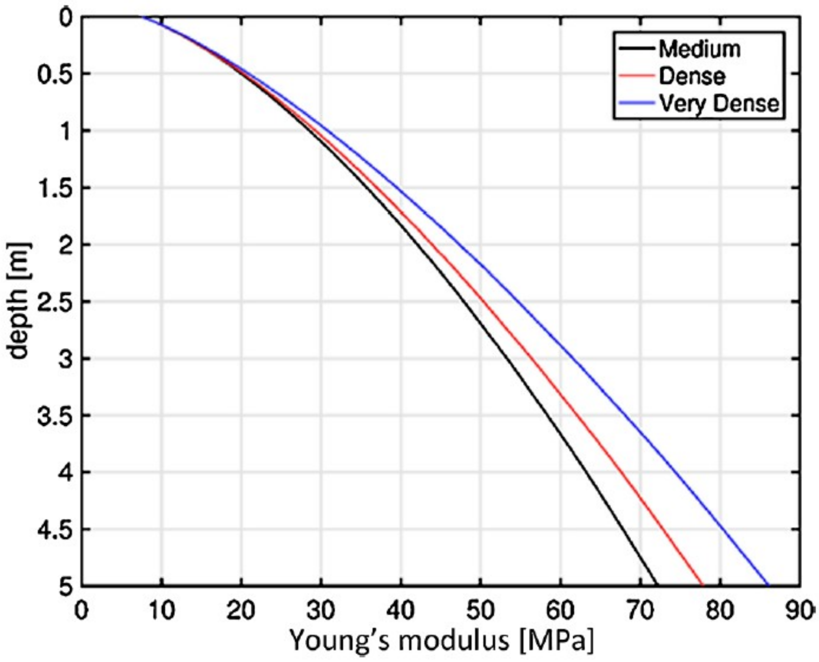

Figure 1.14: Models of Young's modulus as a function of depth for the upper five meters of regolith at the InSight landing site. (Image Credit: Paul Morgan, A Pre-Landing Assessment of Regolith Properties at the InSight Landing Site)

1.6 Mars radiation environment

1.6.1 Ionizing radiation

An introduction to ionizing radiations will be discussed before the description of the radiation environment on Mars. This type of radiation is capable to remove an electron from atoms or molecules, so with energy equal to or higher than the energy of first radiation, the energy necessary to remove an electron from a single atom. The ionizing radiations could be composed of electromagnetic waves, subatomic particles, or ions. The electromagnetic waves able to be ionizing radiation are those located in the higher energetic part of the electromagnetic spectrum. X-ray, γ-rays and high-frequency ultraviolet rays are ionizing radiations, though the low-frequency ultraviolet, infrared, microwaves, and radio waves are radiations with no ionizing power. But there is not a specific value that differences these two groups, due to the dependence on the energy of first radiation that varies in function of the type of atom considered. A conventional value for this energy is between 10 eV and 33 eV for a photon. Other natural ionization particles are muons, mesons, and positrons, but they are part of the group called *secondary cosmic radiation*. On the Earth, the principal causes of ionizing radiation are cosmic rays and the decay of radioactive isotopes and these constitute the background radiation. For example, the presence of radioisotopes such as the 14-carbon is a consequence of the cosmic rays and the decay of 14-carbon generates ionizing radiation. For a better understanding:

Directly ionizing particles are those with a charge and mass that can ionize an atom through the coulomb's force if it has enough kinetic energy. For instance, an alpha particle moving at 5% of the speed of light with c is ionizing.

- The α particles are formed by two protons and two neutrons. In other words, they are equal to a nucleus of helium. More general, the α particles originate from α decay. They are extremely ionizing. If their origins are radioactive decays, they can interact with the first centimeters of skin. If they arise from ternary fission (nuclear fission with three products as results), they are more penetrating, three times energetic than the previous one, reaching the deep layers of the human body. The cosmic rays are composed of 10-12% of helium nuclei, and they have higher energy than the alpha particles produced by nuclear decay, as much as is necessary to pass through the human body.

- Positrons are the same as electrons in antimatter. They have the same charge but in the opposite sign. When a low-energy positron hits an electron of the same energy level, the mass transforms into energy.

- The β particles are high-energy electrons or positrons and are produced by radioactive nuclei. They derive from the β decay which divides into two types: β^- and β^+ which produce electrons and positrons respectively. When a beta particle passes through matter it can produce secondary electrons or X-rays, and this phenomenon is known as bremsstrahlung. Both with ionizing power. The bremsstrahlung radiation is higher in material with high atomic number, for this reason, to protect from this particle shield from material with a low atomic number are used.

- Charged nuclei are commonly found in galactic and solar cosmic rays. Skin, clothes, or thin layers of shielding are adequate to stop these nuclei. The problem with them is the secondary radiation and relative biological cascade that they produce when interacting with matter.

Indirectly ionizing radiation is electrically neutral but causes secondary ionizations.

- Neutrons can ionize atoms through elastic collision because having a mass similar to protons. When a neutron interacts with a hydrogen nucleus, the atoms become ionized representing high ionizing secondary radiation. On the other hand, when a neutron interacts with an atom heavier than the hydrogen one, only part of its energy is transferred to the other atoms. If this is enough, the other atoms are ionized. Another way is inelastic scattering and consists of the absorption of a neutron by the nucleus. The factors that lead are the scattering section and the neutron velocity.

The **Fig. 1.15** is a summing-up of the previous concepts. γ-rays are represented by wavy lines and charged particles and neutrons by straight lines. The small circles show where ionization happens. γ-rays are the name given to photon radiation, produced by nuclear reactions.

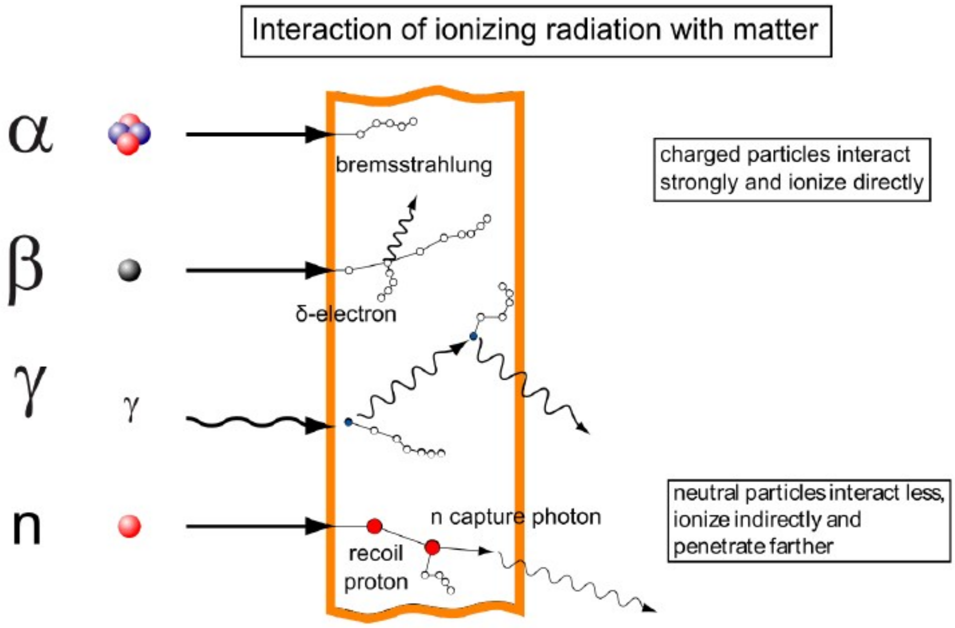

Figure 1.15: Radiation interaction.

1.6.2 Solar wind

Combined with radiant energy, the Sun releases also plasma. The plasma is the state where gas is highly ionized and most of the atoms are split into ions and electrons. The solar wind is the supersonic outflow into the interplanetary space of plasma from the Sun's corona. Globally, however, it appears electrically neutral. The solar wind velocity is in a range from 300 to 700 km/s with a particle concentration of 1 to 20 particles per cm3 [8]. Beyond a few solar radii, the solar wind speed becomes almost constant. Therefore, as the solar wind expands, its density decreases as the inverse of the square of its distance from the Sun. At some large enough distance from the Sun (in a region known as the Heliopause), the solar wind can not contrast the fields and particles of the local interstellar medium anymore, and the solar wind slows down from 400 km/s to perhaps 20 km/s, around 50 AU (Astronomical Unit). The composition of the solar wind is not precisely known. The α particle to proton ratio observation is in the range of 0.037-0.055. The solar wind is also the principal source of volatile elements such as H, He, C, and N.

1.6.3 Coronal mass ejections (CMEs) and Flares

Coronal mass ejections are flows into interplanetary space of a few billion tons of plasma and embedded magnetic fields from the Sun's corona. Different from the steady-state solar wind generated by corona holes where magnetic field lines are open, CMEs start in regions where the magnetic field is closed where disruption of large-scale coronal magnetic structures happen. The exact processes that cause them are not known. CMEs can happen at any time during the solar cycle, and the probability increases with the increase of the solar activity and peaks around solar maximum. CMEs are launched at speeds over 2000 km/s.

A Solar flare is a large explosion on the Sun that occur when stored energy in twisted magnetic fields are quickly released.In few minutes they heat the material over millions of degrees and produce a blowout of radiation across the electromagnetic spectrum, from radio waves to X-rays and γ-rays.

These high energy particles are called Solar Cosmic Rays (SCR). SCRs are mainly composed of electrons, protons ad heavier nuclei as reported in the figure, where most are α particles and other elements, which are easier to ionize [9]. Solar cosmic ray particles are accelerated in the Sun corona or in the interplanetary space. This acceleration can bring particles to relativistic velocity. These can reach Mars in a day circa. For example, considering that Mars is at 1.5 AU from the Sun, electrons are faster than other particles and those with energy between 0.5 and 1 MeV could reach 1 AU within a time of 10 minutes to 10 hours. There are SCR especially during the period of maximum solar activity, it is strange to record them in different periods. The **Fig. 1.16** exposes the higher flux of SCR for three 11-year cycles.

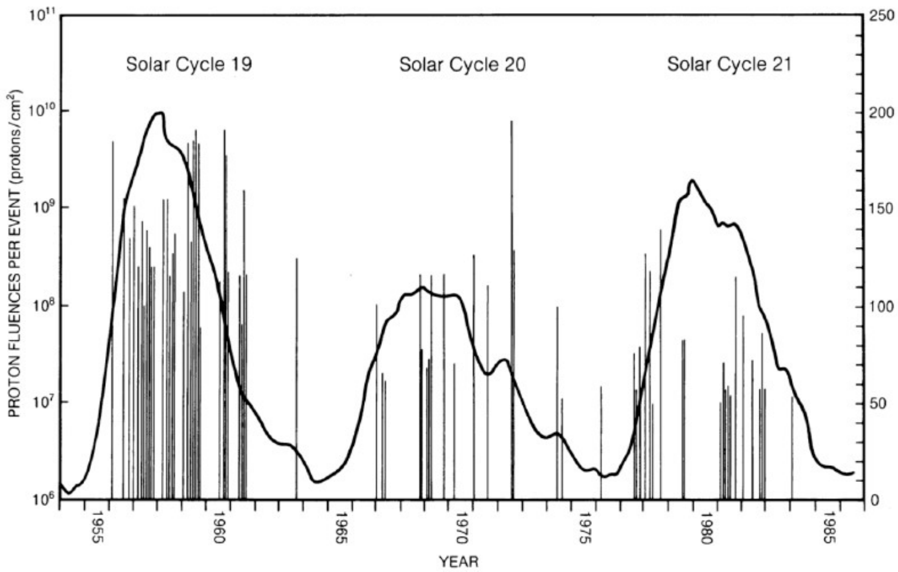

Figure 1.16: Flux of solar cosmic ray, represented with vertical line, and solar activity represented with smoothed line in three 11-year cycle.

The solar activity is usually linked to the number of sunspots on the Sun. These two phenomena happen every 11 years. That is why the history of the Sun and solar activity are classified in 11-year cycles. It is clear from the **Fig. 1.16** that major fluxes of SCR appear together with the maximum solar activity period and specifically when the sunspot number is over 50, circa. The **Fig. 1.17** shows how the quantity of particles reduces rapidly with the rising energy: most particles have energies below 30 MeV. It is rare to have large fluxes of high-energy particles with GeV or higher energies [10]. Scientist usually use three categories for solar flares:

- X-class flares are big;
- M-class flares are medium-sized;
- C-class flares Compared to X- and M-class events are small.

Solar flares are different from CMEs, which were once thought to be initiated by solar flares. CMEs are large sacs of gas joined with magnetic field lines that are expelled from the Sun over several hours. Although some are followed by flares, it is now known that most CMEs are not linked to them.

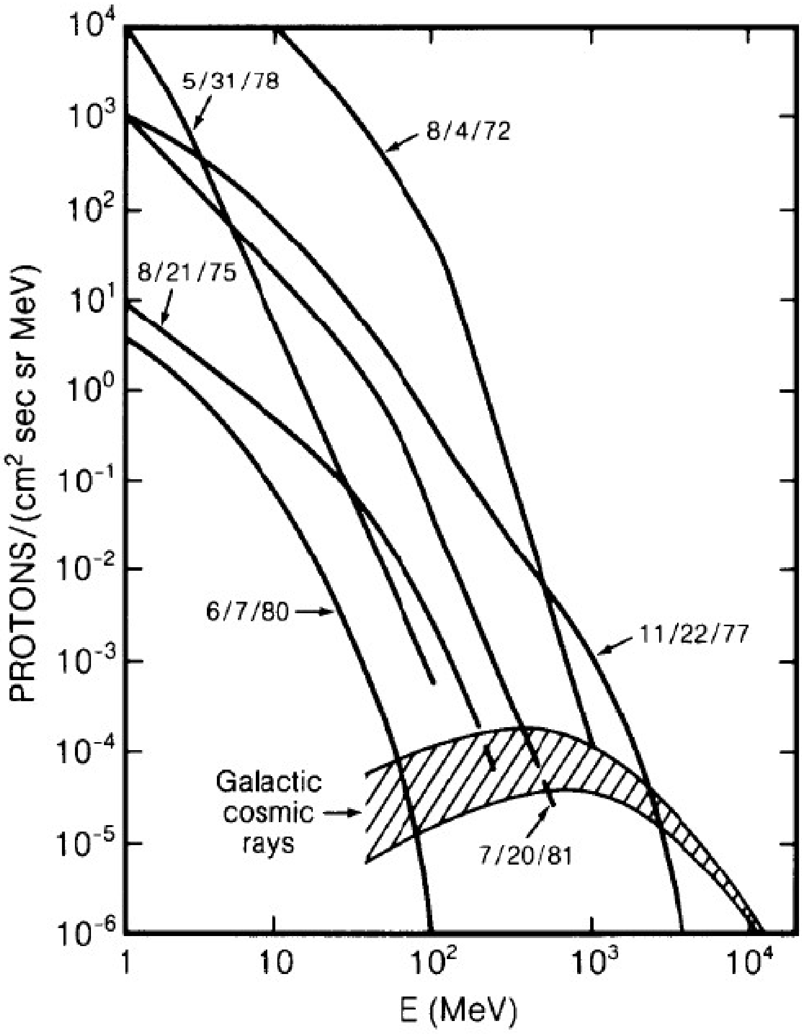

Figure 1.17: Proton fluxes vs. energy in SCR

1.6.4 Galactic Cosmic Rays

Galactic cosmic radiation (GCR) is one of the main agents which determine the radiation condition during long-term (longer than one year) manned expedition. Energetic charged particles of galactic and extra-galactic origin seen in the interplanetary space are called galactic cosmic rays. Galactic cosmic rays are in a wide energy spectrum from many tens of MeV to 10^{20} eV, and even greater. The GCR integral flux with E > 30 MeV seen in the interplanetary space near the Earth (inside our heliosphere) depends on the solar activity cycle, during minimum-activity years, corresponding to N = 4.5 part/(cm^2 s^1) and N = 2 part/(cm^2 s^1) during maximum-activity years. This galactic radiation intensity modulation is caused by the 11-year solar activity cycle as shown in **Fig. 1.19**.

The GCR consists of 83% protons, 13% α-particles, and about 1% nuclei with atomic number Z>2; the electron part is about 3% of the total flux. It should be noted that electrons with energy less than 20 MeV are principally of Jupiter origin. GCR nuclei with Z>2 are considered as several charge groups [11].

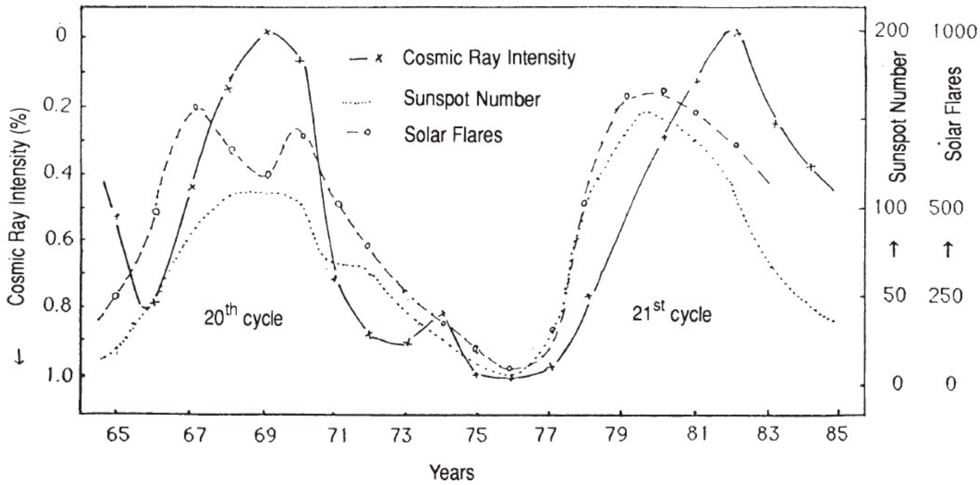

Figure 1.18: GCR, sunspot number on the Sun and solar flares during the 20 and 21 solar cycles.

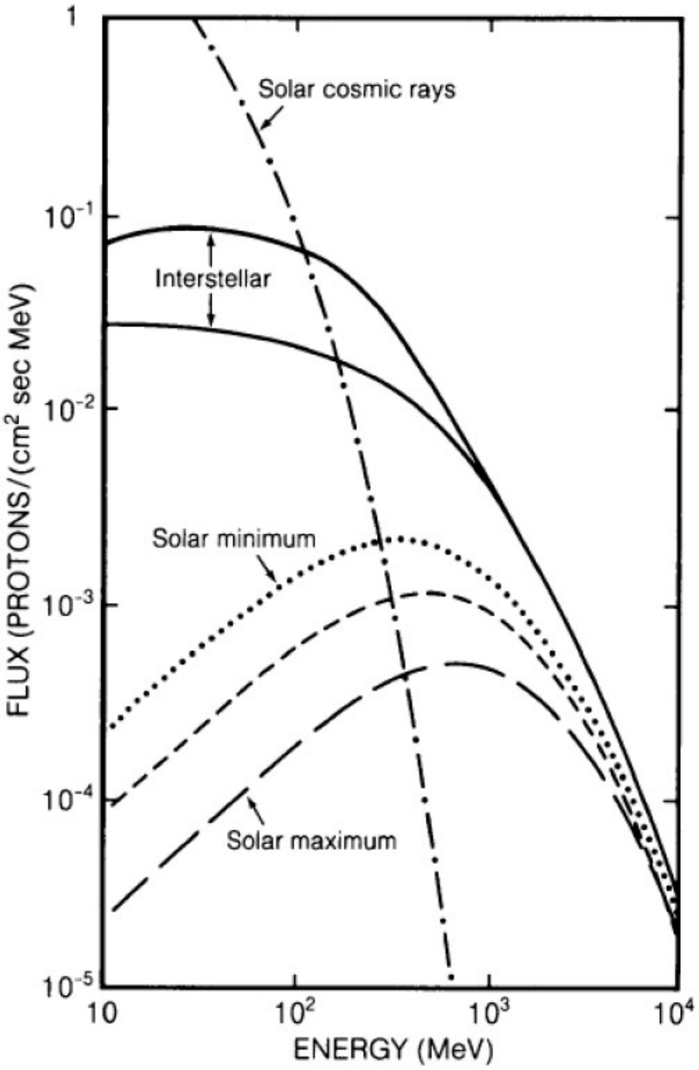

Figure 1.19: GCR proton fluxes vs energy.

1.6.5 Mars Surface Radiation Environment

The radiation exposure on the surface of Mars is much more rigid than on the surface of the Earth because Mars lacks a global magnetic field to deflect energetically charged particles, and the martian atmosphere is much thinner (<1%) compared to that of Earth, giving little shielding against the high-energy particles arriving at the top of its atmosphere. This environmental factor, completely different from the one on Earth, poses a challenge for human exploration of Mars and is also important in learning both geological and potential biological evolution on Mars. The in situ measurements of the ionizing radiation environment on the surface of Mars can be used to test and validate radiation transport models deducted. There are two kinds of energetic particle radiation that arrive at the top of the Mars atmosphere, galactic cosmic rays (GCRs) and solar energetic particles (SEPs). Both interact with the atmosphere and, if energetic enough, penetrate the martian soil, or regolith, producing, via spallation and fragmentation processes, secondary particles (including neutrons and γ-rays) making more complex the radiation environment on the martian surface. GCRs are high-energy particles [10 mega electron volt per nuclear particle (MeV/nuc) to >10 GeV/nuc], which are modulated by the heliosphere and anticorrelated with solar activity as mentioned before. The composition changes lightly depending on solar modulation, with the proton affluence in the range of 85 to 90%, helium ions ∽10 to 13%, electrons ∽1%, and ∽1% heavier nuclei. Due to their high energies, GCRs are hard to shield against and can penetrate up to many meters into the martian regolith. SEPs are the product of the solar activity described in the previous paragraphs. SEP events are irregular and difficult to predict, with durations of hours to days. SEP fluxes are typically dominated by protons, but composition can vary considerably. SEP protons and helium ions have energies below ∽150 MeV/nuc ("soft" spectrum) and do not penetrate to the martian regolith. At Gale crater, the column depths (atmospheric column mass per area) of the Martian atmosphere is around 20 g/cm^2, and energetic particles with energies less than 150 MeV lose all of their energy before moving through this amount of material. But, during "hard spectrum" ions can be accelerated to energies above 150 MeV/nuc (which is also the atmospheric cutoff energy), with fluxes reaching the Martian surface. So, every particle with energies higher than the Martian atmospheric cutoff energy can pass through the atmosphere and reach the surface and some with enough energy can interact with the atmosphere or the regolith generating secondary particles, via spallation or fragmentation as said, worsening the environment. In all events, secondary neutrons generated by SEPs in the atmosphere can arrive at the surface. If martian life exists or ever existed in the past, it is reasonable to assume it is or was linked to organic molecules and will consequently share with terrestrial life the vulnerability to energetic particle radiation. The radiation environment on Mars could additionally play a key role in the chemical modification of the regolith and martian rocks over geologic time scales, influencing the preservation of organics, even potential organic biosignatures of the ancient martian environment. The *Curiosity* rover descended successfully on Mars in Gale crater at ∽ -4.4 km altitude on 6 August 2012. On 7 August 2012, the Radiation Assessment Detector (RAD) began taking measurements on the radiation environment on Mars. The radiation dose rate measured by RAD during the first 300 sols on Mars is reported in **Fig. 1.20**, near the maximum of solar cycle 24. The GCR dose rate varies between 180 and 225 micrograys (mGy)/day, due to the combined effects of diurnal variations from atmospheric pressure changes, Mars seasonal fluctuations at Gale crater, and heliospheric structure variability due to solar activity and rotation.

The diurnal dose rates differ by a few percent because of diurnal change in the Martian atmospheric column, as in **Fig. 1.21B**, which presents data obtained between sols 290 and 302. This daily variation of the total atmospheric column mass is related to the thermal tides that Mars experiences each sol, where there is a redistribution on the atmospheric mass on a global scale. Comparing the RAD dose rate to the Rover Environment Monitoring Station (REMS) of atmospheric pressure measurements there is an anticorrelation between the total dose rate and the atmospheric pressure (**Fig. 1.21B**), which is related to column depth. On the Mars surface, through the 300 days near the maximum of solar cycle 24, there was an average total GCR dose rate at Gale crater of 0.210 $\pm$ 0.040 mGy/day, compared with 0.48 $\pm$ 0.08 mGy/day measured during journey inside the spacecraft (**Fig. 1.22** and **Tab. 1.2**). The

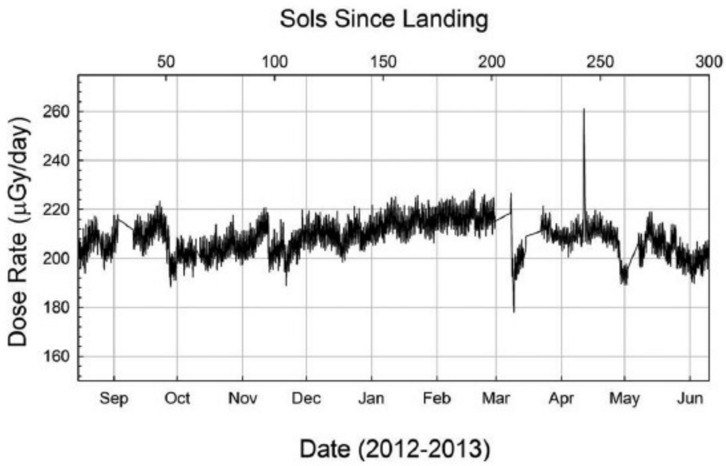

Figure 1.20: Radiation dose rate measured by RAD on the surface of Mars.

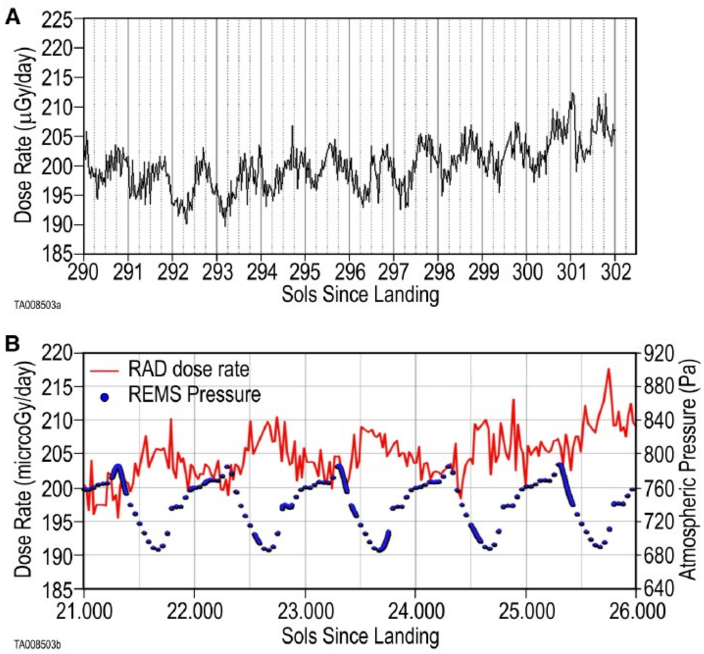

Figure 1.21: (A) RAD daily dose rate versus time. (B) Comparison of RAD dose rate with REMS atmospheric pressure.

difference in dose rate is made by various influences:

- The protection of the planet lower hemisphere reduces the dose rate by a factor of ∽ 2.
- Further differences from this factor 2 are due to interactions of primary GCRs with the nucleons in the atmosphere and soil.
- The atmospheric shielding is thicker than the spacecraft shielding.
- The dose rate is regulated by the modulation of the GCR flux by the sun, and a stronger solar modulation outcome in lower GCR fluxes and so with lower dose rates.

RAD measurement	Mars surface	MSL cruise	Units
Charged-particle flux (A * B)	0.64 ± 0.06	1.43 ± 0.03	$cm^2/s/sr$
Fluence rate (B)	1.84 ± 0.34	3.87 ± 0.34	cm^2/s
Dose rate (tissue-like) (E detector)	0.21 ± 0.04	0.48 pm 0.08	mGy/day
Average Quality Factor <Q>	3.05 ± 0.26	3.82 ± 0.30	(dimensionless)
Dose-equivalent rate	0.64 ± 0.12	1.84 ± 0.30	mSv/day
Total mission dose equivalent [NASA design reference mission]	320 ± 50 (500 days)	662 ± 108 (2x180 days)	mSv

Table 1.2: Radiation environment measured by MSL/RAD (2012–2013) (GCR only).

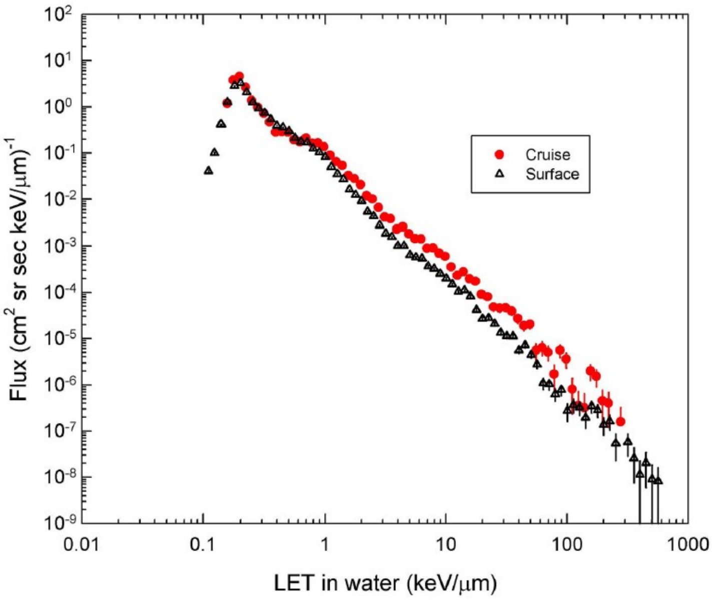

here

Figure 1.22: Charged-particle linear energy transfer (LET) spectrum comparison.

The solar modulation parameter during the mission on the surface was ∽ 577 MV, while the average Φ during the cruise was ∽ 635 MV (resulting in weaker GCR flux on the surface). The average quality factor <Q> (The factor by which the absorbed dose, in rad or gray, must be multiplied to get a quantity that represents the biological damage, rem or sievert, to the exposed tissue) on the Martian surface resulted in 3.05 ± 0.3, compared with 3.82 ± 0.3 measured during the cruise. This small <Q> is due to the thicker shielding in the field of view (FOV) on the surface while during the cruise, approximately half of the RAD FOV was lightly shielded (< 10 g/cm^2). Considering that the column depth of the martian atmosphere was about 21 g/cm^2 over the first 300 sols of *Curiosity*'s mission and combining the tissue dose rate measurement with <Q> leads to an average GCR dose equivalent rate on the Mars surface of 0.64 ± 0.12 millisieverts (mSv)/day (**Fig. 1.23**). The SEP dose was achieved by subtracting the average GCR dose rate during the SEP event. It was found to be 50 μGy in the less-shielded of the two detectors. Because the composition of SEP events (on the surface and during the cruise) are majorly protons, for which <Q> = ∽ 1, the dose equivalent for this event was ∽ 50 mSv, approximately equivalent to 25% of the GCR dose equivalent for the 1-day duration of the event. The frequency and power of SEP events are extremely variable and still unpredictable, and even these observations were made near solar maximum, this current solar activity cycle is very soft by historical norms. Substantial SEP events throughout recent history (February 1956, August 1972, and September 1989) have been reported to be several orders of magnitude more intense than those currently observed to date by the RAD.

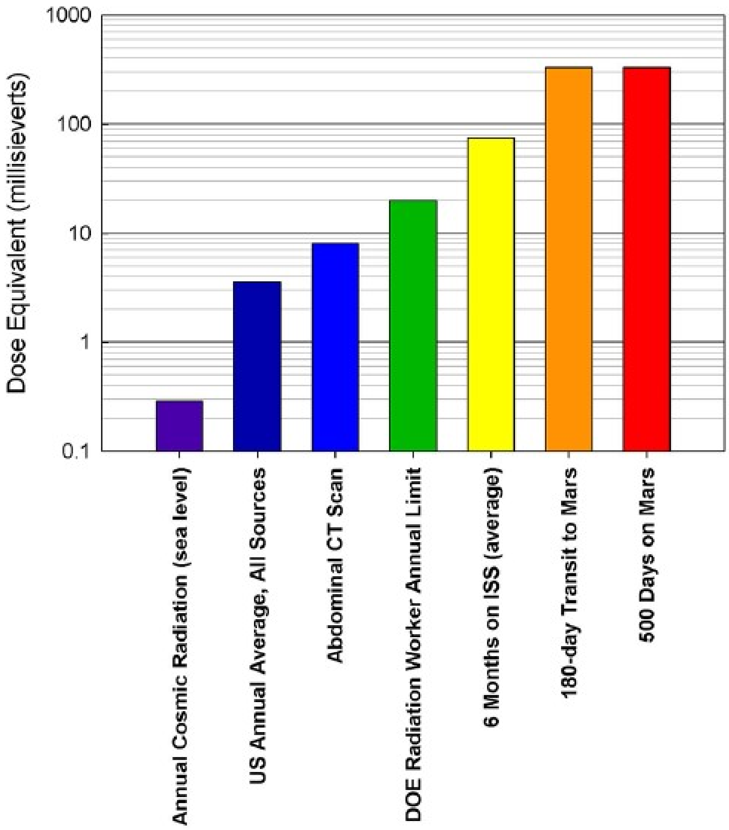

Figure 1.23: Radiation dose-equivalent comparison.

From data obtained during the cruise, the estimated total mission dose equivalent is ∽1.01 Sv for a round trip Mars surface mission with 180 days (outward and return) cruise, and 500 days on the martian surface with the current solar cycle (**Tab. 1.3**). These durations are based on one plausible NASA design reference mission; many mission designs at different times in the solar cycle or in a different solar cycle would result in slightly different radiation exposures. GCR flux modulation by solar activity and risk for exposure to SEPs increases with solar activity, both contribute to the total mission dose of a future Mars mission and it all depends on when in the solar cycle the mission occurs.

The dose and dose-equivalent rates shown in **Tab. 1.2** and **Tab. 1.3** can be used to obtain rates below the martian surface by using the surface measurements. In situ regolith-based materials are prime candidates for astronaut shelter shielding materials to decrease or mitigate the biological hazards linked with radiation exposures on future long-duration human missions, so it is important a good estimation of the subsurface radiation environment. This revised subsurface radiation could help in the studies of the preservation of possible organic biosignatures in relation to depth and survival times of possible microbial or bacterial life forms left asleep beneath the surface. The actual absorbed dose reported by the RAD (76 mGy/year at the surface) (**Tab. 1.4**) allows precise estimations of the

	GCR dose rate (mGy/day)	GCR dose-equivalent rate (mSv/day)	SEP dose (mGy/event)	SEP dose equivalent (mSv/event)
MSL Cruise	0.464	1.84	1.2 to 19.5	1.2 to 19.5
Mars Surface	0.210	0.64	0.025	0.025

Table 1.3: Mars radiation environment summary during 2012–2013 solar maximum (GCR and SEP).

subsurface dose. There could be differences due to differing hypotheses in the models about the level of solar modulation related to the actual level during the measurement period, in addition there is the influence of the atmospheric shielding above the surface. Based on compositional and morphological observations of the rocks in Gale crater, the estimated rock density is 2.8 g/cm^3, which come close to the density of an iron-rich mudstone or siltstone. The natural background radioactivity on present-day Mars is estimated to be circa 1 mGy/day, suggesting that GCR radiation is no longer the principal source of radiation below ∽3 m. This also implies that the advantage of regolith-based shielding materials no longer increases beyond a thickness of ∽3 m [12].

Depth below surface	Effective shielding mass (g/cm^2)	GCR dose rate (mGy/year)	GCR dose-equivalent rate (mSv/year)
Mars surface (RAD)	0	76	232
–10 cm	28	96	295
–1 m	280	36.4	81
–2 m	560	8.7	15
–3 m	840	1.8	2.9

Table 1.4: Mars subsurface radiation estimates (scaled to RAD surface measurements).

1.6.6 Radiation shielding on Mars

To understand better how it is possible to shield a habitat on Mars is necessary to describe a model that considers both the atmosphere and the regolith. It will be now reported the job done in [13] about the models in different scenarios.

To simulate the interactions of energetic particles through the Martian atmosphere and regolith, it will be employed the state-of-the-art Mars Climate Database (MCD) specifying the physical properties and composition of the Martian planetary environment. MCD creates the altitude-dependent data for atmospheric pressure, density, temperature, and chemical composition. In order to validate the model against the RAD data, exposed in the previous paragraph, the data extracted from MCD are based on Gale Crater with a surface elevation of 4.4 km. The composition of the Martian atmosphere is C, O, N, Ar, and H with more than 95% of the molecules being CO_2. Even if the surface pressure varies daily and seasonally up to about 25% at Gale Crater, a surface pressure of 781 Pa, corresponding to a vertical column depth of 21 g/cm^2, is assumed. This pressure is also close to the average value of the first 300 sols data acquired by RAD instrumentation. Seven different subsurface scenarios, with specific densities and compositions, are taken into account. Two distinct rock types, analyzed at different landing sites, and two artificial subsurface compositions have been chosen. Based on Mars Odyssey spacecraft measurements of the epithermal neutron flux in orbit of Mars it was possible to estimate the soil water (hydrogen) contents for numerous locations. As a result of the effective moderation of fast neutrons by hydrogen, the flux of neutrons with epithermal energies is anticorrelated to the quantity of hydrogen and consequently water ice in the soil. From these water content estimations, another three scenarios with subsurface water ice have been considered:

1. An iron rich sandstone (SS) as examined by Curiosity at the Cooperstown land. As a typical value for sandstone on Earth a bulk density of 2.2 g/cm^3 is used for SS.
2. A basaltic andesite rock type (AR) as examined at the Pathfinder site. Has intermediate quartz content of 57% by weight and a density of 2.8 g/cm^3.
3. Quartz (SiO_2), which is a major component of all igneous rocks found on Mars and Earth. Normally not present in its pure form, but this is a simplified scenario for the Martian rocks.
4. Sulfur concrete (SC) as a theoretical material for the construction of future buildings on Mars. Composed of 50% sulfur and 50% Martian soil by weight with an approximated density of 2.0 g/cm^3.
5. A homogeneous mix of 50% water and 50% basaltic andesite rock by weight (W50). Is a presumably realistic scenario for the Martian north pole, with a bulk density of 1.4 g/cm^3.
6. A homogeneous mix of 10% water and 90% basaltic andesite rock by weight (W10), with a bulk density of 2.4 g/cm^3.
7. An inhomogeneous scenario for Arabia Terra (AT), where a soil mix of 10% water by weight underlies 30 g/cm^2 of dry rock. This scenario is supposed to be realistic for some nonpolar areas on Mars.

The chemical components have been converted into an elemental composition and shown in **Tab. 1.5** and **Tab. 1.6** for the dry and hydrated scenarios, each.

Dry scenarios	**O**	**Si**	**Fe**	**Other**	**Density (g/cm^3)**
Quartz (SiO^2)	53	47	0	0	2.8
Andesite rock (AR)	44	27	12	17	2.8
Sandstone (SS)	41	21	20	18	2.2
Sulfur concrete (SC)	22	10	8	60 (51% S)	2.0

Table 1.5: Mass fraction (%) of elemental compositions and densities of the Dry Subsurface Scenarios (normalized to 100%).

Typical values for solar modulation parameter Φ in the model range approximately from $\Phi = 400$ MV for solar minima to $\Phi = 1,000$ MV for solar maxima. Except for the Arabia Terra scenario, all subsurface layers are considered homogeneously in composition and density at different depths. In terms of radiation effects, an important quantity is the absorbed dose, which describes the energy deposited by all energetic particles (charged and neutral) as they pass through matter, normalized to the mass of the matter. It has the unit of gray which is equivalent to J/kg. The model gives the particle spectra (of different species) at certain atmospheric/ regolith profundity. These particles are then used to determine the induced dose. The same particle spectra may produce different absorbed doses due to different material properties (like a detector, a biological structure, or even a human body) and geometry. This is because larger objects can more easily arrest ions inside, and the interaction with arriving particles to generate secondaries is also more likely as shown in **Fig. 1.24**. The absorbed dose produced in a water sphere phantom with a radius of 15 cm, which is a simplified model of the composition and dimension of the human torso and a silicon piece of 300 μm thickness (as a comparison with the RAD dosimetry silicon detector). The equivalent dose of the water sphere is also calculated as defined by the International Commission on Radiological Protection (ICRP). It has the unit of sievert (Sv) and represents the biological effect of the absorbed dose by using a weighting factor related to the incident particle types, and energies in the case of neutrons. These factors are 1 or 2 for light particles such as photons, electrons, protons, muons, and pions. For space dosimetry purposes, another measure called "dose equivalent" (also in Sv) is often evaluated, as in the case of RAD measurement. It is determined as the product of detected absorbed dose converted in water and a mean biological quality factor <Q> and depends on the linear energy transfer (LET), which is the mean energy loss by charged particles because of the electronic interactions per unit path length. Regarding the protection of future astronauts on Mars, the equivalent dose used in this paragraph is an overestimation of the maximal potential hazard.

Hydrated scenarios	**Water by weight (%)**	**Rock by weight (%)**	**Density (g/cm^3)**
10% water & 90% andesite rock (W10)	10	90	2.4
50% water & 50% andesite rock (W50)	50	50	1.4
Arabia Terra (AT)			
Above 30 g/cm^2	0	100	2.8
Below 30 g/cm^2	10	90	2.4

Table 1.6: Bulk Densities and Mass Fractions of Hydrated Scenarios Containing Water.

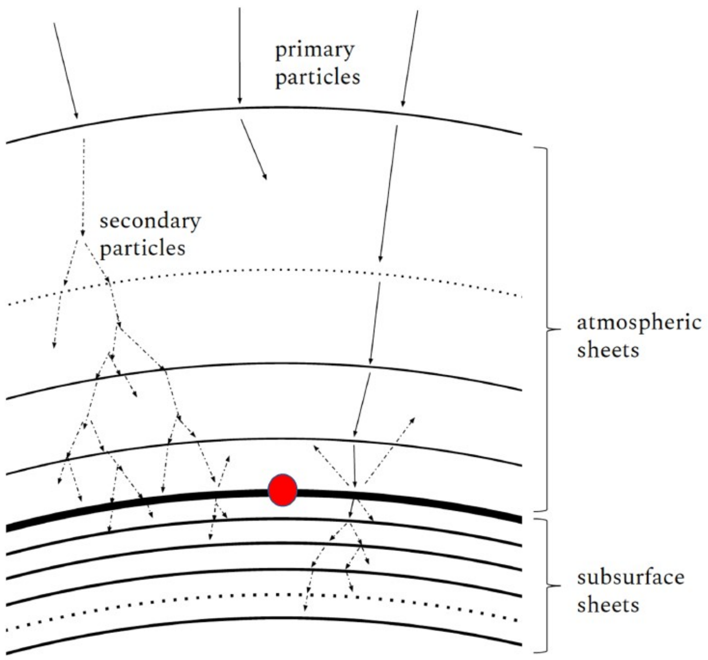

Figure 1.24: Chain effect starting from the primary particles hitting, propagating through, and interacting with the Martian atmosphere and regolith.

During the first 300 sols after the landing of MSL, RAD measured a surface dose rate of 58 ± 5 mGy/yr in the silicon detector considering an average solar modulation parameter of about 580

MV and a mean column depth of 21 g/cm^2. Assuming similar GCR and atmospheric conditions, the model of the surface radiation environment show a dose rate in the silicon slab of 51.6 ± 0.6 mGy/yr as shown in **Fig. 1.25**. This agrees closely with the data in the lower standard deviation of 11%. The absorbed dose in the water sphere is in all cases 10–16% higher related to the silicon slab, which can be explained by the higher ionization energy loss by charged particles in water and by the risen sensitivity to neutrons in the water sphere.

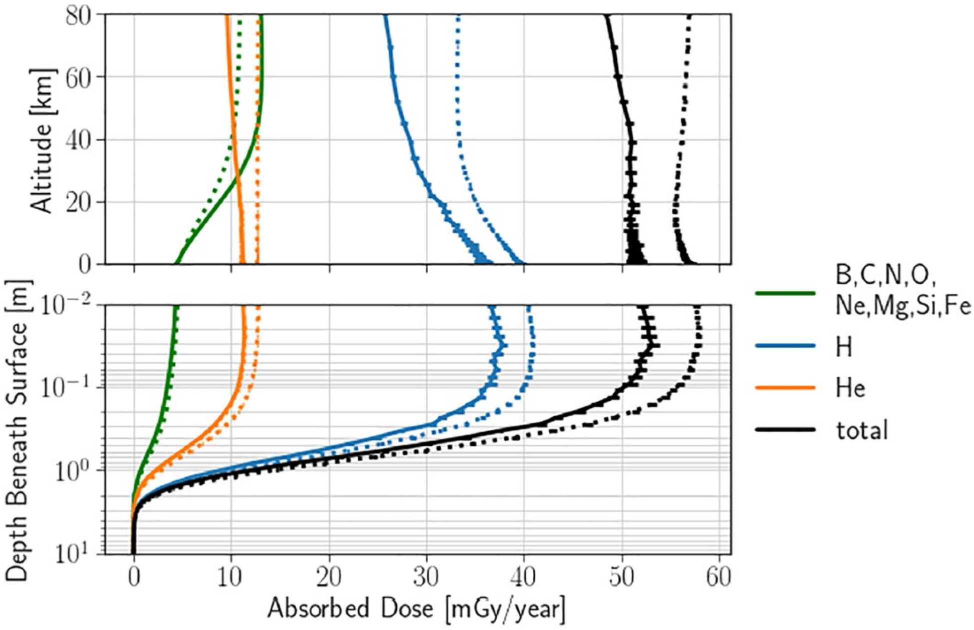

Figure 1.25: Primary particle contribution to absorbed dose rates in the water sphere (dashed) and silicon slab (solid). Hydrogen (blue), helium (orange), eight heavier primary particle species (green). All are summed up to the total absorbed dose (black).

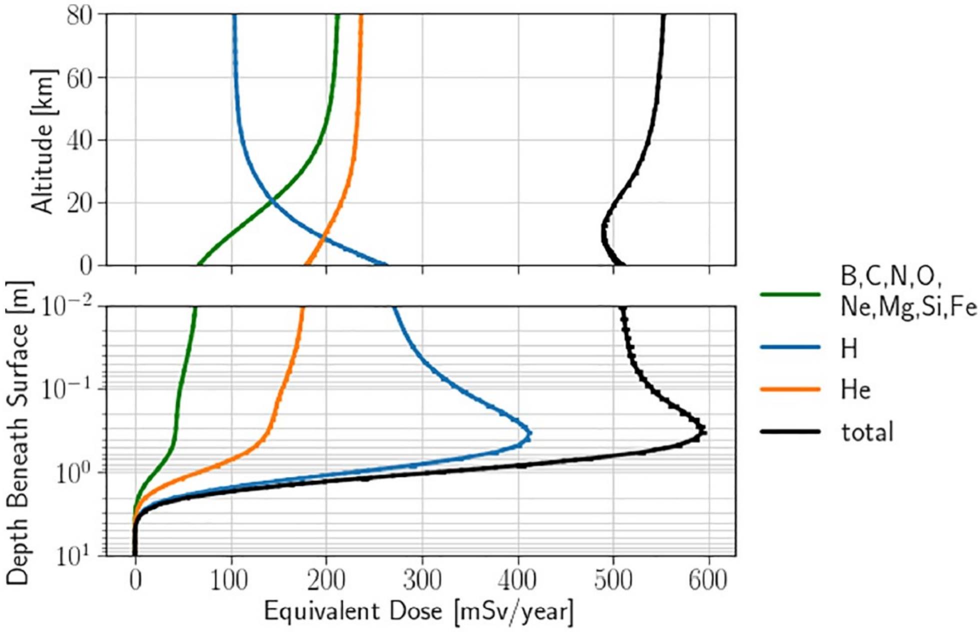

Figure 1.26: Primary particle species contribution to equivalent dose rates in the water sphere.

The blue lines in **Fig. 1.26** show that the primary GCR proton contributed absorbed dose rate rises with rising atmospheric depth. A maximum is reached at 3 cm under the surface, from where the proton-induced dose rate decreases with rising depth. This can be explained as primary protons through the atmosphere lose energy by ionization and excitation of the target material and by the generation of secondary particles that additional contribute to dose rates. Though, primary particles with higher Z values tend to fragment more frequently in the atmosphere and in general have a smaller penetrating depth (a measure of how deep electromagnetic radiation can penetrate a material) through ionization energy loss. As shown, the total absorbed dose rate produced by primary high Z GCRs regularly diminishes with rising depth. Primary protons, particles with energy over 178 $\pm$ 21 MeV, contribute in more than 97% of the surface dose rate, while for primary irons, the cutoff energy is 35 $\pm$ 5 GeV (or 620 $\pm$ 90 MeV per nucleus). On the surface of Mars, the largest portion of the absorbed dose is produced by primary hydrogen (about 69–70%) and helium (about 22%) GCR particles. **Fig. 1.26** shows proton-contributed equivalent dose rate rises with rising atmospheric depth, more clearly than that in Figure, and also grows with the regolith depth. There is a peak at 30 cm beneath the surface, even for the total equivalent dose rate. In comparison to the absorbed dose rate in the water sphere (**Fig. 1.25**), this more important increase of the proton-contributed equivalent dose rate with depth can be explained by a severe rise of the generation of secondary particles with a higher radiation weighting factor, in particular neutrons, as already discussed.

Fig. 1.27 shows the model for absorbed dose rate as registered in the silicon slab for the seven subsurface situations, only primary hydrogen and helium particles are simulated, because as it was said they contribute the majority amount, more than 90%, of the Martian radiation environment. The shielding depth is represented in units of g/cm^2, but it is known to be different from the actual atmospheric/ regolith height. There is no important difference between the absorbed dose rates under various shielding properties within the uncertainty of the statistics. If at all, there is only a small reduction in the absorbed dose under the 50% water-rock mix. For all other materials, a peak in absorbed dose rate is reached at about 30 g/cm^2 of shielding depth (including atmospheric column depth) within the subsurface.

Figure **Fig. 1.28** shows the absorbed dose rate in the water sphere in relation to the height (which is different from the column depth) of the Martian environment for seven different subsurfaces. The adoption of different units of atmospheric depth in **Fig. 1.26** and **Fig. 1.27** exhibits the difference in densities of various regolith considered. On the surface, the excess of subsurface water produces a minor reduction in absorbed dose rates of 5% for W50 and 3% for W10 compared to other scenarios. Though, at deeper subsurface depth, as better shown in **Fig. 1.28**, the dry rock materials have lightly more shielding than the water mix materials due to their bigger bulk densities. **Fig. 1.29** shows the equivalent dose rates in the water sphere in relation to height. It is visible the advanced shielding effect of subsurface materials with water is severely increased. The surface equivalent dose on Mars surface diminishes by about 45%, 36%, and 27% for the 50% water, 10% water, and Arabia Terra scenarios, respectively, compared to the dry andesite rock scenario. In the top meter of subsurface material, the improved shielding effect is maintained for all water scenarios despite the lower density. The inhomogeneous Arabia Terra scenario shows a significant reduction even in equivalent dose rates in the top dry layer at 0–11 cm below the surface. Under this depth, the Arabia Terra scenario contains 10% water, equal to the W10 scenario. At ∽40 cm, the shielding effect of the Arabia Terra scenario is almost the same as W10 scenario.

The observed anticorrelation of subsurface water abundance and the equivalent dose is explainable by calculations of all secondary particle species that contribute to the dose. **Fig. 1.30** shows the surface neutron flux of the 50% water, 10% water, and andesite rock scenarios, respectively, in order to explain the observed anticorrelation of subsurface water abundance and equivalent dose. There is a drastic reduction in neutron fluxes beneath 10 MeV for the first two hydrated scenarios. On the y axis, the differential neutron flux dF/dE is multiplied by the energy of the neutron itself which is the highest energy that neutron can place in an object. The neutron flux continues up to an energy of 10 TeV, matching to the maximal primary proton energy due to the conservation of momentum

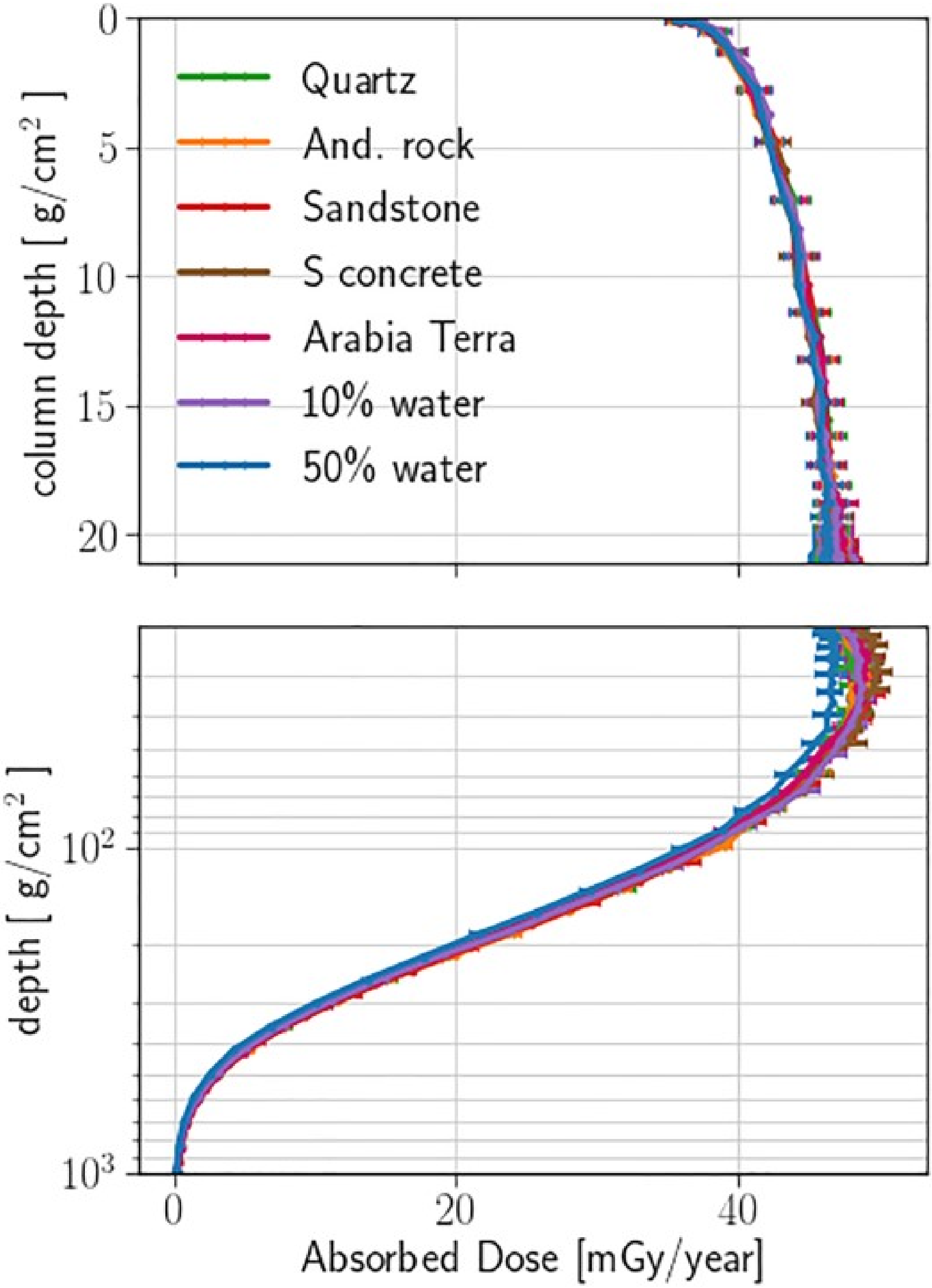

Figure 1.27: Absorbed dose in the silicon slab versus the Martian atmospheric and regolith depth (in unit of g/cm^2) under the different subsurface scenarios.

during nearly elastic hadronic processes. While surface neutron fluxes over energies of ∽10 MeV are not significantly influenced by the subsurface water, at lower energies a more effective attenuation is observed. When compared to the dry andesite rock scenario, neutron fluxes are diminished by factors of ∽2 and 5 at around 1 MeV for W10 and W50 scenarios, each. The reduction factors are also higher at lower energies. 1 MeV neutrons have the highest biological weighting factor (over 20) compared to other neutron energies or particle species, the attenuation of the neutron flux nearby this energy below the hydrated scenarios significantly diminishes the equivalent dose. The strong attenuation of neutron fluxes by big contents of subsurface water is due to the high concentration of hydrogen in water and incident fast neutrons frequently experience efficient elastic scattering. These slowed-down neutrons are then more simply caught by hydrogen, with the emission of gamma rays then the scattered neutrons are

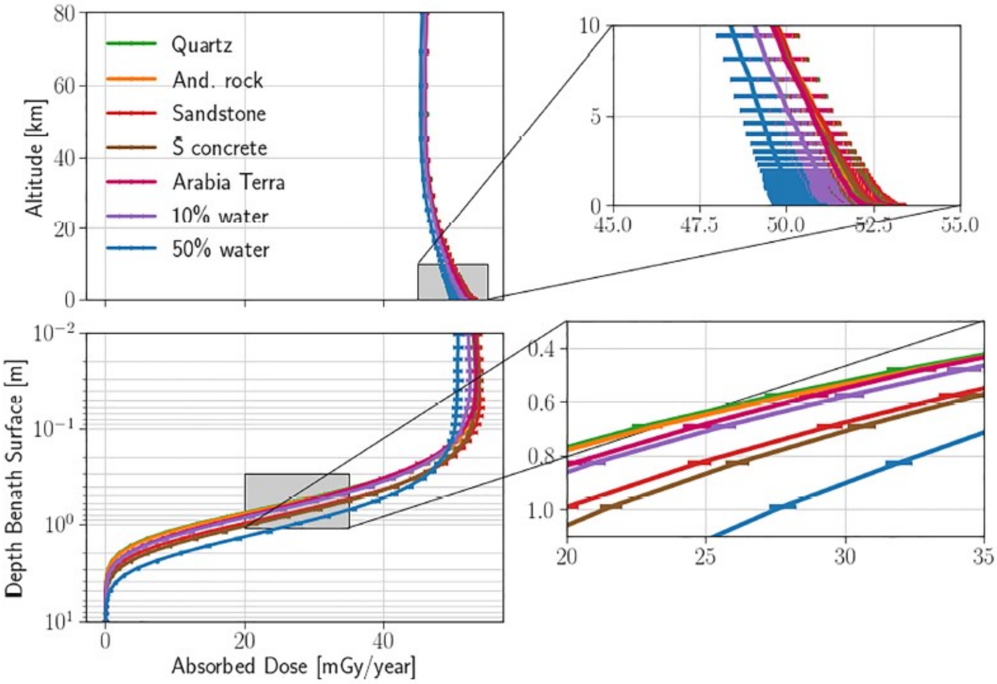

Figure 1.28: Absorbed dose in the water sphere versus the Martian atmospheric and regolith depth (above and below the surface, respectively) under the different subsurface scenarios. The regions above surface up to 10 km and from 0.3 to 1.1 m below the surface are increased to see better the differences.

thermalized by the subsurface hydrogen and are less capable to reach the surface thus. This starts an indirect shielding effect in water-rich scenarios compared to dry scenarios. Otherwise, surface spectra of other major particle kinds, especially ions, do not appear to depend on subsurface water contents. This is principally because they are essentially primary particles and secondary particles produced in the atmosphere and the albedo contribution to the high-Z fluxes from the soil is comparably small. Furthermore, the biological weight of particles, like protons or photons, contributing to equivalent dose is lesser than that of neutrons around 1 MeV. For these reasons, the equivalent dose varies by about 45% between W50 and dry scenarios on the surface (and over to 75% in the subsurface) as reported in **Fig. 1.29** so the equivalent dose in the water sphere is largely dominated by the contribution of neutrons. Subsurface composed of dry materials as andesite rock, sandstone, and quartz in **Fig. 1.29** show an increment in equivalent dose rates reaching a peak at about 30–40 cm or 88–102 g/cm^2 depth, except sulfur concrete for which there is no significant change in the equivalent dose rate within the upper 50 cm of subsurface material. Just to remember that what already exposed is the equivalent dose which only includes H and He primary particle species. The additional contribution of heavier ions to the equivalent dose rate within the water sphere is often considered to be within the order of ∽10%. In **Tab. 1.7** are reported the required shielding depths for a few examples of equivalent dose reducing to specific values. This is useful for shielding strategies for the design of future habitats on Mars choosing the optimal shielding material (with the least amount of required shielding depth) under a selected requirement of equivalent dose. For example, for equivalent dose reductions below 200 mSv/yr, the 50% water scenario is optimal. For an equivalent dose rate below 100 mSv/yr, the Arabia Terra and W10 subsurface scenarios are convenient, presenting relatively higher densities than W50.

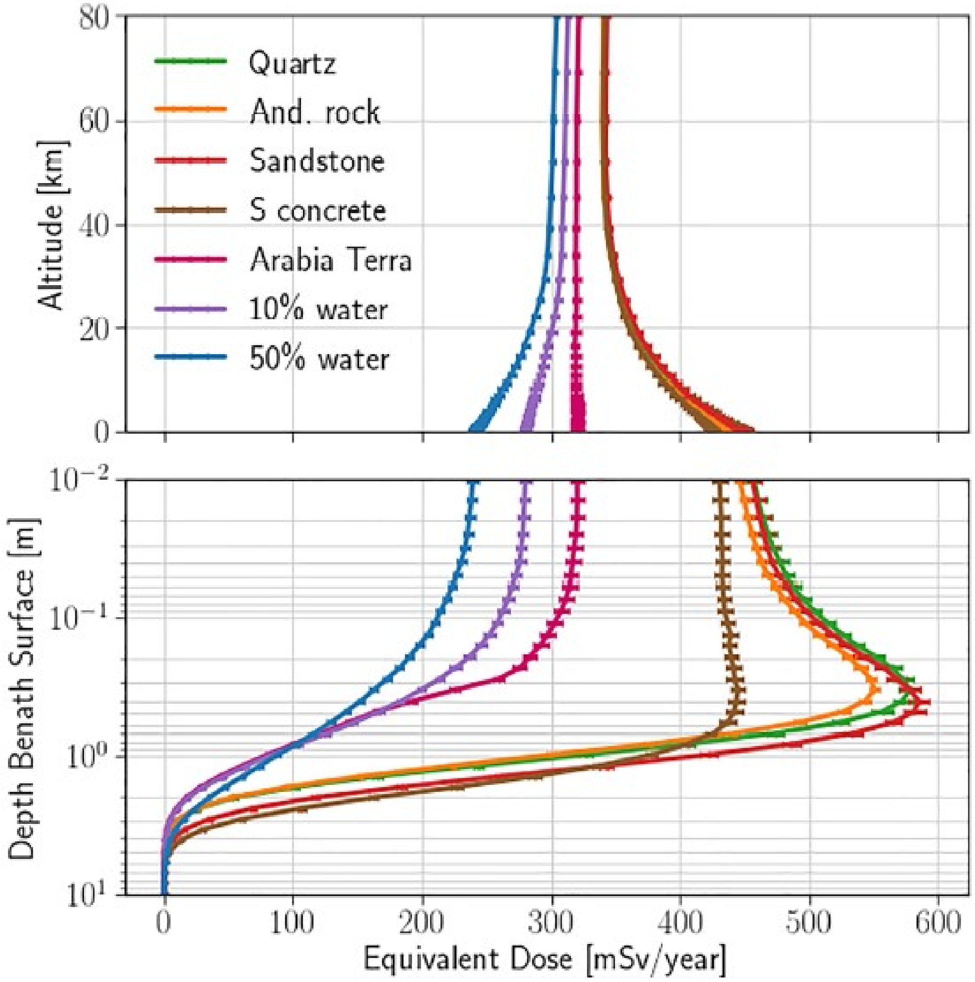

Figure 1.29: Absorbed dose within the water sphere versus the Martian atmospheric and regolith depth (above and below the surface, respectively) under the various subsurface scenarios.

A fixed and medium solar modulation parameter has been employed in the previous calculation, in order to confront the results with the RAD measurements with similar heliospheric circumstances. This because absorbed dose and equivalent dose can be heavily affected by variations of the primary GCR flux which is modulated by the heliospheric activities. Weaker solar modulations (smaller values of Φ) usually result in higher GCR fluxes in space and consequently also over and below the surface of Mars as seen by the MSL/RAD at Gale Crater. Values of $\Phi = 400$ MV, $\Phi = 580$ MV, and $\Phi = 1,000$ MV representing different powers of solar modulation conditions, from weaker to stronger, will be considered. To have an equivalent dose rate reduction below 200 mSv/yr, less than half of the surface equivalent dose rate under dry scenarios while medium solar modulation condition and 100 mSv/yr, which is the limit above which increased lifetime cancer is evident, the needed shielding depths under different subsurface types are shown in **Fig. 1.31**. During solar maximum conditions when GCR fluxes are weaker, less shielding material is required for all subsurface scenarios. As a result, no shielding is needed during the peak of the solar maximum condition of $\Phi = 1,000$ MV with a W50 scenario. It is clear that the surface materials with water content require less shielding depth than the dry regolith conditions.

The first 200 g/cm^2 (0.7–0.9 m) of soil depth can be considered as the minimum shielding depth for potential human habits based on dry rocky subsurface materials on Mars, this is what it can be extrapolated from **Fig. 1.31**. Any "shielding" thickness less than this value may even intensify the equivalent dose, ending in a worsened radiation environment. On the other hand, medium to huge

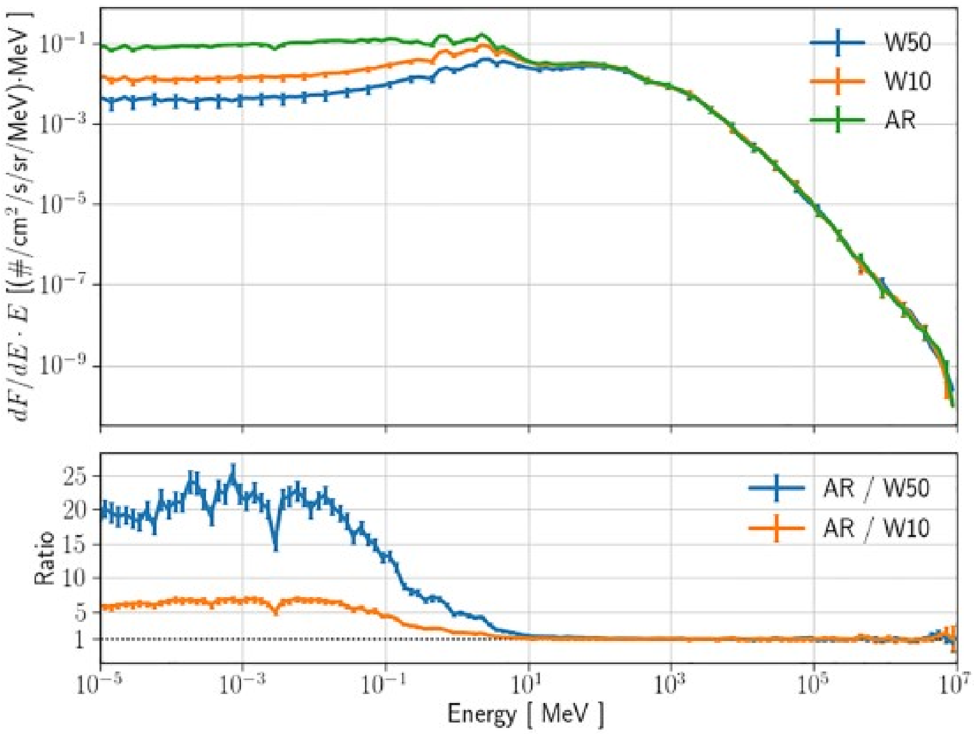

Figure 1.30: Comparison of surface neutron fluxes modeled using different surface materials. W50 stands for 50% water content in the andesite rock, and W10 stands for 10% water in the andesite rock. AR represents andesite rock. (top) Differential neutron flux dF/dE multiplied by neutron energy E versus the neutron energy. (bottom) Ratio of differential fluxes.

Equivalent dose per year	**Required subsurface shielding depth (cm)**					
(mSv)	AR	SS	SC	AT	W10	W50
400	79±1	105±1	89±3	None	None	None
300	100±1	131±1	137±2	14±3	None	None
200	126±1	164±1	184±1	39±1	34±3	16±1
100	167±1	215±2	248±2	84±2	87±1	87±1
50	205±1	265±3	305±3	133±2	137±2	164±3
10	295±3	377±6	432±6	240±3	243±3	334±6

Table 1.7: Required Shielding Depth for Reduction of Equivalent Dose Rate to a Given Value in the Water Sphere. Note. AR = andesite rock; SS = sandstone; SC = sulfur concrete; AT = Arabia Terra; W10 = 10% water in the andesite rock; W50 = 50% water mixture with andesite rock. Solar modulation condition is Φ = 580 MV. “None” means no shielding is needed.

amounts of subsurface water ice (10–50% by weight) are highly advantageous, both for direct shielding under the surface and indirect shielding above the surface. The increase of shielding effect because of the water content in the surface material can be described by the attenuation in neutron fluxes beneath 10 MeV as shown in **Fig. 1.30**, due to the enhanced biological weighting factor of neutrons at

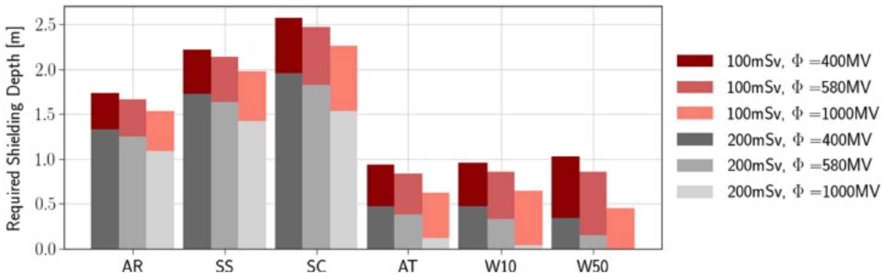

Figure 1.31: Subsurface shielding for $\Phi = 1,000$ MV, $\Phi = 580$ MV, $\Phi = 400$ MV solar modulation. Gray and Red bars indicate the required shielding depths to achieve an equivalent dose reduction to 200 mSv/yr and 100 mSv/yr, each.

this energy range contributing to the equivalent dose. It is important examining the neutron spectra and efficiently diminishing the neutron flux in order to have a better shielding environment of future human habitats on Mars. Regolith-based shielding could be granted even by various natural geological features, giving potential habitats for humans on Mars. Observations from the orbit of Mars showed that possible cave skylights or lava tubes which could provide shelter from cosmic radiation. Also, enhanced content of water ice in the subsurface can reduce the equivalent dose due to the reduction and absorption of biological effective neutrons by hydrogen. Indeed above the surface without direct regolith-based shielding above, equivalent dose rate is estimated to be reduced by about 36% with a homogenous subsurface water content of 10%. From previous studies is suggested that the highest water content on the planet can be supposed at the cold polar and subpolar areas of the north and south poles. Even in some regions near the equator ther are relatively high contents of water underlie a dry top layer, that is, Arabia Terra and the Medusae Fossae. These regions with high-water content might be favored and realistic landing and habitat sites for diminishing the radiation risk of a long-term sojourn on Mars.

Moreover, as already said before, high solar modulation circumstances are generally better for decreasing the GCR-induced Martian surface radiation. For solar maximum conditions ($\Phi = 1,000$ MV) surface equivalent dose decreases by about 49–54%, depending on the subsurface material, than to that of solar minimum conditions. Of course, the risk for exposure to SEPs through solar maximum conditions could alternatively rise. However, because SEPs have usually lower energies (only up to 1–2 GeV in rare case) than GCR particles, they are more easily to be shielded by the atmosphere and regolith. So, the shielding depth suggested before, against GCRs, is also enough for shielding against SEPs.

Chapter 2

Martian habitat in literature

There are different solutions for extra-terrestrial habitat in literature. Since the lunar missions, the interest in build a habitat on another planet strongly increased. In this chapter different solutions proposed in other papers will be taken into consideration in a way that a comparison with the solution offered in this thesis could be possible in order to show vantage and disadvantage. It is clear that the viability of long duration visits with appropriate radiation shielding/crew protection, depends on the construction of habitat structures, preferably in advance of a manned landing, and preferably utilizing in-situ resources.

Figure 2.1: Martian habitat render.

Autonomy is the most peculiar characteristic of interplanetary missions than orbital flights. Crew independence and self-sufficiency as far as functioning, choice, and timing of psychological support measures; health monitoring, countermeasures, diagnostic investigations, and medical care are concerned. This self-confidence will add to the crew loading, responsibility, and stress, which are all that functions currently done by the ground controllers and are now entrusted to the crew.

2.1 Planetary Surface Habitat

NASA's 1997 Habitats and Surface Construction Technology and Development Roadmap, classified three wide categories of space and surface habitats and the means of constructing them.

Class of Construction	Title	Characteristics
I	Pre-Integrated	Fully built and combined on Earth before launch. Lands on the surface and stays in one place.
II	Deployable	Fully built on Earth but may be combined, constructed, deployed, erected, inflated, moved or reconfigured on the lunar/planetary surface.
III	In Situ Resource Utilization (ISRU)	It may be produced on Earth, but includes in situ materials on the surface or basic structure may use in situ construction.

Table 2.1: NASA Planetary Surface Habitat Classifications.

The Habitat Structures group within NASA/Marshall Space Flight Center's ISFR team determined a list of "Top level requirements":

- Support a pressurized (shirtsleeve) environment for the crew
- Protect the crew from a worst case radiation (galactic cosmic radiation (GCR) & solar particle events (SPE)) exposure
- Protect the crew from micrometeorites and exhaust plumes
- Initially, be able to be fabricated in advance of a manned crew so as to provide immediate protection (semi-autonomous construction)
- Early, achievable, and visible milestones and successes are required
- Development should be evolutionary and scalable
- Present a psychologically/ergonomically compatible living environment for the crew

Also, a life cycle of 15 years has been assumed for a Lunar or Martian habitat. For consistency, it has been assumed a habitable, pressurized area/volume consisting of the equivalent of three rectangular rooms, each 6 m x 6 m with 3 m ceilings, or a hemisphere with an equivalent diameter that would support a contained 6 m x 6 m x 3 m room. Relevant parameters of these two configurations are summarized in **Tab. 2.2**

Parameter	Rectangular Configuration	Hemispherical Configuration
Dimensions	6 m long x 6 m wide x 3 m high	10.5 m diameter, 5.25 m high at center
Floor area, m^2	∼37	87.5
Volume, m^3	113	308
Wall/Ceiling/Roof Area, m^2	186	350

Table 2.2: Relevant Physical Parameters of an Assumed Habitat Structure.

A description of the three types of habitat classified in **Tab. 2.1** will be done now, to understand better the differences between them.

2.2 Pre-Integrated structures

In this group are considered the rigid structures which are all those structures designed to preserve their shape avoiding high deformation and displacement when subjected to the operative loads. They are made of trusses and frames structures and are usually composed of metal or composite material. Until today they are considered the most widely used structures in the aerospace field. The reason is their high safety due to the deep knowledge about the performance of the mentioned materials developed in the past years. Rigid structures provides also high puncture resistance and are meant to keep the desired shape without the necessity of a secondary structure, unlike inflatable structures. However, the disadvantage is a frequently higher mass and the difficulty reduction of their volume during the transport phase.

Figure 2.2: ISS Tranquillity module. (Image credit: Thales Alenia Space)

They are cylinders, closed at the top with two truncated cones where standard interfaces are placed to permit the connection with the opposite modules. The primary structure consists of cylindrical isogrid stiffened panels welded together to achieve the specified length of the module. The panels are obtained by machining with machine tools and joined together through a friction steel welding process. The secondary structure consists of standard-sized racks, which have the task of accommodating scientific experiments, equipment and facilities for the astronauts. additionally, layers of various materials envelop the module protecting it from the extreme temperature of the space environment and micro-meteorites hazard. These layers aren't visible in figure that shows only the first structure of the module. All modules are equipped with the following systems: Environmental Control and Life Supports System (ECLSS), Thermal control system (TCS) Data Management System (DMS) and Electrical Power System (EPS). To have an idea of module dimensions, the Columbus has a diameter of 4.2 m and a length of 8, with a weight of 10.2 tons and a pressurized volume of 75 m^3. However, only 25 m^3 is the free volume when all racks are installed.

2.3 Deployable structures

Deployable structures are a solution in which the starting volume is less than the final volume. In this group are also considered the inflatable structures, which are also considered in the aerospace sector. These structures are principally produced with fabrics or membranes. They can maintain the desired shape and resist the operative loads only through the help of the internal pressure, the presence of a secondary support structure, or both of them. The principal reason for the interest in this kind of structure is their capacity to reach small volume and sizes once folded and to guarantee large spaces once inflated. Terms "inflatable" and "deployable" do not have a standard use in the literature, it seems preferable to use inflatable for flexible and foldable materials that are balloon-like and deployable for rigid but storable elements that are mostly mechanisms. Inflatable structures are not very popular in the aerospace sector and the reasons are mainly two: they are built with recently created exotic material (compared to metal ones) and the deployment method is not linear, showing high deformations, which are difficult to model mathematically. Besides, the first consideration determines a little in-depth knowledge of their behavior, therefore lower reliability.

In summary, the main advantages of inflatable structures are:

- high packaging in the closed configuration: they have a 25% packaging advantage;
- low mass: 50% weight advantage because composed of very thin materials;
- low cost: costs reduce, in particular for structures like space antenna;
- possibility to be inflated many times.

But the greatest advantage of this kind of structure could be also a disadvantage for the habitability. Habitability is the total of those conditions which make a space pleasant to live in and a productive place where work in a personal space. These represent an important factor in the psychological wellness of isolated groups Disadvantages are:

- not very high punctual resistance;
- the need for higher care in the folding phase, because it is necessary to avoid bends in an orthogonal direction which could cause high stress during the deployment phase [14] [15].

2.4 In Situ Resource Utilization (ISRU) structures

All the materials exposed to the severe Martian environment undergo aging, with the resulting degeneration of their mechanical properties. The materials mainly vulnerable to these circumstances are the composite ones. In fact, the polymer matrix, in which the fibers are sunk, is profoundly sensitive to radiation and humidity, which can lead to fragility and growth of microcracking. The vacuum is also not a pleasing condition for them, since it is the cause of the outgassing phenomenon. A solution to these problems could be the application of raw materials already existing on Mars, to create shielding structures, for those made of composite materials, or to build new and autonomous ones. This can leads also to a reduction in the number and mass of structures carried from the Earth, reducing mission cost. Though, this solution requires advanced robotic manufacturing capabilities.

Useful Martian raw materials, from a structural point of view, are types of soils presented in the previous chapter. Sintering the soil or combining it with water carried from the Earth or using Martian regolith with a percentage of water ice, already existing there. Sintering is a method where the material is heated to its melting point and then cast into molds or used for 3D printing. This process aims to allow the production of artifacts in dry environments.

2.5 Proposed Mars Habitat architecture

Now will be done a review of design concepts for Mars exploration habitats that illustrate design thinking during the quarter-century from the 90-Day Study in 1989 to the Evolvable Mars Campaign in 2015. Through this period, NASA and its academic and industrial partners started to consider seriously for the first time a long-term strategy to expand human presence permanently beyond low Earth orbit. Over this period the interest was on the human return to the Moon, with an eventual permanent establishment, and then going to Mars for exploration and then establishment. Therefore, Moon and Mars's habitats have much in common. These habitat architectures will be evaluated in terms of their solutions.

2.5.1 Early Days

Fig. 2.3 shows Garin's concept of the Mars base. This solution is a classical example of what is a pre-Integrated structure. Even if this mission architecture was restricted to an Apollo-heritage vernacular, Garin's concept is illuminating of the thinking on the differences between the Apollo heritage and the new Space Exploration Initiative. Garin's idea shows different levels of complexity not realized in many later projects. The habitat sections that lie so close to the surface exhibit an important feature of the terminal descent and landing design; the large propellant tanks, that appear in so many later lander concepts, it is not there. Alternately, Garin's lander would use a drop-stage that would detach from the main lander approximately 100 km before touchdown. Each lander offers its own Mars ascent, Earth return, and Earth re-entry vehicle all in one. The descent stage habitats would attach by inflatable tunnels, enabling the crew to walk between them in a pressurized environment. The image shows five landers. Three carry Apollo Command and Service Module (CSM), which are crew vehicles that work as Earth return vehicles. Multiple landers ensure redundancy to help mission success. Two of the landers carried cargo (photovoltaic panels and the nuclear reactor) rather than the Apollo CSM. Each lander has its own pressurized crew rover.

NASA during the 1990s developed the first Mars Design Reference Mission (MDRM 1.0). The 90-Day Study introduced two types of habitat: an "initial habitat" and a "constructible habitat." The initial habitat was comparable to the rigid structure, previously explained, currently in use for the ISS

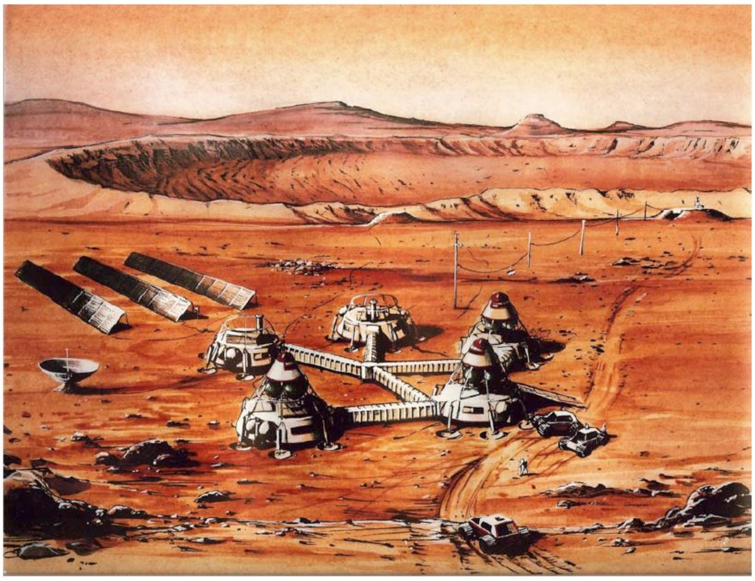

Figure 2.3: Vladimir M. Garin's "Apollo on Steroids" concept (1989) for a Mars base (Image Credit: Vladimir M. Garin).

modules. The constructible habitat was an innovative idea (**Fig. 2.5**): a spherical structure with three or four floors carried by truss work, all of it confined in an inflatable sphere. The astronauts or robots would then overlay the sphere with terraced bags or cells of regolith in order to shield from radiation and micrometeoroid protection. The initial habitat was named the First Lunar Outpost (FLO), **Fig. 2.4**, a descent/ascent vehicle (DAV) on top of a heavy lift launch vehicle. Both types of habitat could be useful on the Moon and Mars.

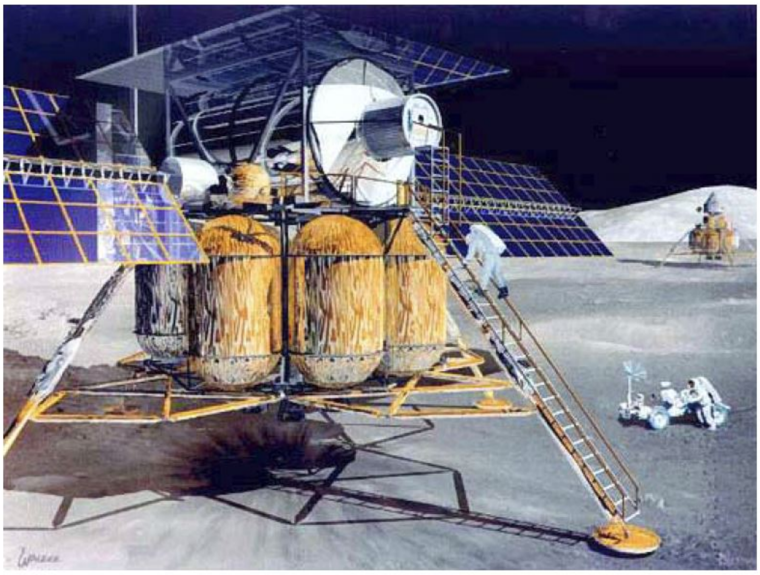

Figure 2.4: Rendering of the First Lunar Outpost (Image Credit: NASA).

Soon, it became obvious that a human mission to Mars would be the most complicated and costly single project in human history. Because of this difficulty and cost, it would inevitably become international including at least Canada, the European Space Agency (ESA), Japan, and Russia, which are also the partners on the ISS. Also, the crews would require to become involved in the design process to guarantee the propriety of the IVA (intravehicular activity) environments and EVA (extravehicular activity) equipment, to ensure their health, safety, and productivity.

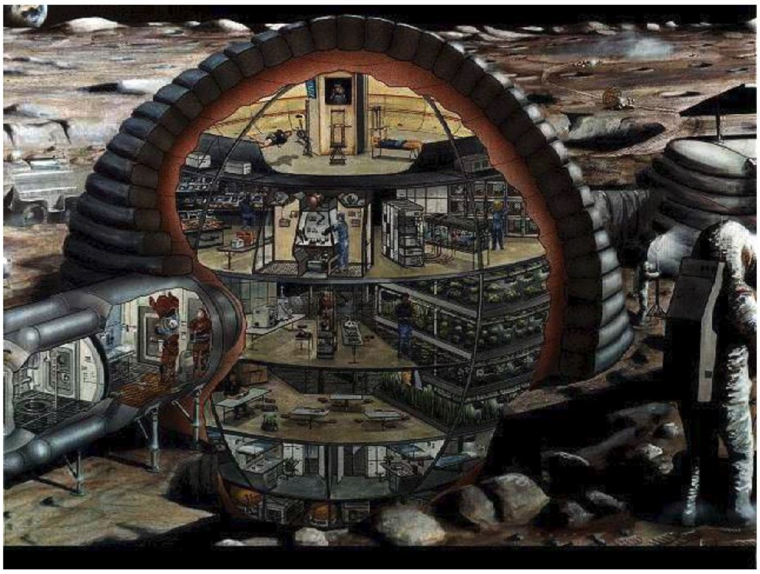

Figure 2.5: Constructible habitat for the Moon or Mars (Image Credit: NASA/Design by Gary Kitmacher, Architect/Engineer John Ciccora).

The habitat proposed by Joosten and Frassanito in "Strategies for Mars" (1993) [16] is a pre-integrated solution. The habitats will be complete and tested as fully as possible before integration into the launch vehicle. The first launch window helps for the launch of the first pre-integrated habitat-laboratory module. Because the habitat does not include EVA airlocks initially, it saves the mass penalty of the airlock from the launch. The EVA Access Modules would be launched independently and attached on site.

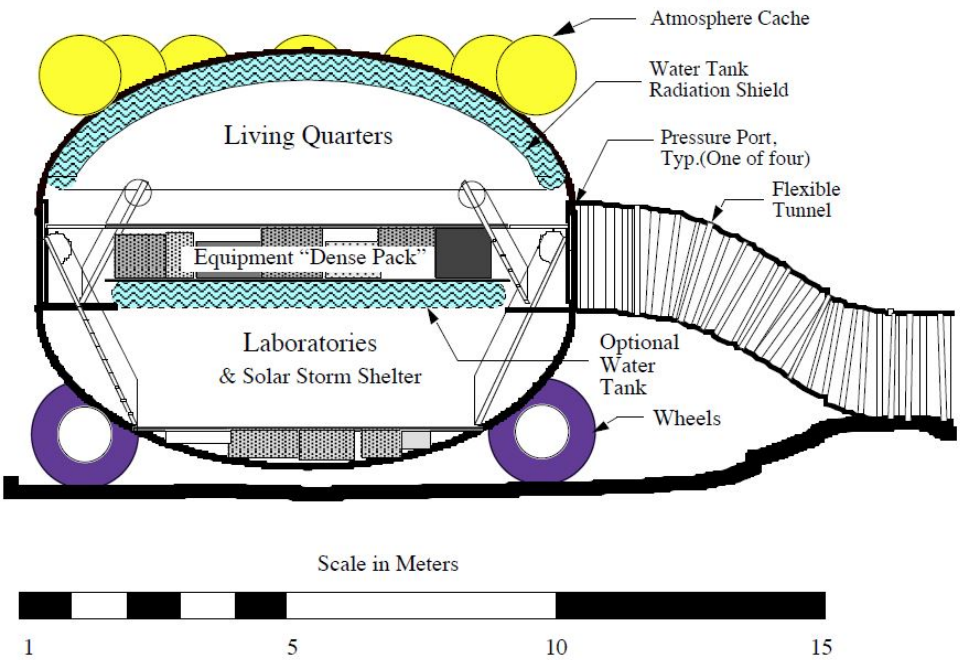

Figure 2.6: Transverse section through the "Strategies for Mars" habitat showing water radiation shielding and solar storm shelter (Image Credit: Cohen M.M.).

Each module presents four radial pressure gates, nominally ordered at 90° around the perimeter of the habitat module. These multiple pressure ports and hatches enable the attachment of at least three other pressurized modules to each habitat, also one sample airlock into which robots can put containers with specimens stored outside the habitats. The transverse section in **Fig. 2.6** presents a Mars science laboratory on the lower level. This laboratory would be where the crew study and test specimens they have recovered on excursions outside the habitat. Another use for a lower level would be an agricultural laboratory where the crew would handle experiments with plants under Mars conditions including the use of regolith for soil, water from regolith or Mars atmosphere, and of course, the Martian gravity. So the key to the Strategies for Mars Habitat are:

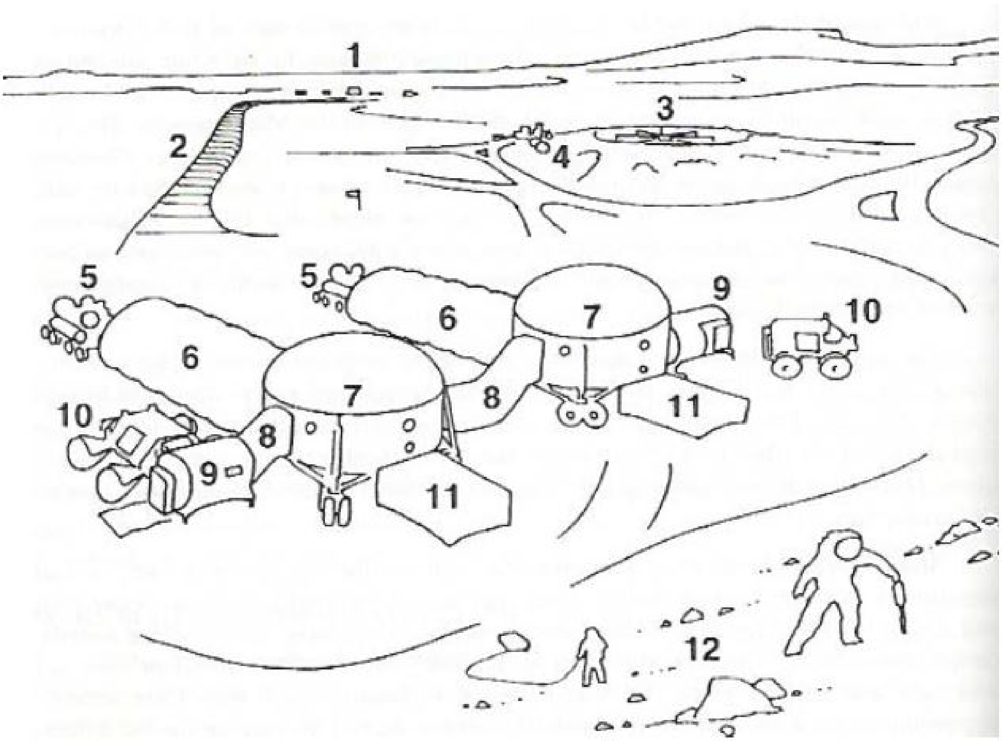

Figure 2.7: Key to the Strategies for Mars Habitat.

1. Landing Zone at least 5 km from the base for safety in case of a crash or an explosion.
2. Sintered road to the LZ on which to move the large payloads, including habitat modules.
3. Nuclear fission reactor in a crater.
4. Control facilities outside the crater.
5. ISRU production plant.
6. Inflatable greenhouse.
7. Pre-integrated habitat.
8. Flexible pressurized tunnel.
9. EVA access module.
10. Pressurized rover.
11. Scientific sample storage with robotic retrieval.
12. EVA astronauts exploring a nearby slope.

2.5.2 TransHab

NASA JSC developed an alternate solution, intended only for in-flight application, known as the Transit Habitat (TransHab) for the flight to Mars and back, but not for landing on the Mars surface. Kriss Kennedy and Constance Adams worked as the principal architects of the original inflatable TransHab concept at JSC.

The TransHab is an inflatable structure that expanded from a rigid central axial core. The crew sleep areas are on the middle floor and the galley and wardroom on the lower floor. **Fig. 2.9** shows a CAD rendering of the crew sleep services on the middle floor. The thick white cutaway walls represent the water shields containing from 5 to 10 tons of radiation protection around the TransHab. **Fig. 2.8** shows the TransHab connected to an interplanetary vehicle on its way to Mars.

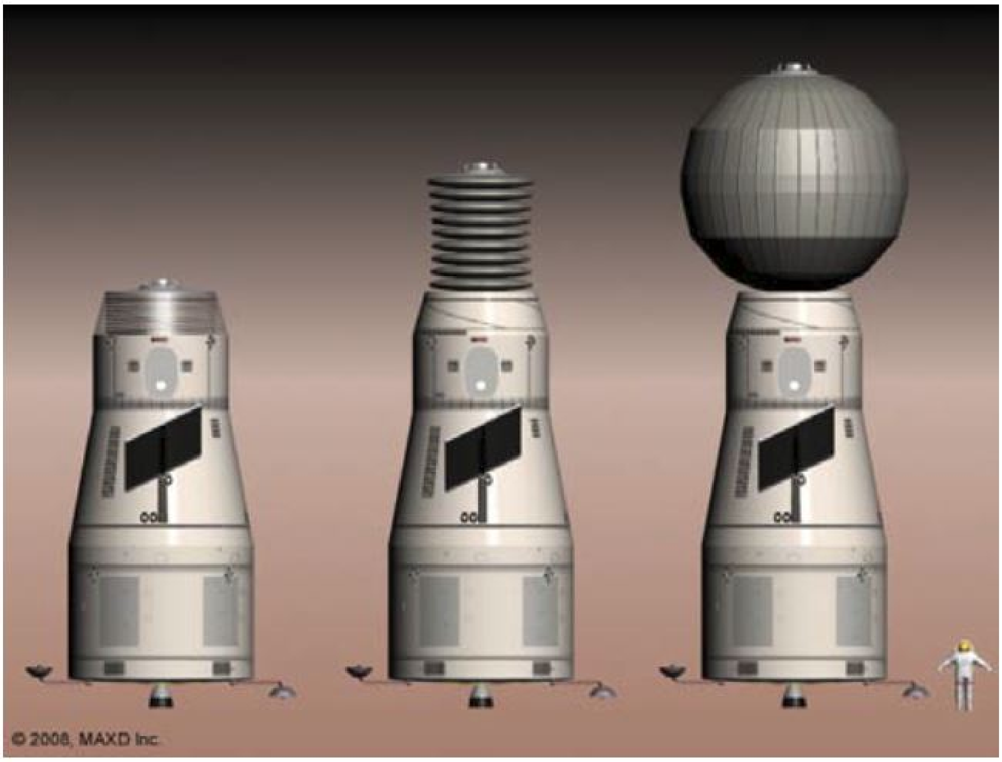

Figure 2.8: TransHab mounted on an interplanetary vehicle. (Image Credit: NNASA-Glenn Research Center)

From an architectural point of view, the TransHab is composed of four levels or floors:

- Level 4: The Pressurized Tunnel Area designed to provide a way between TransHab and any vehicle to which it is connected.
- Level 3: It hosts the exercise area.
- Level 2: It hosts the crew quarters.
- Level 1: It hosts the kitchen and the common area.

Starting from the outside side and going towards the internal one, is possible to encounter:

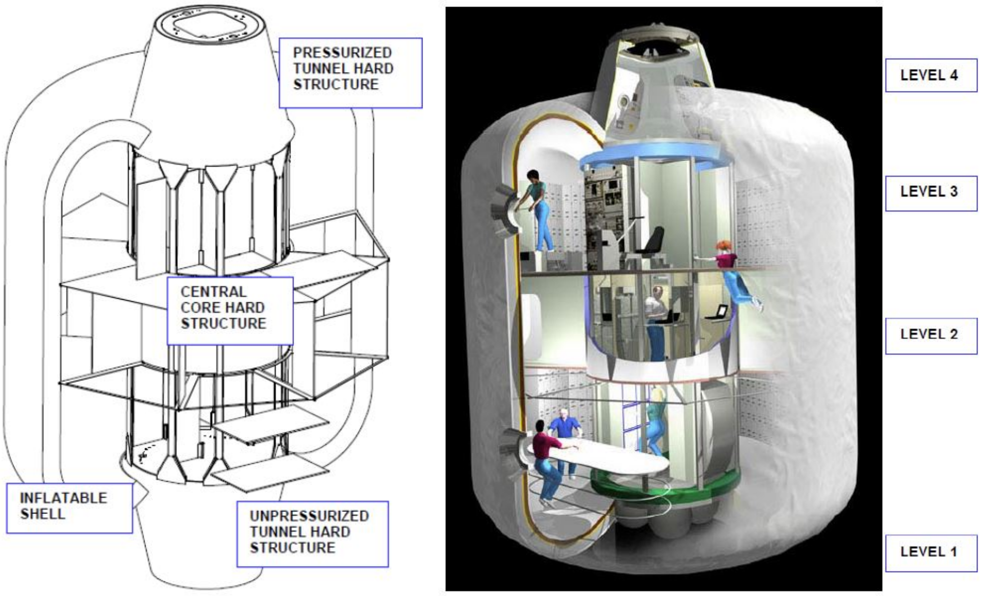

Figure 2.9: TranHab scheme. (Image Credit: NASA)

- One layer of an external thermal cover, protecting the internal structure and astronauts from the high temperature gradient recorded on the external surface (121° on lighted surfaces and -128° in shadow ones),
- Four layers of bullet-proof materials divided by open-pore foam with the aim to provide protection against micro-meteorites impacts. The idea behind this concept is the idea of the Whipple shield.
- Multiple sheets of Kevlar fabrics with the duty to be the primary structure of the inflatable part. They fix the module shape and resist the operational load caused by the internal pressure.
- Four layers of Combitherm make the module hermetic.
- An internal cut-resistance and fireproof bladder, to preserve the previous layers from unexpected scratches and flames [17].

TransHab has gained a life of its own, since Bigelow Aerospace commissioned the patent from NASA and began producing it with innovative design and new approaches to system integration. Bigelow currently has two prototype inflatable TransHab-derived habitats in LEO, Genesis I, and Genesis II. Bigelow also is produced the Bigelow Experimental Activity Module (BEAM), now connected to the ISS.

BEAM is composed of two rigid ends, which enable the connection with the rigid docking interfaces of the ISS and by an outer surface in a fabric that allows the folding of the module during the transport and storage phase. In this configuration BEAM dimensions are: 2.16 m in length and 2.36 m in diameter. Once expanded to a final pressure of 101.4 kPa, the module can reach 4.01 m in length and 3.23 m in diameter. These dimensions enable a pressurized volume of 16 m^3. Inside, the module appears as in **Fig. 2.11**.

The solution adopted by engineers to shield the module and humans from the space environment, such as radiation and micro-meteorites is a primary structure of BEAM made by flexible Kevlar-like materials, but created by the company itself, while multiple sheets of flexible fabric and closed-cell vinyl polymer foam provides the needed protection from radiation and micro-meteorites impact. But, this technology is still young, and for this reason a series of sensors were installed inside the module

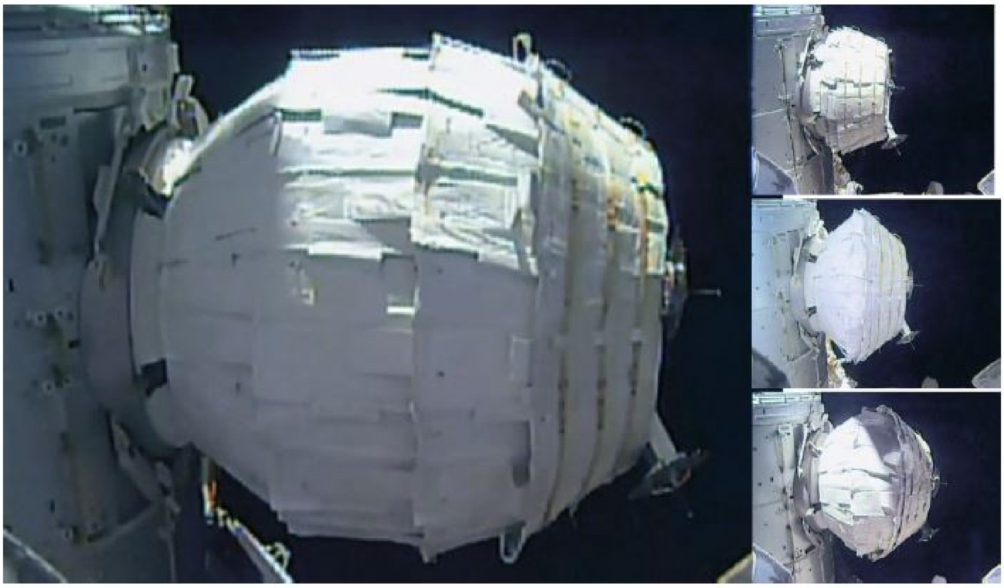

Figure 2.10: BEAM, expansion process (Image Credit: NASA).

Figure 2.11: BEAM, Inside view (Image Credit: NASA).

to validate the model calculations. The closed-cell polymer foam structure serves as a shield against micro-meteorites through the Whipple shield principle and also as a radiation shield due to the high level of hydrogen contained within the material [18].

"Whipple shields consist of a relatively thin outer bumper spaced some distance from the main spacecraft wall. The bumper is not expected to stop the incoming particle or even remove much of its energy, but to break up and disperse it, dividing the original particle energy among many fragments that fan out between bumper and wall". Thus "the original particle energy is spread more thinly over a larger wall area, which is more probable to withstand it" [19].

2.5.3 ISRU habitat

There are a lot of proposals about ISRU habitat in the literature. That's because this kind of habitat simplifies the mission profile, especially because there is a strong reduction in the mass at the departure from the Earth. The ISRU habitat uses all the resources on the target planet, giving the possibility to send from the Earth other types of resources that are not present on the target planet, which is Mars in this case. The idea proposed by Arnhof [20] is a habitat made of a rigid cylinder in the middle, with two inflatables at each end. which rise the volume and aid efficient packaging. The cylinder gives two docking ports and each inflatable provides one. Multiple exit opportunities as well as the fact, that two inflatables are attached to a rigid part in the middle, constitute the design very safe and reliable. The rigid ring additionally acts as a structural support of the cylindrical shape of the inflatables. In the case of Solar Particle Events (SPEs) it acts as a safe refuge for the crew. It will be made of a composite material called carbon-filled carbon.

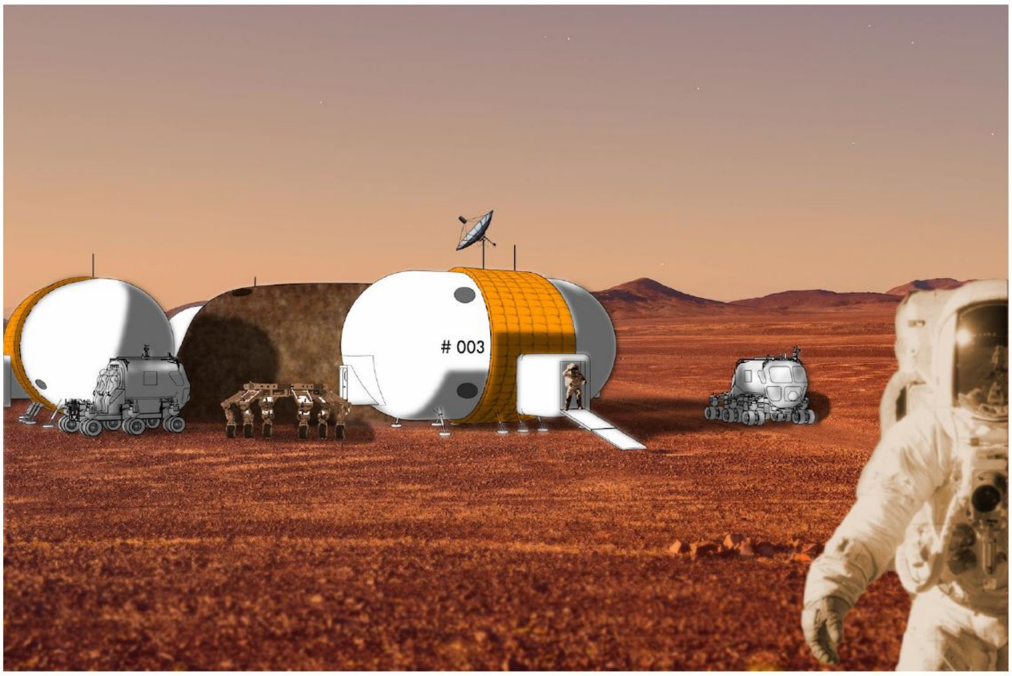

Figure 2.12: Arnhof habitat rendering (Image Credit: Marlies Arnhof).

The light elements of the polymeric fibers, in the inflatable structure, are particularly good at shielding radiation (e.g. the polymer polyethylene, with a density of 0,93 g/cm^3, with a thickness of 15 cm, succeeds to reduce radiation doses by almost 44%. It is considered as a shielding material in spaceflight better than aluminum, which is a ferocious emitter of secondary neutrons. Still, additional radiation shielding will be required to more decrease the radiation doses, in order to stay within astronauts' limits. The proposal to use in-situ regolith to shield the habitat is also a launch-mass-saving option. The simplest way to use the regolith would be in its primary or ground up form. The habitat could be easily buried under it or coated with regolith-filled bags (**Fig. 2.13**). The shielding of the central rigid ring is increased by the mounting of such bags to the outer shell, to make it safe enough in the case of SPEs. The bags provide a simple, fast and adaptable method of shielding.

2.5.4 3D-Printed Habitat Challenge NASA's Centennial Challenge

The 3D-Printed Habitat Challenge was NASA's Centennial Challenges competition to develop a 3D-printed habitat for deep space exploration, including the Moon, Mars, or beyond. The multi-phase

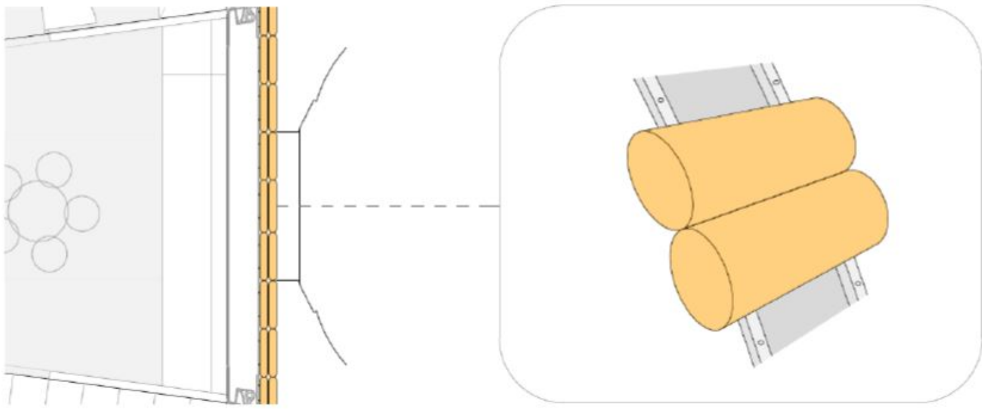

Figure 2.13: Layers of 60x20x10 cm sized regolith pillows increase shielding (Image Credit: Marlies Arnhof).

challenge was created to promote the construction techniques required to create sustainable housing solutions for Earth and beyond. The competition, completed in 2019. The challenge's phases are:

- Phase 1, the Design Competition, asked teams to offer architectural renderings and was completed in 2015.
- Phase 2, the Structural Member Competition, analyzed material technologies, requiring teams to build structural components. It was completed in 2017.
- Phase 3 the On-Site Habitat Competition, completed in 2019, claimed competitors to manufacture sub-scale habitats, and had five levels of competition – three construction levels and two virtual levels. For the virtual levels, teams used software to design a habitat that mixed allowances for both the structure and systems it must contain. The construction levels put the teams in the situation to autonomously 3D-print elements of the habitat, ending with a one-third-scale printed habitat [21].

AI SpaceFactory: MARSHA

The challenge winning habitat is MARSHA, made by AI SpaceFactory. Their idea is that Martian exploration and settlement at a significant and sustainable scale will depend on the utilization of in-situ Mars materials (ISRU). ISRU bypasses the hard limits of the rocket equation that link the total mass to the propellant mass. Without ISRU the price of carrying materials from Earth makes the project of extraterrestrial futures impossible.

"Where structures on Earth are intended essentially for gravity and wind, Martian conditions require a structure optimized to manage internal atmospheric pressure and thermal stresses. Marsha's unique vertically oriented, egg-like shape maintains a small footprint, minimizing mechanical stresses at the base and top which increase with diameter. Standing tall on the surface grants the human crew a superior vantage point to observe a dynamic landscape.

MARSHA employs a unique dual-shell scheme to isolate the habitable spaces from the structural stresses brought on by Mars's extreme temperature swings. This separation makes the interior environment unbeholden to the conservativism required of the outer shell, which retains its simple and effective form. As a result, the interior is free to be designed in the sense we take for granted on Earth – around human needs.

Figure 2.14: MARSHA rendering (Image Credit: AI SpaceFactory).

Figure 2.15: MARSHA explode CAD (Image Credit: AI SpaceFactory).

MARSHA's functional areas are spread over four levels identified by a unique interior atmosphere that encourages mobility and averts monotony. Via the large skylight above and intermittent windows, the space between the two shells acts as light-well connecting all levels with diffuse natural light. This unique space allows for a stair to arc gently from floor to floor, adding dimension to daily life.

Each level has at least 1 window, which, together, cover the full 360 degree panorama. Indirect natural light from the large water-filled skylight and intermittent windows floods the interior while still keeping the crew safe from harmful solar and cosmic radiation. Circadian lighting, designed to recreate Earthly light, is employed to maximize crew health."

AI SpaceFactory created a mixture of basalt fiber extracted from Martian rock and renewable bioplastic (PLA) processed from plants grown on Mars. This recyclable polymer composite showed properties better than concrete in NASA's strength, durability, and crush testing. ASTM lab tested and certified to be two to three times stronger than concrete in compression, the material is also five times more durable than concrete in freeze-thaw conditions [22].

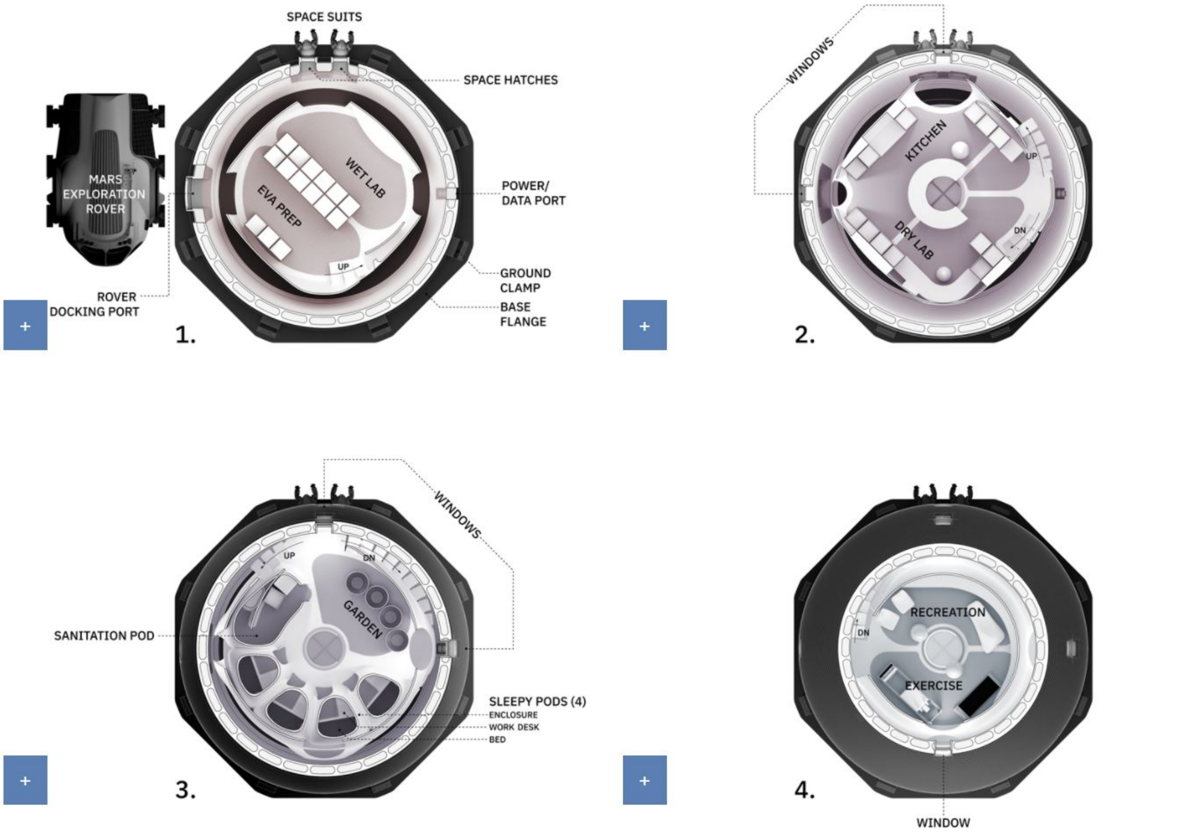

Figure 2.16: MARSHA different levels (Image Credit: AI SpaceFactory).

Martian 3Design by Northwestern University

Northwestern University suggested building a dome, the ability to create such a structure is made possible by utilizing readily available materials found across the Martian surface. The first key aspect is the internal shape of the structure which is created by printing over a unique inflatable pressure vessel. The 3D printer, proposed by the university, is lightweight, compact, adjustable, proportional to the size of the structure and easily transportable to the Red Planet. The pressure vessel will serve as the primary barrier for maintaining an internal atmosphere, which the structure itself could not hold alone. With an abundance of sulfur found in the Martian crust, Northwestern University has developed a waterless sulfur based concrete that functions as the main building block for the structure. The unique chemical composition of this concrete is optimized for the best mechanical properties resistance to radiation and performance under impulsive loadings, such as impacts from meteorites and atmospheric.

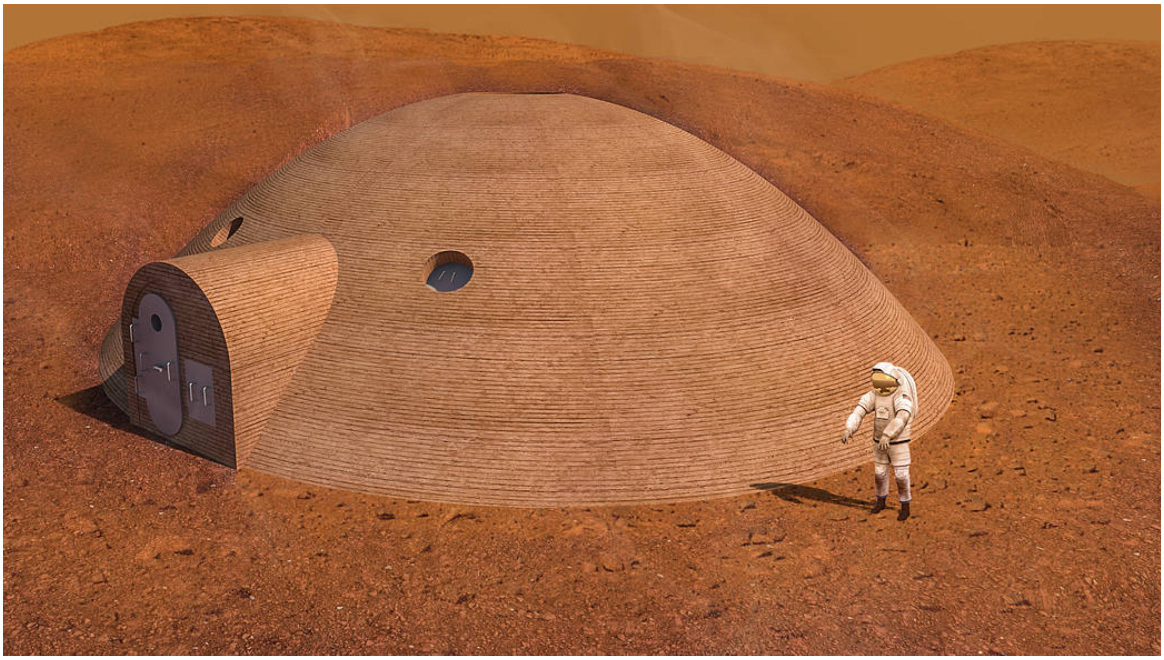

Figure 2.17: Martian 3Design (Image Credit: Northwestern University).

Chapter 3

Habitat requirements

3.1 Geometric requirements

Requirements describe the guideline for each project. This chapter summarizes and explains the chosen ones, through the analysis of their origins. It includes architectural, internal environmental, structural and departure requirements. These requirements will lead to the choice for the preliminary design.

As reported by M. Roberts "As used here, the term architectural refers to those factors that influence the volume and form of the habitat. The physical and psychological needs of humans in a confined environment must be balanced against the physical limitations of a pneumatic structure." [23].

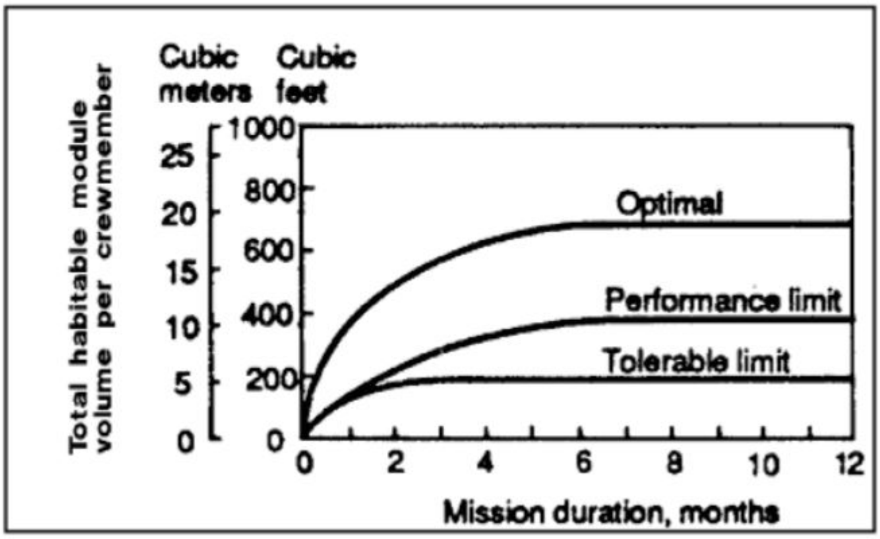

Figure 3.1: Performance level about crew member in relation to mission duration (Image Credit: NASA).

The term volume means the free space which does not include occupied volume by equipment or secondary structures. From the experience of Gemini missions, the volume per crew member can be 0.57 m^3. But this value is related to short-duration missions, where astronauts are seated most of the time, so it is necessary another value. NASA's document NASA-STS-3000 [24] gives a guideline for the habitable volume per crew member in relation to mission duration (**Fig. 3.1**). As result, for mission duration longer than 5 months the optimal level is around 20 m^3 per crew member. These data are questionable because based on "(1) a very small subject pool, (2) under limited simulated conditions,(3) with extrapolations to 12 months drawn from seven days of testing" as reported by Kriss Kennedy [25]. Considering also the project *Mars 500*, the total volume of the cylindrical module, per 6 crew member, was around 814 m^3 [26]. For these reasons, and considering a hemispherical shape for this study, a free volume per crew member of 180 m^3 is assumed, including living and working areas. Values also similar to the volume per person on the ISS. To the chosen volume, is associated with a radius of 3.5 m and in consequence a floor area of 39 m^3 approximately and a center height of 3.5 m. The chosen height is enough considering that there are not many problems due to the Martian gravity, so astronauts will not jump or fluctuate as aspected on the Moon or the ISS. The hemispherical shape is also a choice related to the material considered in this thesis, which permits a foldable structure easy to transport.

3.2 Environmental requirements (ECLSS)

Since this structure is designed to host humans, other requirements are needed to guarantee a suitable environment for them. This includes the proper pressure, temperature, humidity and all the other features which are indispensable to allow human life. However these features are fundamental, they represent additional requirements that the habitat structure has to satisfy. Nevertheless, a life support system similar to the Environmental Control and Life Support System (ECLSS) on ISS must be inserted in the mission payload, as the most efficient strategy to restrict the needed input of resources and to permit the recycle of the resources.

3.2.1 Internal pressure

Considering that the total pressure of a mix of non-reacting gases is equal to the sum of the partial pressure generated by the individual gas. Partial pressure is the pressure of the single gas, when is alone in the same volume filled by the mix. To support the respiration and maintenance of natural functions of the human body the partial pressure of oxygen has to be considered otherwise the barometric pressure (total pressure) of the environment. So the partial pressure of the oxygen must be higher than 0.114 atm. To understand better the focus on this value, the minimum barometric pressure which inhibits ebullism, (spontaneous boiling of body tissues) is 0.06 atm. This is also the value related to the saturated vapor pressure of water at body temperature. But even carbon dioxide is in our blood. To allow respiration the carbon dioxide partial pressure must be 0.048 atm because a pressure gradient must exist between oxygen and carbon dioxide. The resulting ambient pressure is higher than 0.114 atm. This pressure could be provided by oxygen alone, resulting in a single gas environment or by multiple gases as on the Earth. Despite that, as already mentioned the partial pressure of the oxygen is relevant and not the environment barometric pressure. Therefore an environmentally suitable pressure for human life can be reached with a single-gas atmosphere or with a more complex dual-gas atmosphere (oxygen-nitrogen). However, a single gas environment enriched in oxygen leads to a big danger of fire leads to numerous problems, in particular, if the barometric pressure is major than the hypobaric level. This was the case in the Apollo 1 disaster, where a 100% oxygen cabin environment was momentarily increased to 1.08 atm for a test on the launch pad but a spark started a fire burning the three astronauts in the cabin. Today all the modern vehicle's cabin and modules have an oxygen-nitrogen atmosphere. The atmosphere pressure on Mars is only 600 Pa while on Earth is 101325 Pa (1 atm) at sea level. Because the habitat must simulate the conditions on Earth, it must be set to a minimum of 0.78 atm, resulting in a pressure difference of 80,000 Pa. These forces must be counterbalanced by the habitat shell. The gravity on Mars is 0.375 times the one on Earth, which means that about three times more mass is required on Mars to counterbalance an equal pressure difference. Materials with high tensile strength could neutralize a part of the pressure difference [27].

3.2.2 Thermal control

Temperature and humidity are two features closely linked between them because the perceived temperature strongly depends on the humidity level. Although, because of the low atmospheric density on Mars, convection and conduction are less influent than radiation, with temperature fluctuation between -130° C and 30° C [28]. The Mars habitat will dissipate heat that is needed to keep internal habitability for the crew. With an accurate thermal insulation design, it should be possible to guarantee that the base does not generates more heat than it dissipates. Indeed, electrically powered equipment transmits heat inside the base. This heat is transferred to the soil, the atmosphere and is radiated. The thermal insulation design must support possible large fluctuations in the temperature of the soil, as it can warm up if in touch with heat-emitting equipment such as power units, and for heat exchange with the atmosphere. According to Edgardo Farias et al. [29] [27] 1 m of Martian regolith, with approximation, will be sufficient to ensure thermal insulation. Other materials such as Aerogel or fiberglass blanket, with small thickness, are considered a good solution for insulation.

As reported above humidity has a big influence on the perceived temperature and human comfort. As it occurs in the desert vs. jungle, the temperature may be very comparable but the second is more uncomfortable than the first one. The motivation is the different level of humidity. With the raising or decreasing of the temperature, humidity affects significantly. At high temperatures a low level of humidity is better, helping evaporative cooling used by the body, while at low temperatures high humidity is helpful to reduce evaporation and help heat preservation. The cabin atmosphere is usually kept at about 60% relative humidity (corresponding to about 0.2 psi of water vapor pressure) [30].

3.3 Noise and vibrations

The launch ad re-entry phases vibrations are not the primary health matter for crew members of a space module or of a space launcher. The principal source of vibration, like turbulence, is absent in space, due to the absence of atmosphere. Separately from vibrations, noise is rather a bigger affair in space. A larger source of noise and vibration in the missions are the avionics and other equipment: pumps, fans, compressors, and other of this type. "At noise levels above 50 dB, most people must raise their voices to be heard and find the ambient noise annoying. Above 65 dB, temporary threshold shifts are seen and sleep is impaired. Above 75 dB, performance degradation is seen. Obviously, for space travellers - especially those on long duration missions - noise and vibration control mechanisms can be very important for long term health and mood." [30]. The operation effects related to noise are a problem for astronauts and their risk changes with the duration and intensity of it. For this reason a value of 50 dB is chosen as the highest admissible level of noise for the habitat preliminary design.

3.4 Shielding surface

As already exposed in the previous chapter, the first type of radiation is Cosmic Galactic Radiation (CGR) and the second is Solar Particle Events (SPE). The CGRs are constant radiation in the Universe, created by supernova remnants. The SPEs come from the Sun and are a consequence of Coronal Mass Ejections (CME). SPE radiation is further energetic than CGR and can be lethal to astronauts in a short time frame while GCR raises the risk of deadly cancers over time. On the contrary to CGR, which is constant, high levels of SPE radiation only occur punctually and are predictable. The measurements reported by RAD instrumentation indicate that an astronaut would be exposed to a CGR dose equivalent to about 131.4 mSv per trip during a nine-month between Earth and Mars and to 184.32 mSv for a 288-day mission on Martian surface. This lead to a total estimated radiation of 447.12 mSv in a 835-day interval. This result is problematical reflecting on NASA guidelines which specify that the exposure limit during an astronauts career should not raise the chance of cancer by more than 3%, which corresponds to an annual dose of 500 mSv considering crew members of all genders and ages. In the case of 25 year old females, the most sensitive to radiation, a career dose of 400 mSv is the maximum admissible. For SPE radiation, the method currently applied to shield a crew against it is to repair in the airlocks until the radiation comes back to safe levels. This normally takes a day or two and it is possible to inform the crew shortly before the radiation levels rise up.

3.5 Structural requirement

This section gives all the requirements linked at the structure such as safety factor, load case and maximum stresses permitted in all MadFlex layer. Safety Factor (SF) is one of the most important structural parameters because it describes the past knowledge and experience that engineers have concerning the material's behaviors adopted for the structure, and on environmental features that determine the external load conditions. The safety factor on Earth is in a range between 1.7 and 3.5. All of the problems and uncertainties on other planets will certainly require higher safety factors, so a SF of 4.0 or higher seems reasonable [31].

3.5.1 Load condition

The structure must endure the following load case, satisfying both sturdiness and stiffness criteria. The description of these criteria is reported in the next paragraph.

Load conditions:

1. Internal pressure of 1 atm ($1.013 \cdot 10^5$ Pa) only;
2. Internal pressure of 1 atm ($1.013 \cdot 10^5$ Pa), plus regolith cover load (regolith thickness: 1.650 m of W50 regolith);
3. Regolith cover load only (regolith thickness: 1.650 m of W50 regolith);
4. Load used to keep the habitat in the folding configuration.

The regolith thickness chosen is a compromise in order to not have a high regolith load on the structure, plus the W50 regolith is present in a vast area of the planet and has a good percentage of water that helps to better shield the structure. This thickness assure an equivalent dose per year of 50 *mSv* and considering that the limit in an astronaut career is 500 *mSv* it will ideally permit a 10 years mission. The structure must resist the regolith load without the help from the internal pressure. This requirement is fundamental since it describes an emergency or organized de-pressurization of the module where the structure has to avoid the habitat collapse, keeping the astronauts safe.

3.5.2 Sturdiness criteria

Sturdiness indicates the capability of the structure to resist the ultimate load without breaking. Ultimate load is the maximum expected load on the structure through its operational life, multiplied by a designated safety factor. This imposes to confirm that the internal stresses of the structure, caused by the ultimate loads for each load case, are lower than the ultimate strength of each material that composes the structure. It is important to know that materials behavior and type of collapse are different in case materials are in traction or compression, since precisely requirements are necessary for each of them.

Dyneema

- Tensioned: Internal stresses caused by the ultimate load must be lower than the ultimate tensile strength reported on the material's datasheet.
- Compressed: When compressed, Dyneema layers in the MadFlex enter the buckling condition, therefore the criteria is not required.

Foam

- Tensioned: Internal stresses caused by the ultimate load must be lower than the ultimate tensile strength reported on the material's datasheet.
- Compressed: Internal stresses caused by the ultimate load must be lower than the ultimate tensile strength reported on the material's datasheet.

Carbon

- Tensioned: Internal stresses caused by the ultimate load must be lower than the ultimate tensile strength reported on the material's datasheet.
- Compressed: Considering that the MadFlex is a sandwich material, when compressed, the carbon layers break due to "face wrinkling", before reaching the ultimate compressive strength. Consequently, internal stresses generated by the ultimate load must be lower than the critical buckling stress ($\sigma_{b,i,x}$ or σ_{Ho}) of the carbon. This latter value is calculated with the following two empirical formulas:

  1. First empirical formula:

  $$\sigma_{b,i,x} = \frac{2}{3}(E_{c,i,x} \cdot E_{3,z} \cdot \frac{t_i}{t_3})^{0.5} \tag{3.1}$$

  "wherein: t_i is the thickness of the outer layer (carbon). $E_{c,i,x}$ is the compression elasticity module of the same outer layer [...]; t_3 is the thickness of the intermediate layer (foam) and $E_{3,z}$ is the compression elasticity module of the intermediate layer, in the direction of the thickness in accordance with ASTM C365 / C365M standard" [32].

  2. Second empirical formula:

  $$\sigma_{Ho} = 0.5 \cdot (E_f \cdot E_c \cdot G_c)^{\frac{1}{3}} \tag{3.2}$$

  Where the index "f" means the face of the sandwich, while the index "c" the core [33].

To meet the previous requirement on critical buckling stress of the carbon layers, stresses inside the carbon must be lower than only one of the two values calculated by the empirical formula.

3.5.3 Stiffness criteria

Stiffness is the capability of a structure to avoid large deformation under ultimate load. This requirement is applied to the arch and one the floor or tie of the arch.

- Arch: Under the ultimate load, the deformation of the structure must allow the movement of the astronauts inside it and do not compromise the shape of the radiation shielding made with the regolith bags or other types of solutions.
- Tie of the Arch: It must have sufficient stiffness to avoid excessive deformation of habitat floor under ultimate load, this could be a problem in the case of internal pressure. An excessive deflection of the floor could compromise the equipment inside the module.

3.6 Payload requirement

The launcher considered right now, for missions toward Mars, is the Space Launch System (SLS), surely in the future even the Space-X Starship will contribute to the exploration of the Red Planet. "The Space Launch System (SLS) is a super heavy-lift expendable launch vehicle, which has been under development by NASA [...]. It will be the primary launch vehicle of NASA's deep space exploration plans, including the planned crewed lunar flights of the Artemis program and a possible follow-on human mission to Mars." [34]. The size and weight of the habitats must be optimized to allow the stowage of the largest number of habitats inside the launcher with all the necessary types of equipment in order to minimize the costs and number of lunch toward Mars.

3.6.1 Fairing geometry

The estimated diameter of the faring draws the maximum transversal dimension of a payload representing a limit for the dimension of the Martian habitat took in the study and the number of them that can be stowed. "Impacts of Launch Vehicle Fairing Size on Human Exploration Architectures" [34] describe three different fairing ideas for exploration missions that the SLS launcher can fit:

1. SLS block 1B cargo 2: 8.4 m (27.6 ft) with an internal diameter (value of interest) of 7,5 (24.6 ft);
2. SLS block 1B cargo 2: 8.4 m (27.6 ft) with an internal diameter (value of interest) of 7,5 (24.6 ft);
3. SLS block 2: 10 m (32.8 ft) with an internal diameter (value of interest) of 9,1 m (29.9 ft) [35].

The 1. and 2. concepts differs instead in other parameters such as height and volume. Faring heights of the SLS launcher, in according to [34] for the three different faring concepts, are:

1. SLS block 1B cargo 2: 19,1 m (62.7 ft);
2. SLS block 1B cargo 2: 27,4 m (90 ft);
3. SLS block 2: 27,4 m (90 ft).

The total usable volume for the payload, in the three mentioned configuration is:

1. SLS block 1 cargo: 229.9 m3 (8118 ft3);
2. SLS block 1B cargo: 621.1 m3 (21930 ft3);
3. SLS block 2: 988 m3 (34910 ft3)

Reported in detail in **Fig. 3.1**.

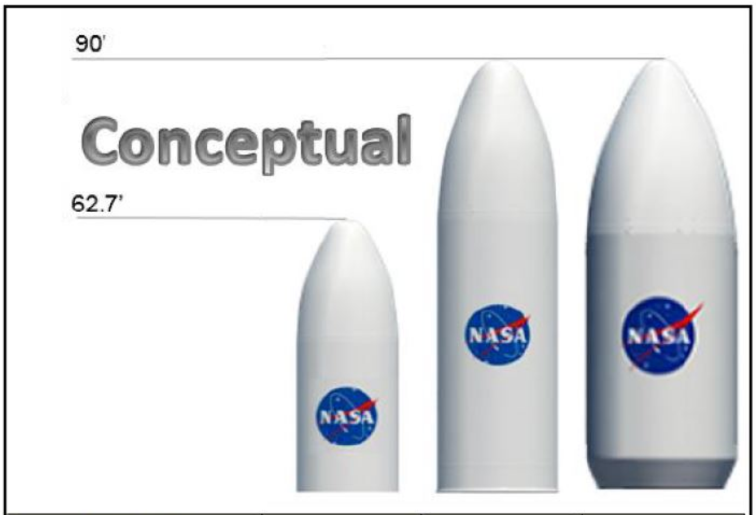

Payload Accommodation	8.4m Short	8.4m Long	10m
Type	8.4m PLF	8.4m PLF	10m PLF
SLS Block Effectivity	1B & 2	1B & 2	2
Length	62.7 ft	90 ft	90 ft
Diameter	27.6 ft	27.6 ft	32.8 ft
Internal Diameter	24.6 ft	24.6 ft	29.9 ft

Figure 3.2: SLS fairing concepts for exploration missions. (Image Credit: "Impacts of Launch Vehicle Fairing Size on Human Exploration Architectures").

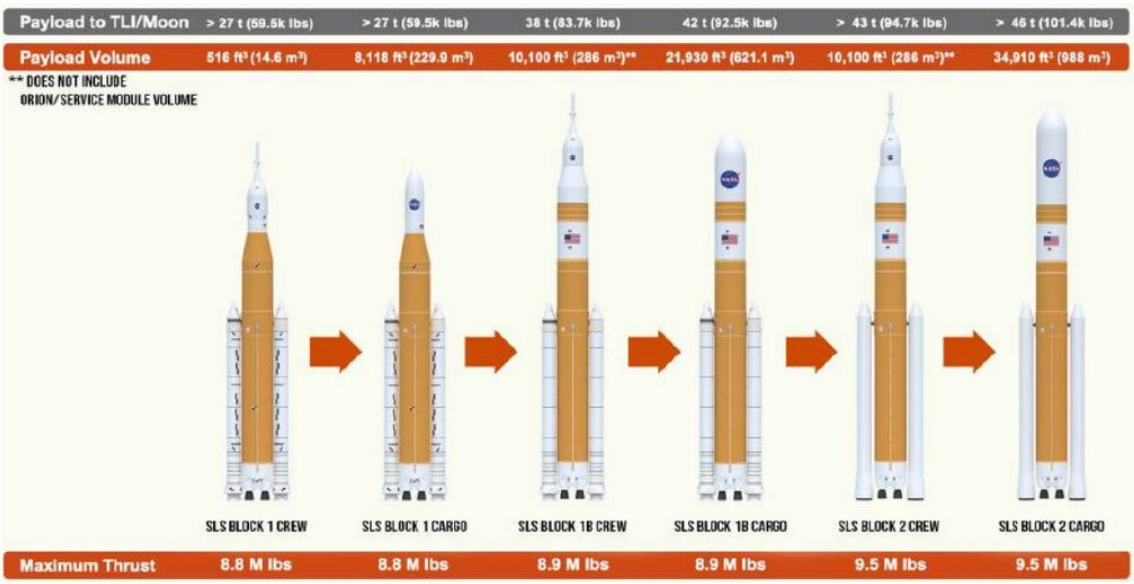

Figure 3.3: SLS evolution (Image Credit: NASA).

3.6.2 Available mass

The maximum payload's mass and depends on the developable trust of the launcher and the mission target (Moon L2, Mars or other planets). The maximum mass for the three mentioned launcher configurations are:

1. SLS block 1 cargo: 27 ton (59.5k lbs);
2. SLS block 1B cargo: 42 ton (92.5k lbs);
3. SLS block 2: 46 ton (101.4k lbs) [35].

3.6.3 Vibrations

To avoid resonance during the departure, which is catastrophic, the resonance frequency of the payload must be far from the ones generated by the launcher systems and atmospheric phenomena.

Chapter 4

The Madflex

4.1 An innovative material

The Madflex is an innovative material created by the Composite Research (CoRe). It is a composite material having a sandwich-like structure. The particular behavior of this sandwich structure then the other in commerce is to be crushproof if loaded on one side and flexible, even rollable, if loaded on the other one. Here, better than words, is shown the material in the two configurations with two different load conditions [36]

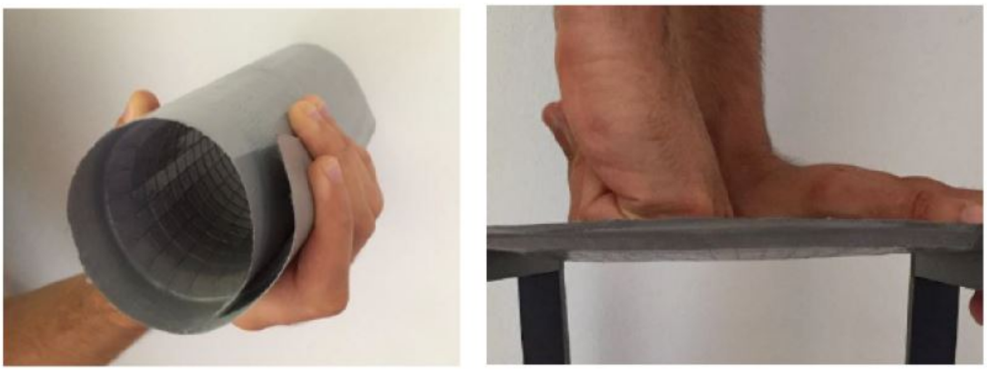

Figure 4.1: Madflex's behaviour (Image Credit: CoRe).

The materials employable for the construction of the two skins can be of a different kind such as carbon fibers, Kevlar, aramidic fibers and many others. The benefits of the MadFlex are the following ones:

- Temperature resistant.
- Anti-seismic.
- Resistant to chemical agents.
- Fireproof
- Possibility to avoid complex and expensive mechanisms to create folding parts
- Endless surface finishing

- Structural strength: On the rigid side, when it is loaded, allows high structural strength. Representative values about MadFlex mechanical properties, from the structural tests, are reported in **Tab. 4.1**:

	Bending stiffness rigid side [Nm^2/m]	**Bending stiffness rollable side [Nm^2/m]**	**Tensile strength [KN/m]**	**Flexural strength [MPa]**	**Flatwise compressive strength [MPa]**
Test Method	ASTM D7250/D7250M	ASTM D7250/D7250M	ASTM D3039/D3039M	ASTM D7250/D7250M	ASTM C365/C365M
Max value configurations	250	2.0	700	450	2.4
Min value configurations	13	0.1	350	95	1.2

Table 4.1: Madflex Mechanical Properties (Source: CoRe).

- Lightness: Related to rigid materials, for example aluminum, it gives the same deflection, under the same load (200 Kg) with a total weight of only 1.7 kg compared to 7.8 kg of aluminum. "It is 5-6 times lighter than a sheet of ABS (polymer material) of the same flexural rigidity and 3-4 times lighter than a sheet of ABS of the same flexural resistance" [36] (**Fig. 4.3**).
- Thermic insulating: Insulating capacity is over 5 times higher than an ABS panel (**Fig. 4.4**).
- Environmental friendly material: the CO_2 released during the production process of this material is very low. The greenhouse gases liberated into the environment are about half of those delivered to produce an ABS panel with similar mechanical properties.
- Thermoformable: It possible to give to the Madflex the desired shape, simply utilizing molds. An example is shown in **Fig. 4.2**.
- Easy to transport: Thanks to its properties to be rollable on one side it can be collected and transported in a very small volume, representing a good solution for deployable structures.

  As discussed before Madflex can be created with different materials to satisfy the design necessities of each project. For these motivations the types of Madflex developed are numerous and the table below shows the mechanical properties of only a part of them. The data about the other MadFlex types are reported in the MadFlex Book [36].

Figure 4.2: While making a Madflex curved panel.

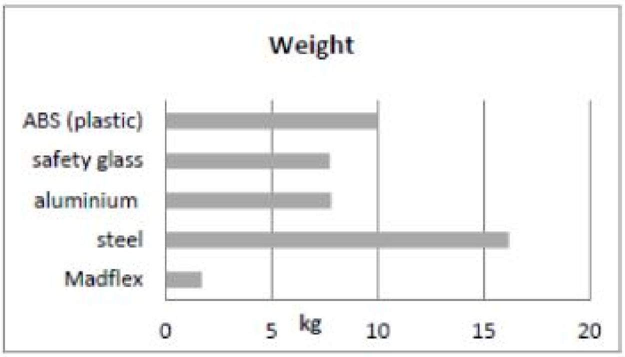

Figure 4.3: Lightness of 1 m^2 sheets in different materials and with the same deflection under a load of 200 N. (Image Credit: CoRe).

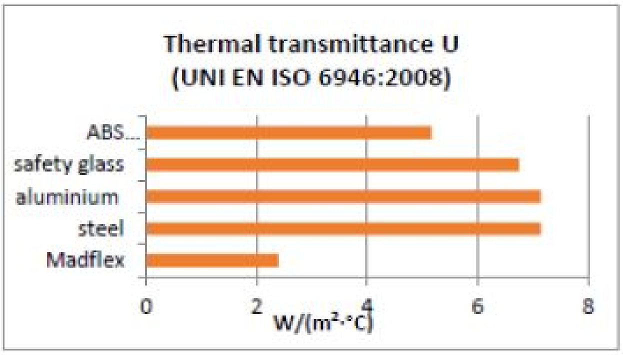

Figure 4.4: Thermal trasmittance of 1 m^2 sheets in different materials and with the same deflection under a load of 200 N. (Image Credit: CoRe).

	Unit	Typical value	Test
Thickness	mm	5	
Areal weight	kg/m^2	1.3	
Tensile strength	kg/m	500	ASTM D3039/D3039M
Failure bending moment	Nm/m	170	ASTM D7250/D7250M
Bending stiffness "rigid side"	Nm^2/m	30	ASTM D7250/D7250M
Bending stiffness "rollable side"	Nm^2/m	0.5	ASTM D7250/D7250M
Flatwise compressive strength	MPa	1.7	ASTM C365/C365M
Heat transfer coeffcient	W/m^2K	7.5	DIN52612

Table 4.2: MadFlex 1.0 It is the first type of Madflex produced by CoRe and led to the filing of the MadFlex patent.

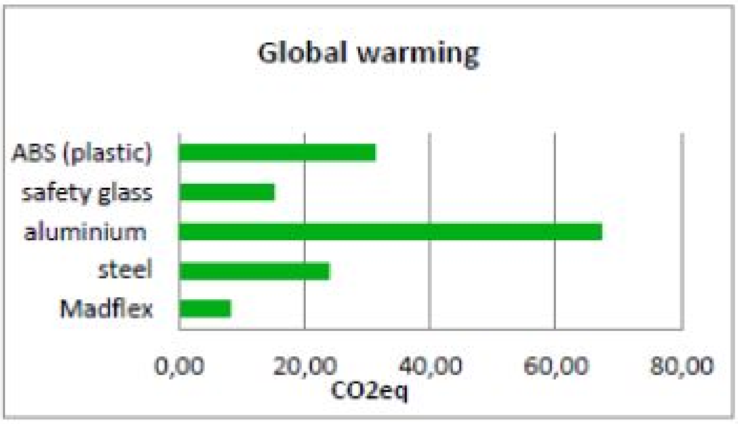

Figure 4.5: CO_2 emitted for the production of 1 m^2 sheets in different materials and with the same deflection under a load of 200 N. (Image Credit: CoRe).

	Unit	Typical value	Test
Thickness	mm	11	
Areal weight	kg/m^2	1.8	
Tensile strength	kg/m	700	ASTM D3039/D3039M
Failure bending moment	Nm/m	480	ASTM D7250/D7250M
Bending stiffness "rigid side"	Nm^2/m	240	ASTM D7250/D7250M
Bending stiffness "rollable side"	Nm^2/m	1.5	ASTM D7250/D7250M
Flatwise compressive strength	MPa	1.5	ASTM C365/C365M
Heat transfer coeffcient	W/m^2K	3.6	DIN52612

Table 4.3: Maximum Structural Performances It is able to replace structural metallic part.

	Unit	Typical value	Test
Thickness	mm	6	
Areal weight	kg/m^2	1.65	
Tensile strength	kg/m	450	ASTM D3039/D3039M
Failure bending moment	Nm/m	230	ASTM D7250/D7250M
Bending stiffness "rigid side"	Nm^2/m	40	ASTM D7250/D7250M
Bending stiffness "rollable side"	Nm^2/m	0.6	ASTM D7250/D7250M
Flatwise compressive strength	MPa	1.7	ASTM C365/C365M
Heat transfer coeffcient	W/m^2K	6.2	DIN52612

Table 4.4: Cut Resistant it is able to withstand cut and perforation damages

4.2 Structural consideration

The Madflex is an asymmetrical sandwich structure. The asymmetry is due to three different factors:

	Unit	Typical value	Test
Thickness	mm	5.5	
Areal weight	kg/m^2	1.75	
Tensile strength	kg/m	500	ASTM D3039/D3039M
Failure bending moment	Nm/m	225	ASTM D7250/D7250M
Bending stiffness "rigid side"	Nm^2/m	55	ASTM D7250/D7250M
Bending stiffness "rollable side"	Nm^2/m	0.4	ASTM D7250/D7250M
Flatwise compressive strength	MPa	1.7	ASTM C365/C365M
Heat transfer coeffcient	W/m^2K	7.2	DIN52612

Table 4.5: Another Madeflex's version cut resistant has the following mechanical properties

- Distinctive materials for the upper and lower skins of the sandwich.
- Different thickness of the skins, even using the same material for both skins.
- Both of the previous considerations together.

Madflex can be classified as an asymmetric material especially for the third point in the upper list. The different behavior in traction and compression of the skins give to the MadFlex the capabilities to be rollable on one side and rigid from the other one:

- One skin is composed of materials with great elastic modulus, in traction and compression, consequently, the skin can develop high resistance in these two cases. The materials principally used to realize this skin are Carbon fiber, reinforced with polymer, and glass fibers.
- The other skin is made from materials capable of high resistance in traction but to oppose a very low one when compressed. How these materials can have two different behaviors is described at the end of this chapter because it is not linked only to a simple mechanical feature. Materials used to obtain this skin are mainly Dyneema and aramidic fiber.

Analyzing the mechanical behavior of the entire MadFlex in bending configuration, two load cases can be identified:

- If the asymmetric sandwich is loaded on the rigid side (**Fig. 4.6**), the rigid skin (green) is in compression and the flexible one (red) in traction. This allows the sandwich to resist high loads thanks to the high compression resistance of the rigid skin and the high resistance to the traction of the other one. In this load case, the flexible skin contributes to the overall flexural stiffness of the entire structure.
- If the sandwich is loaded on the flexible side, rigid skin is in traction but the flexible one in compression. Nevertheless, the flexible skin cannot resist the compression and consequently the sandwich folds, under very low loads. In this load case, the flexural stiffness of the flexible skin can be ignored when it is calculated the overall one. The sandwich can be thought composed of only two layers.

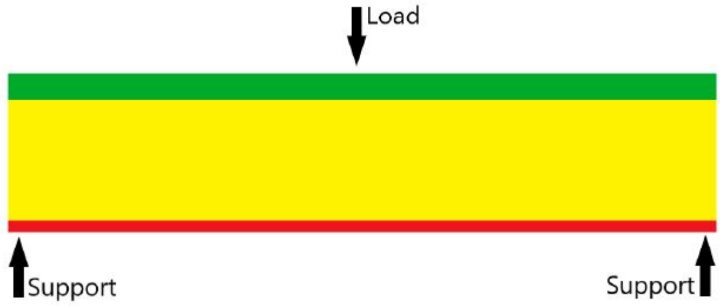

Figure 4.6: Load case with rigid side in compression and flexible side in traction

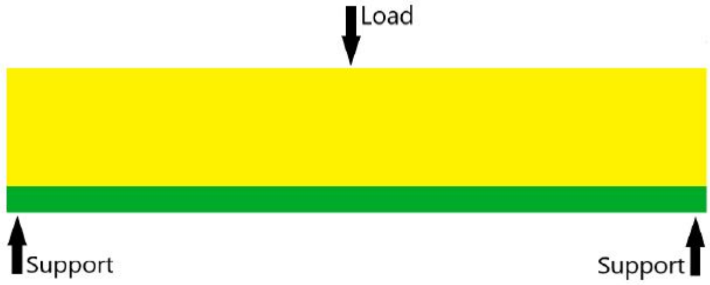

Figure 4.7: Load case with rigid side in traction and flexible side in compression, which is negligible.

So it is clear that in one configuration the structure is capable to resist and remain rigid but in the other case, it is highly flexible with low stiffness allowing to fold it. This second case is possible thanks to the movement of the flexural neutral axis, or the centroid, near or inside the rigid skin letting smaller radii of curvature than the case in which the structure is entirely rigid. To explain in detail, each material subjected to a bending moment, develop a curvature following the expression:

$$M = EI \cdot k \tag{4.1}$$

where M means the bending moment, EI the bending stiffness and k the curvature equal at 1/r (where r is the radii of curvature). This expression comes from the Eulero-Bernulli beam theory for a homogeneous and isotropic material.

Considering a constant moment the higher is the bending stiffness the lower will be the curvature, for this reason, stiffer materials develop lower curvature with higher bending radii and vice versa. Materials usually used in structures have only one value of bending stiffness and develop the same curvature if loaded on both sides. The Madflex alternatively can have this dual behavior thanks to the possibility to show two different values of bending stiffness depending on the load case, which defines the contribution or not of the flexible skin at the overall bending stiffness. Therefore the curvatures and the radii developed are different.

The low resistance developed by the flexible skin once in compression is due to the possibility to make skin supple. This can be achieved by using something that is usually viewed as a defect or issue to avoid in the design phase of the material: the local buckling of a skin. In the case of buckling the type of load is the only compression and a sandwich skin can fail due to this types of local instability:

- Dimpling: "A sandwich with a honeycomb core may fail by buckling of the face where it is

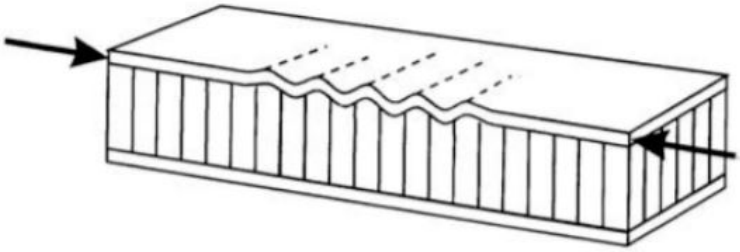

Figure 4.8: Dimpling. (Image credit: Achilles P., Design of sandwich structures)

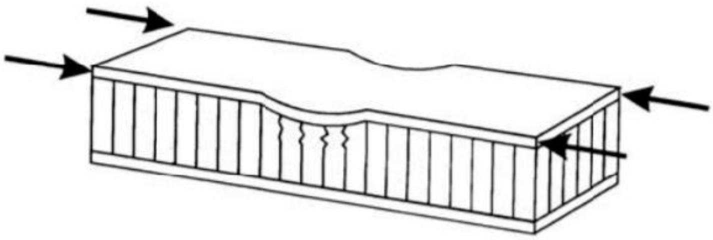

Figure 4.9: Wrinkling. (Image credit: Achilles P., Design of sandwich structures)

unsupported by the walls of the honeycomb core" [37].

- Wrinkling: "Face wrinkling is a buckling mode of the skin with a wavelength greater than the cell width of the honeycomb core under compression load" [37].

This particular behavior of the skin can be facilitated by the following factors:

- an elastomeric matrix to concede the fiber deformation;
- a lower thickness of the compressed skin;
- a lower density of the core.

The reversible buckling is the main factor that leads to the double mechanical behavior presented by the Madflex. It can be obtained by applying the previous ideas in an intentional and controlled manner. **Fig. 4.10** and **Fig. 4.11** show the buckling mode mentioned applied to the MadFlex.

While to better explain the behavior of the rigid skin is important to know that the materials, which MadFlex rigid skin is made, have a high resistance in compression, but, as with all panels, or beams, with small thickness, even for them the critical issue of the global buckling load, occurs before the ultimate compressive strength. To bypass this event the foam and the junction glue, have a crucial role. Thanks to them the rigid skin can reach the buckling load and resist higher load once compressed. But, because MadFlex is a sandwich-like material great attention is also needed for the other skin failure modes previously mentioned, especially when they are not intentional. The most crucial failure mode for the rigid skin attached to a foam is the wrinkling which restricts the maximum applicable compressive load [30].

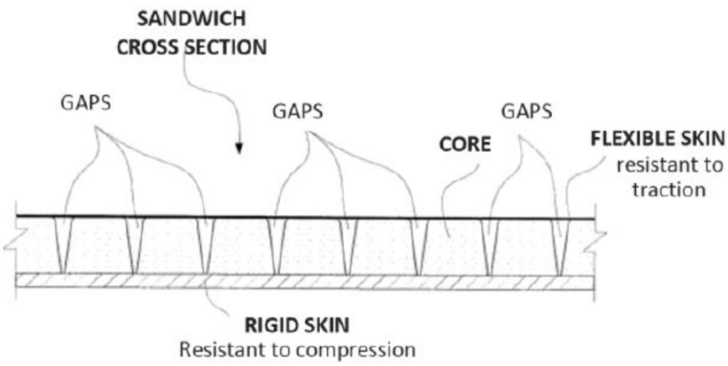

Figure 4.10: MadFlex, section view. (Image credit: CoRe)

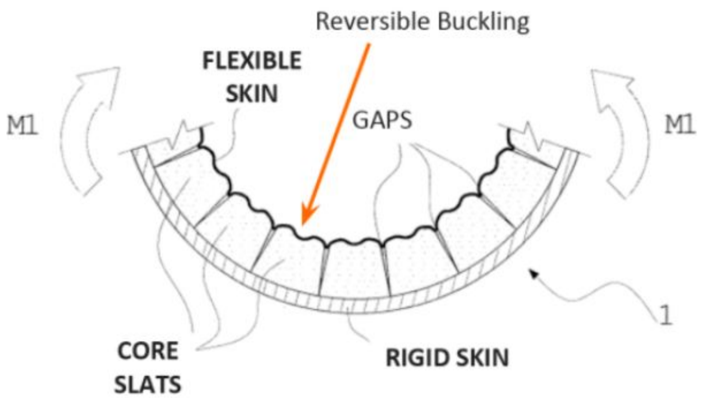

Figure 4.11: MadFlex, section view in bending configuration. (Image credit: CoRe)

Chapter 5

Preliminary design

A preliminary design is needed to develop in order to understand how MadFlex could be used in a better way, especially in a way that other common materials could not fulfill. The design will take advantage of the particular MadFlex behaviors. The fundamental requirement is the folding and deploying of the structure, a goal that MadFlex can satisfy, being flexible on the "soft" side and rigid on the other, assuring a structural resistance. Even if the MadFlex proves the great ability to be flexible on one side and rigid on the other side, is not a simple task to use to design a deployable habitat. The chosen concept should satisfy the following criteria:

- Packaging: the ability of the structure intended to decrease its volume once put in the launcher faring;
- Ease of deployment: in order to deploy the proposed structure easily;
- Available volume: free volume for astronauts;
- Volume optimization: Amount of free volume compared to the outside surface of the structure;
- Workability of the folding process: integrity to fold the structure in a stored configuration with an industrial process;
- Constructive simplicity: realize and build the chosen structure with the modern technologies;

5.1 The idea

The idea is based on a hemispherical shape, principally made with different arches built with MadFlex and then covered with a flexible layer in order to fill the spaces between each arch and give the hemispherical shape to the structure. The rigid side of the Madflex will be on the outside of each arch while the flexible side on the inside, otherwise, the folding would not be possible with the rigid side on the inside. Each arch, to avoid the collapse of the structure, will be anchored to a floor that will be made with structural MadFlex beams also covered with flexible material in order to have even a foldable floor. For this concept, the inspiration comes from the classical umbrella mechanism of deployment. The deployment is assured by a similar umbrella mechanism but in this case the internal branches of the "umbrella" are forced upwards through the rotational motion of a threaded column which allows the upward movement of a ring where the previously mentioned branches are connected. Surely in this case the shape is not hemispherical, reaching the desired height not in a comfortable way for the astronauts.

5.1.1 CoRe antenna

This concept was realized by CoRe to build a deployable space antenna. It has a hemispherical shape and with four branches made in MadFlex, which are connected through fabrics to give a continuous surface to the structure. The multi-layers fabric works as a membrane, capable consequently to withstand only axial forces and not the bending moment or transversal shear. The MedFlex orientation along the thickness of the branches allows them to bend inwards. They are held in the deployed position through a cable mechanism that unites each branch to a ring able to move along a rod placed at the top of the antenna. The following figure shows a prototype of it.

Figure 5.1: Space antenna prototype (Image Credit: CoRe).

Even if this design is thought for an antenna, the same idea can be used to design a deployable dome for a Martian base by placing the antenna as in the previous figure. This concept was particularly inspirational due to its way to take advantage of the MadFlex behavior. The cable mechanism can also be substituted with a less bulky one. This habit can be deployed in different phases as reported below.

This concept is easy to deploy on the surface and to fold and store in a rocket fairing. The free volume is high also thanks to the possibility to have a flat roof, in order to optimize the volume. The structure is very easy to build and this prototype is an example.

The structure, to deploy, will take advantage of the 1 atm internal pressure. This is possible thanks to the low atmospheric pressure on Mars, with an average of 700 Pa. With this great difference between the internal and external pressure, the deployment will be easy. The 1 atm internal pressure is also a requirement for the astronauts and their comfort. It keeps the habitat in the right position and

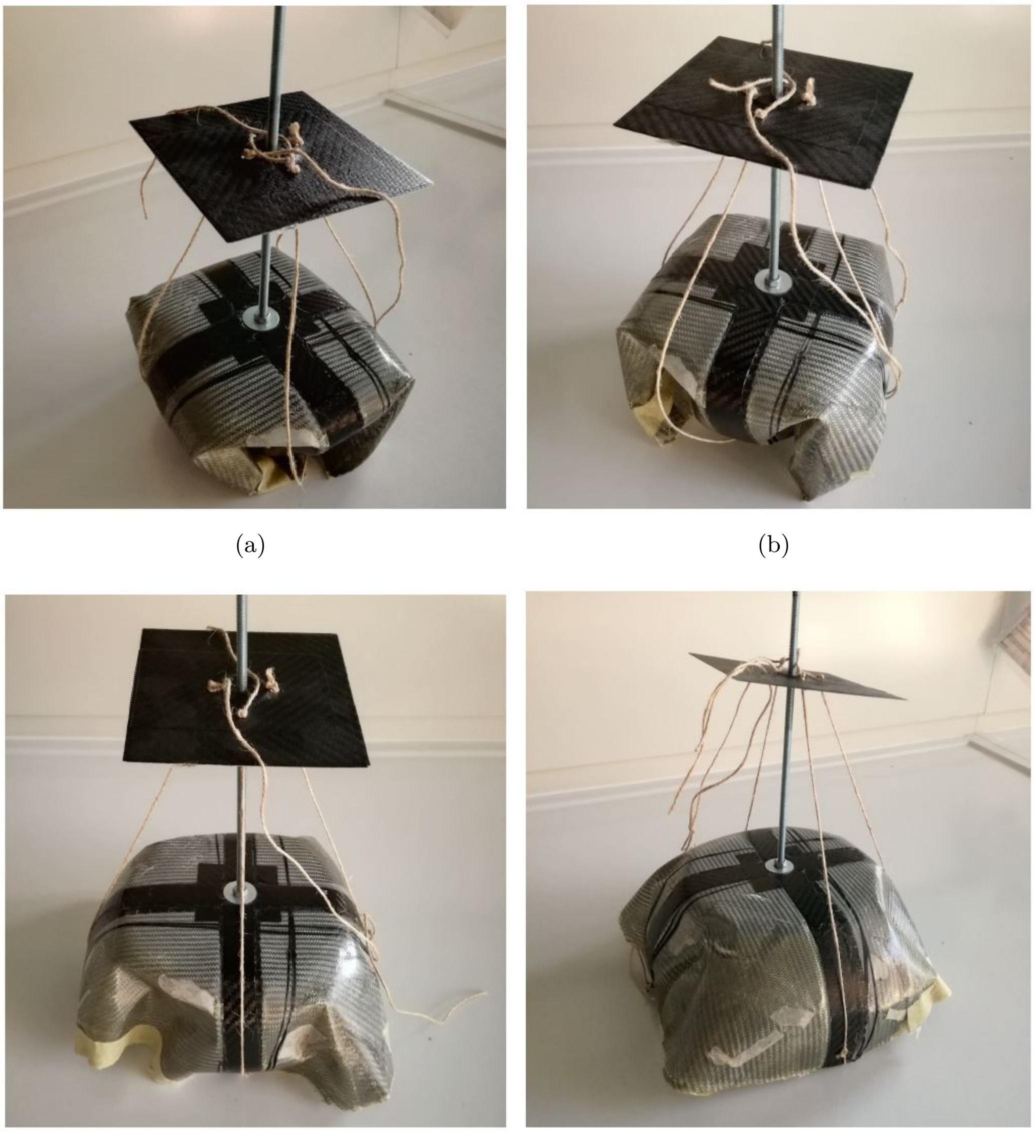

(a) (b) (c) (d)

Figure 5.2: (a) Phase 1 (b) Phase 2 (c) Phase 3 (d) Phase 4

shape and helps the structure to resist the regolith load above the structure. The regolith is fundamental to shield the habitat from cosmic rays and solar storms. A clarification about the role of the pressure to "withstand" the regolith will be done by structural analysis. The intention is to design a cluster of habitat with a hemispherical shape or similar connected to each other by cylindrical structures made with MadFlex. This will lead to the use of different shapes based on the utilization of the volume and its function.

5.2 Keep the habitat folded and docking mechanism

The problem is not only to have the habitat in the folded configuration, which is favorable during the transportation phase of the mission but also to allow its deployment once reached Mars surface. The solutions thought are two:

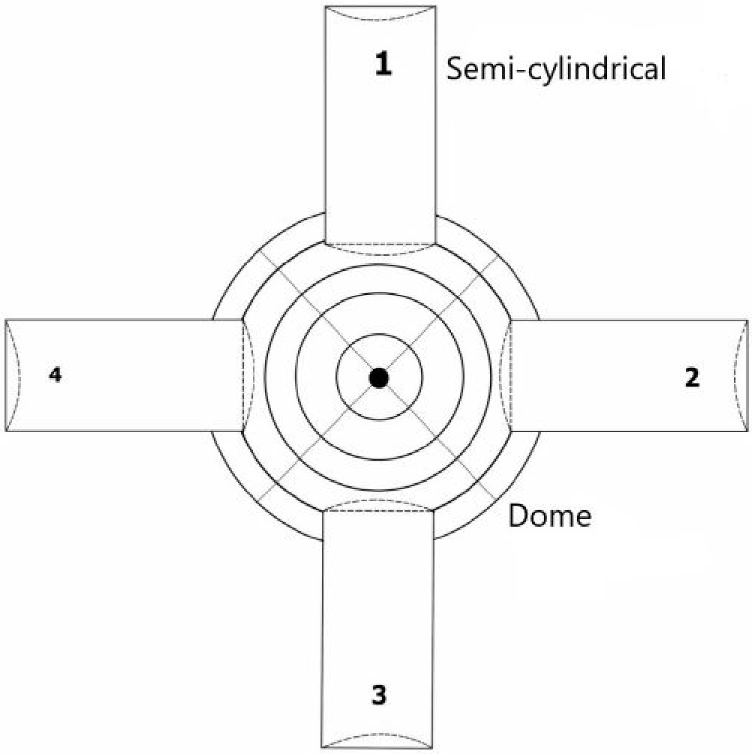

Figure 5.3: Dome structure with semi-cylindrical tubes for connection (from above).

- Keep the habitat folded with belts, with an unhook mechanism, to allow the opening. This mechanism can involve the use of a small pyrotechnic mechanism or it can be realized through another type of option that does not need a big mass or any source of external power. Another idea could be the use of piezoelectric materials.
- Dome's arms can be kept in bent configuration through electromagnets connecting the end of them with the habitat's top, but this needs an external source of power for force generation increasing the total mass.

Numerous are the issues during this phase, such as the perfect alignment of the two modulus along the desired direction, the union without rise of damages and the perfect sealing of the contact surfaces avoiding de-pressurization phenomena. A solution is presented in the following **Fig. 5.4** and **Fig. 5.5**:

Since the deployment is the main behavior of the structure, the presence of rigid docking mechanism or hatches at the ends, as on the ISS, is not allowed because it limits the folding of the structure. Therefore a different solution is necessary. The docking system thought is composed of two mechanisms. The first is placed at the contour of the semi-cylindrical arm and on the contour of the rigid material, made with MadFlex, of the dome, while the second around the area where the hatches should be.

First mechanism: It consists of two parts: an inflatable membrane placed on the contour

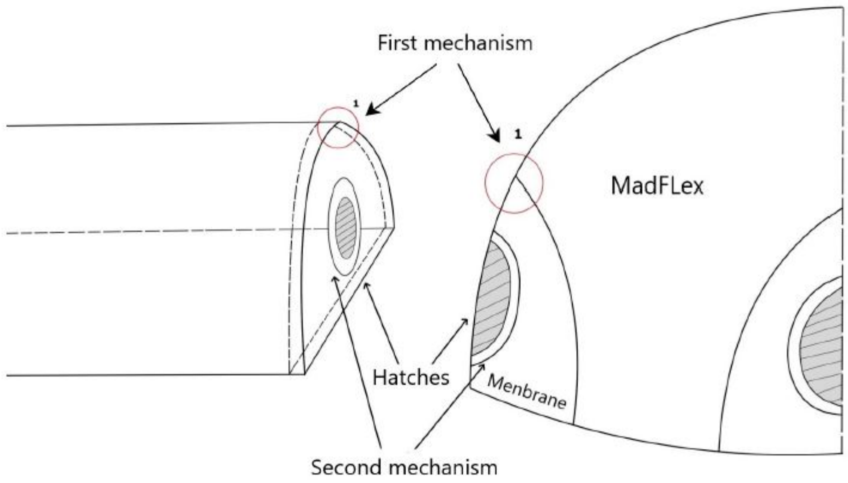

Figure 5.4: Alignment of the habitat (Image Credit: Federico Cumino).

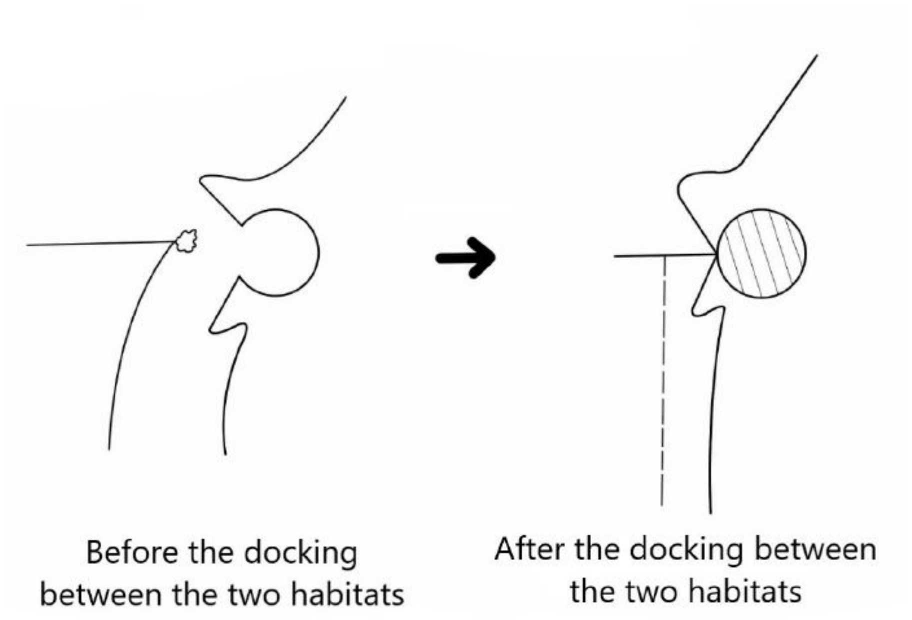

Figure 5.5: First docking mechanism (Image Credit: Federico Cumino).

of the semi-cylindrical arm, as shown on the left in figure, and an inlet placed on the contour of the rigid part of the dome, shown on the right. When aligned the semi-cylindrical arm will be translated horizontally till its contour and inflatable membranes are inside the inlet of the dome. The membrane will be inflated with air if the connection would be temporary, or with expandable foam if permanent, allowing the sealed connection between them.

Second mechanism: As the previous one it consists of two parts too. The mechanism is similar but in this case, the inflatable membranes and the inlet are located on the contour of the hatch zone.

Chapter 6

Structural preliminary analysis

This chapter reviews and explains how the preliminary structural analysis was made. The Chapter explains the method applied to solve the Three- Hinged, Two-Hinged Arch and the complete structure with examined load conditions before with a simplified method by Matlab® script and then compared with FEM analysis in order to validate the results.

6.1 The analyzed structure

The analyzed structure for the Martian base are arches and the floor built by MadFlex. A circular arch with a depth of 0.5 m is initially analyzed to understand better the different behavior of the MadFlex, also a simplified model of a cantilever beam is took into account for the validation. The arch represents the section of the half-cylindrical module, while for the dome it is the shape assumed by the structural branches with a width corresponding to the depth of the section. **Fig. 6.1** shows the standard half-cylindrical section.

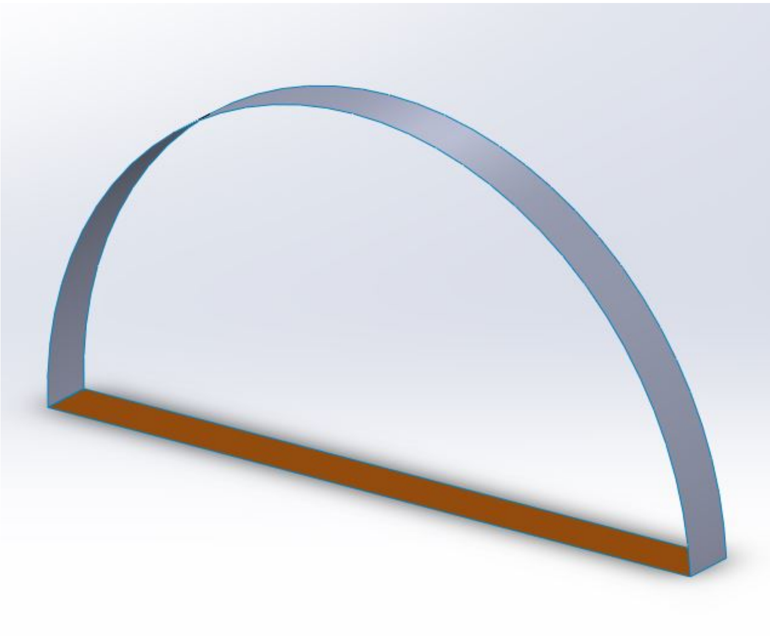

Figure 6.1: Arch structure.

The arch mentioned above can be realized in many ways such as Hingeless Arch, Two-Hinged Arch, or a Three-Hinged Arch. These different configurations give different displacements, deformation and internal stresses. Furthermore, also the solution process is different if they are solved analytically. The analyzed configurations are the following:

- Three-Hinged Arch. It is a statically determinate structure (isostatic). For this reason, it is the simplest shape to solve analytically.

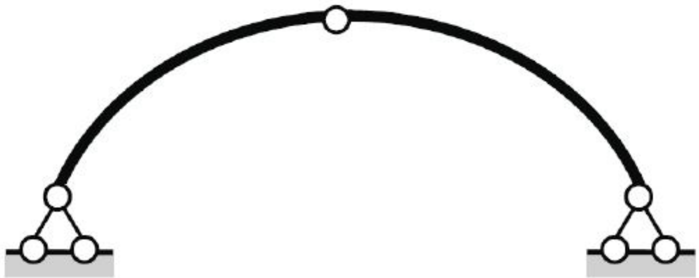

Figure 6.2: Three-Hinged Arch (Image Credit: Theory of Arched Structures).

- Two-Hinged Arch. It is a statically indeterminate structure. For this reason, it needs a more complicated analytical resolution.

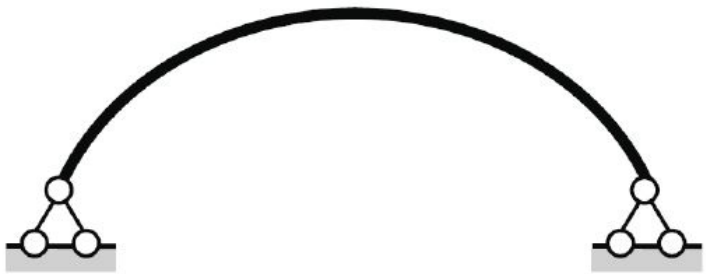

Figure 6.3: Two-Hinged Arch (Image Credit: Theory of Arched Structures).

Arches with four or more hinges are not considered because of statically underdetermination.

6.2 Load conditions

The analyzed load conditions are:

1. Only an internal pressure of 1 atm;
2. Internal pressure of 1 atm and regolith cover load. It is the nominal operative load that the structure must resist during its whole operative life;
3. Regolith load only. It is the most critical load condition, it can happen due to the lack of internal pressure, producing high displacements of the habitat top;

4. Load used to keep the habitat in the folding configuration. This load condition presents the greatest constraint about the curvature of the habitat in the folded configuration. The highest stresses in the foam are expected under this load.

6.3 Structural theory

The Allen's beam theory is used in the analytical analysis considering the MadFlex is a composite material panel having a sandwich-like structure. This theory is also useful because does not neglect the shear contribution in the displacement calculation. The theory considers that:

- The overall shear deformation is absorbed by the core of the sandwich, therefore the equivalent shear stiffness is:

$$GA^* = G\frac{d^2b}{h_c} \tag{6.1}$$

Here is reported the scheme

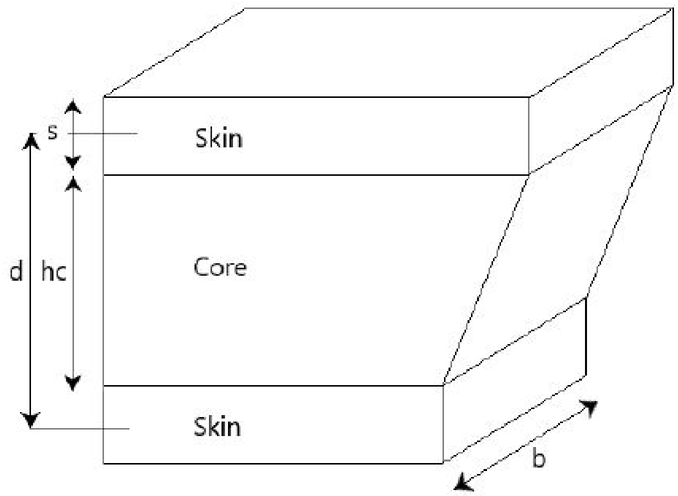

Figure 6.4: Sandwich scheme.

- All the layers of the sandwich are considered in the overall flexural stiffness, which is calculated as the one in the Eulero-Bernulli beam theory:

$$EI = 2E_f(\frac{bs^3}{12} + bs\frac{d^2}{2}) + E_c\frac{bh_c^3}{12} \tag{6.2}$$

This equation is valid when the materials of the two skin are the same, but when they are different, a recalculation is needed considering also the position of the centroid, which will be explained later [30]. Once the habitat is deployed on the Martian surface and the regolith shield located above it, the module is buried under (1.650 m) of regolith, as required for the protection against ionizing radiation. Regolith load over the habitat is a distributed, but non-uniform load, because how it can be seen in **Fig. 6.5**, around the circular habitat there is another circular structure that represents the regolith and the effective load of the regolith is not a radial pressure. For this reason, a discretization of it is needed for the carrying out of the analytical structural analysis. The distributed load is converted into more concentrated loads equal to the regolith volume between two discretization points multiplied by the Martian regolith density and the Martian constant of gravity. The result is a concentrated load, placed in the middle of the distance between the discretization points. The arrows in the **Fig. 6.5** represent the forces.

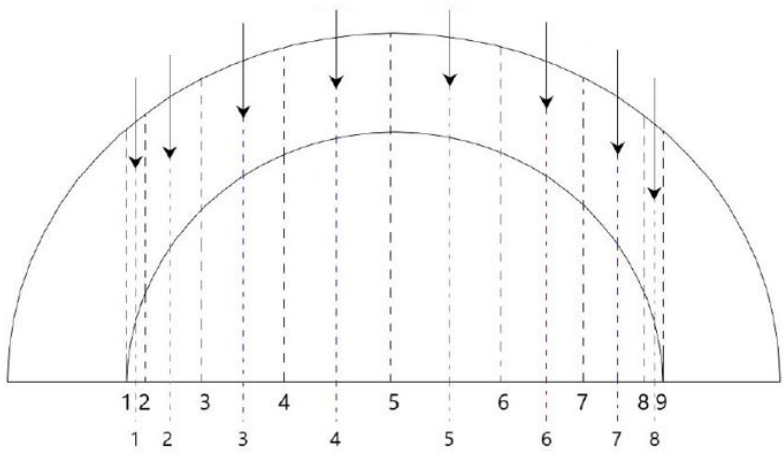

Figure 6.5: Load discretization scheme.

Now are reported the analytical method used to resolve the three-hinged arch and the two-hinged arch exposed by Igor A. Karnovsky in the book Theory of Arched Structures [38]

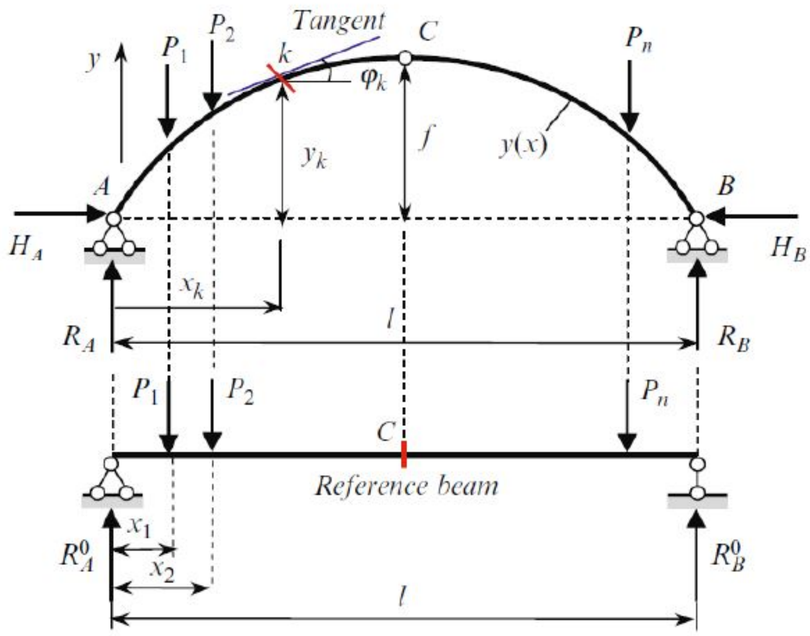

Figure 6.6: Three-Hinged Arch force scheme (Image Credit: Theory of Arched Structures).

In arch structures, the horizontals reactions (H_a and H_b) are equal in magnitude but opposite in direction while the vertical reactions of three-hinged have the same values as the reactions of the reference beam, reported in **Fig. 6.6**, and can be obtained with a simple equilibrium equation of the moment in the points A or B. The horizontal reactions are calculated with the equilibrium of the flexural moment at the central hinge and imposed that is equal to zero.

$$M_c = \underbrace{R_A \frac{l}{2} - P_1(\frac{l}{2} - x_1) - P_2(\frac{l}{2} - x_2)}_{\mathrm{M}_0^c} - H_A \cdot f = 0 \tag{6.3}$$

Therefore

$$H = \frac{M_0^c}{f} \tag{6.4}$$

To calculate the internal forces, the convention shown in **Fig. 6.7** is considered, and the Bending Moment M_k, Shear Q_k, and axial forces N_k at each section k can be acquired with the equilibrium of free body diagram of the left or right part of the arch (referring to the central hinge). Considering the left part:

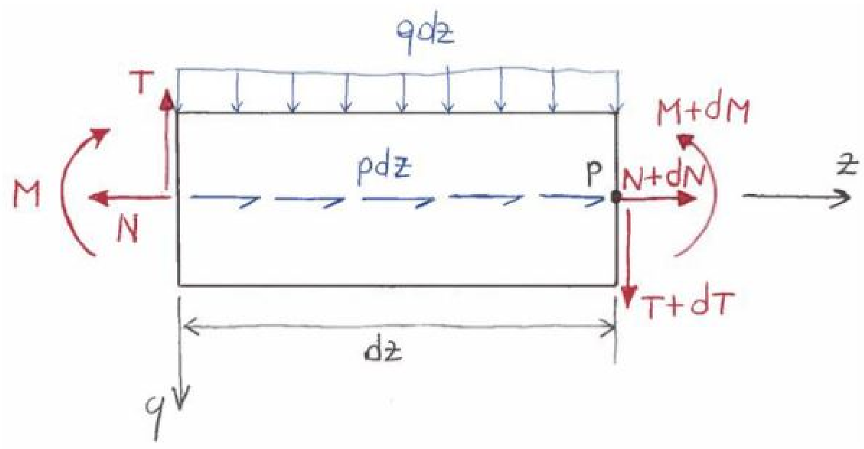

Figure 6.7: Rectilinear elementary beam segment convention (Image Credit: Aerospace Structure lecture).

$$M_k = R_A x_k - \sum_{left} P_i(x_k - x_i) - H y_k \tag{6.5}$$

$$M_k = \left(R_A - \sum_{left} P \right) cos\varphi_k - H sin\varphi_k \tag{6.6}$$

$$M_k = -\left(R_A - \sum_{left} P \right) sin\varphi_k - H cos\varphi_k \tag{6.7}$$

Where φ_k is the angle between the tangent to the arch centerline at the section k and the horizontal line. From the book "Theory of Arched Structures": " In order to calculate the bending moment in any cross-section of the three-hinged arch, the bending moment at the same section of the reference beam should be decreased by the value Hy_k. Therefore, the bending moment in the arch less than that of in the reference beam. This is the reason why the three-hinged arch is more economical than simply supported beam, especially for large-span structures." [38]

For the material model it is important to remember the different behaviors of the materials that compose the MadFlex, especially the Dyneema. Due to these different mechanical properties in traction and compression, eight different values of flexural stiffness are considered (four when carbon is on the upside of the sandwich and four when the Dyneema is on the upside).

Work case	Upper skin	Lower skin
Case 1	Carbon in traction	Dyneema in traction
Case 2	Carbon in compression	Dyneema in traction
Case 3	Carbon in traction	Dyneema in compression
Case 4	Carbon in compression	Dyneema in compression
Case 5	Dyneema in traction	Carbon in traction
Case 6	Dyneema in traction	Carbon in compression
Case 7	Dyneema in compression	Carbon in traction
Case 8	Dyneema in compression	Carbon in compression

Table 6.1: MadFlex cases

These eight different cases generate eight different membrane and bending stiffness. The stiffness matrixes are calculated with the plate theory showed below. Considering the following picture the coordinates L and T represent the longitudinal and transversal direction along the fibers and belonging to the reference system, named "p".

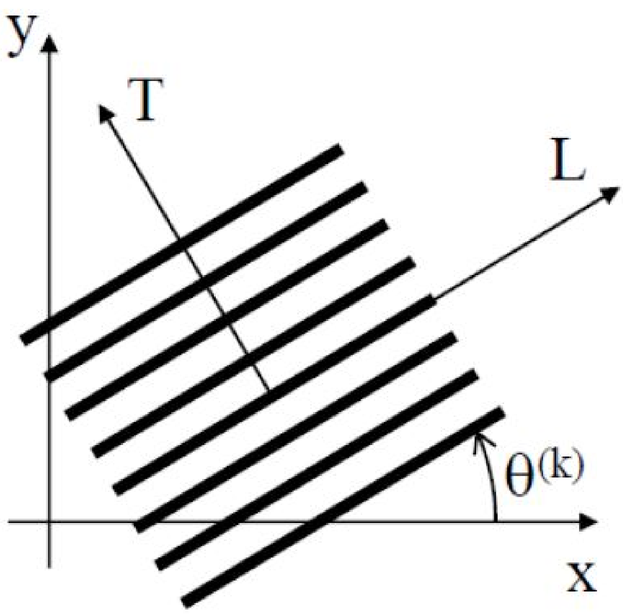

Figure 6.8: Orthotropic reference system and global reference system (Image Credit: Aerospace Structure lecture).

the reduced stiffness matrix for a single layer of an orthotropic material is obtained by:

$$\left[Q_p^{(k)}\right] = \begin{bmatrix} \frac{E_L}{1-\nu_{LT}\cdot\nu_{TL}} & \frac{\nu_{TL}E_T}{1-\nu_{LT}\cdot\nu_{TL}} & 0 \\ \frac{\nu_{LT}E_T}{1-\nu_{LT}\cdot\nu_{TL}} & \frac{E_T}{1-\nu_{LT}\cdot\nu_{TL}} & 0 \\ 0 & 0 & G \end{bmatrix} \tag{6.8}$$

If the reference system p is rotated of an angle ϑ concerning the global reference system, the directional cosines matrix $[\Lambda(k)]$ is needed.

$$\left[\Lambda^{(k)}\right] = \begin{bmatrix} cos^2(\vartheta^{(k)}) & sin^2(\vartheta^{(k)}) & cos(\vartheta^{(k)})\cdot sin(\vartheta^{(k)}) \\ sin^2(\vartheta^{(k)}) & cos^2(\vartheta^{(k)}) & 2cos(\vartheta^{(k)})\cdot sin(\vartheta^{(k)}) \\ -cos(\vartheta^{(k)})\cdot sin(\vartheta^{(k)}) & cos(\vartheta^{(k)})\cdot sin(\vartheta^{(k)}) & cos^2(\vartheta^{(k)}) - sin^2(\vartheta^{(k)}) \end{bmatrix} \tag{6.9}$$

The reduced stiffness matrix in a rotated coordinate system is then:

$$\left[Q^k\right] = \left[\Lambda^{(k)}\right]^{-1} \cdot [Q_p] \cdot \left(\left[\Lambda^{(k)}\right]^{-1}\right)^T \tag{6.10}$$

And consequently, for the plate considered, is possible to calculate the membrane stiffness matrix $[A]$, the coupling matrix $[B]$ and bending stiffness matrix $[D]$:

$$[A] = \int_{-\frac{h}{2}}^{+\frac{h}{2}} [Q]\,dz = \sum_{k=1}^{NS} \left[Q^{(k)}\right] \int_{z^{k-}}^{z^{k+}} dz = \sum_{k=1}^{NS} \left[Q^{(k)}\right](z^{k+} - z^{k-}) = \sum_{k=1}^{NS} h^{(k)} \left[Q^{(k)}\right] \tag{6.11}$$

$$[B] = \int_{-\frac{h}{2}}^{+\frac{h}{2}} z\,[Q]\,dz = \sum_{k=1}^{NS} \left[Q^{(k)}\right] \int_{z^{k-}}^{z^{k+}} z\ dz = \sum_{k=1}^{NS} \left[Q^{(k)}\right] \left(\frac{(z^{k+})^2}{2} - \frac{(z^{k-})^2}{2}\right) \tag{6.12}$$

$$[D] = \int_{-\frac{h}{2}}^{+\frac{h}{2}} z^2\,[Q]\,dz = \sum_{k=1}^{NS} \left[Q^{(k)}\right] \int_{z^{k-}}^{z^{k+}} z^2\ dz = \sum_{k=1}^{NS} \left[Q^{(k)}\right] \left(\frac{(z^{k+})^3}{3} - \frac{(z^{k-})^3}{3}\right) \tag{6.13}$$

where z^{k+} and z^{k-} are the coordinates along the thickness of each layer referred to the coordinate system in the middle of the overall plate. NS represents is the total number of layers in the laminate.

Since the theory used for the analysis is the one referred at the beam, only the element (1,1) of the matrices $[A]$, $[B]$ and $[D]$ are taken into account for the simplified calculations. Even if the bending stiffness D(1,1) is different from the one used in the theory of the beam because the value relative to $Q_p^{(k)}$(1,1) is only equal to E_L and not to $\frac{E_L}{1-\nu_{LT}\nu_{TL}}$, the difference is negligible.

Nevertheless, a B(1,1) value equal to zero is useful to facilitate the analytical solution about displacement, which employs the Virtual Working Principle, also called Force Method in the book "Theory of Arched Structures" [38]. B(1,1)=0 permits the decoupling of the membrane phenomena from the bending ones. So it is necessary to translate the material reference system from the middle of the laminate to the centroid. The centroid is the intersection point of material neutral axes. Points on these

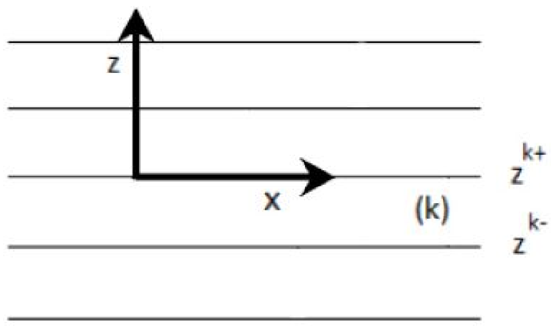

Figure 6.9: Coordinate system placed in the middle of the laminate (Image Credit: Aerospace Structure lecture).

axes have only membrane strain (ϵ^0) and the absence of the curvature (k) participation to the overall strain (ϵ). To withdraw a repetitive notation, the term (1,1) of the previous matrix will be symbolized with the subscript 1. The centroid is found from the constitutive equations of the beam:

$$\begin{bmatrix} \{N\} \\ \{M\} \end{bmatrix} = \begin{bmatrix} A_1 & B_1 \\ B_1 & D_1 \end{bmatrix} \begin{bmatrix} \{\epsilon_0\} \\ \{k\} \end{bmatrix} \tag{6.14}$$

and by imposing that the curvature k is equal to zero, the z coordinate of the centroid is:

$$z = \frac{B_1}{A_1} \tag{6.15}$$

Now the membrane and bending stiffness referred to the centroid position can be calculated repeating the process above giving attention to consider the position of the material layer concerning it. This process allows the decoupling of the membrane effects from the bending ones and therefore the simplification of the equation used in the Virtual Working Principle. Is then possible to calculate the internal strain and stress by inverting the constitutive equations above reported:

$$\begin{bmatrix} \{\epsilon_0\} \\ \{k\} \end{bmatrix} = \frac{1}{A_1 D_1 - B_1^2} \begin{bmatrix} D_1 & -B_1 \\ -B_1 & A_1 \end{bmatrix} \begin{bmatrix} \{N\} \\ \{M\} \end{bmatrix} \tag{6.16}$$

The overall strain is:

$$\{\epsilon\} = \{\epsilon_0\} + z\{k\} \tag{6.17}$$

and consequently the stresses:

$$\{\sigma\} = [Q]\,\{\epsilon\} \tag{6.18}$$

Nevertheless, the previously explained method gives a perfect result for standard material but fails with the MadFlex. Due to the behavior of the MadFlex that changes according to the load condition;

hence, the stiffness matrices are not constant, but they are affected by the load. This material adds a new relation that links the material properties to the load condition making the system underdetermined. It is necessary an iterative process.

6.4 Desplacement calculations

Virtual Working Principle, also called "Force method" in the book "Theory of Arched Structures" is used for the estimation of the structure displacement in the case of three-hinged and two-hinged arches.

"The Virtual Work principle establishes the equivalence between external virtual work L_v^e and internal virtual work L_v^i for a structure subject to two independent systems: the (a) balanced system (external forces and internal tensions) and the congruent system (b) (displacements and strain)" [39].

$$L_v^e = L_v^i \tag{6.19}$$

The internal virtual work for a deformable structure is:

$$L_v^i = \int_V \{\sigma^{(a)}\}\{\epsilon^{(b)}\} dV \tag{6.20}$$

Introducing the De Saint Venant beam, the participation of bending moment, transversal shear and axial force to the internal virtual work for a flat beam in the plane x,z can be written as follows:

$$L_v^i = \int_L \left(\frac{N^{(a)}N^{(b)}}{EA} + \frac{M^{(a)}M^{(b)}}{EI} + \frac{T^{(a)}T^{(b)}}{KGA} \right) dx \tag{6.21}$$

with EA as the membrane stiffness of the beam, EI as the bending stiffness, GA as the shear stiffness ad K as the shear correction factor. The external virtual work, on the other hand, can be expressed as:

$$L_v^e = \int_V \{f^{(a)}\}^T \{\eta^{(b)}\} dV + \int_V \{M^{(a)}\}^T \{\varphi^{(b)}\} dV \tag{6.22}$$

with f as the external force, η the displacement induced by it, M the external moment and φ the rotation induced by it. The congruent system (b), mentioned above, can set as the real system (r), while the balance system (a) as the "primary system" (u) (as reported in the book "Theory of Arched Structures") for the displacement calculation. Only one force with a value equal to one ($f^{(a)} = 1$) is presented in the primary system (u). This gives:

$$|\{\eta\}| = \int_L \left(\frac{N^{(u)}N^{(r)}}{EA} + \frac{M^{(u)}M^{(r)}}{EI} + \frac{T^{(u)}T^{(r)}}{KGA} \right) dx \tag{6.23}$$

$$|\{\varphi\}| = \int_L \left(\frac{N^{(u)}N^{(r)}}{EA} + \frac{M^{(u)}M^{(r)}}{EI} + \frac{T^{(u)}T^{(r)}}{KGA} \right) dx \tag{6.24}$$

These equations are also adequate for beams where material properties and section change along with it (but for limited variations). Material properties (E and G) and the ones related to the section (area, the moment of inertia and the shear corrective factor) are within the integral in the previous expressions [39].

The primary system is set with vertical forces equal to one and placed at different times in the discretization points chosen as the exploratory force for the primary system. This allows us to know the vertical displacement of each discretization point. This information is necessary to understand the residual habitat height when a de-pressurization occurs. **Fig. 6.10** shows the position of the exploratory forces.

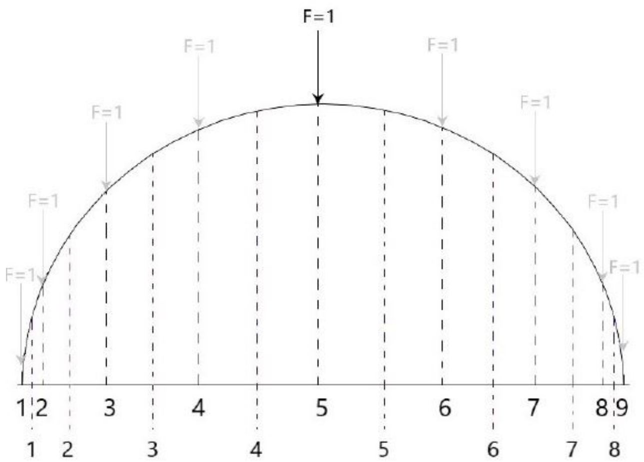

Figure 6.10: Exploratory force for the 9 primary system. (Image Credit: Federico Cumino).

To solve the two-hinged arch, which is an indeterminate structure, the Virtuale Working Principle also can be used. In this configuration, the constrain reaction cannot be found with the three equilibrium equations, because their number is equal to four. The system provides infinite solutions, but just one makes the system balanced and congruent. The missing equation can be written using the Virtual Working Principle. The first step is to choose a constrain reaction as "Primary unknowns" (X) and substitute it with an active force, achieving an equivalent statically determinate structure. This last system is equivalent to the statically indeterminate one, only if the displacement produced by the active force is equal to zero [39]. The value X of the Primary unknown can be determined by using the Virtual Working Principle in the following manner. At first, it is required to know which system is the real system (r) and which is the primary one (u).

The real system (r) is the one with all the applied load. It is convenient to use the real system in the equivalent statically determinate structure. By the principle of superposition, it is feasible to write it as the sum of two systems, called (0) and (1). A reasonable choice about systems (0) and (1) to solve the Two Hinged Arch is reported in figure **Fig. 6.11**, where the system (0) is the Three-Hinged Arch previously solved and the system (1) is the structure where only the primary unknown is applied. Therefore:

$$\begin{cases} H_a^{(r)} = H_a^{(0)} + X \cdot H_a^{(1)} \\ \dots \\ M_a^{(r)} = M_a^{(0)} + X \cdot M_a^{(1)} \\ \dots \end{cases} \tag{6.25}$$

The primary system (u) must have the same constrain reaction of (r) and an exploratory force

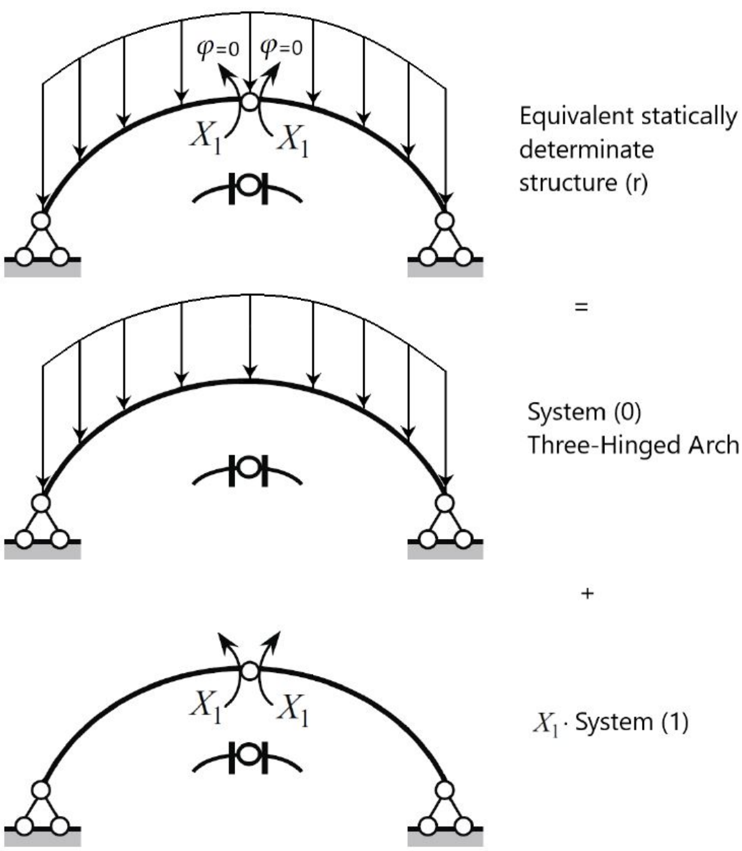

Figure 6.11: Decomposition of the real system (equivalent statically determinate structure) in the system (0) and (1).

on the same point where the displacement is needed to be find. Consequently, the system (u) corresponds to the system (1). Imposing that the rotation at the upper hinge is zero in the (6.24), the primary unknown X calculated:

$$X = -\frac{\int_L \left(\frac{N^{(0)}N^{(1)}}{EA} + \frac{M^{(0)}M^{(1)}}{EI} + \frac{T^{(0)}T^{(1)}}{KGA} \right) dx}{\int_L \left(\frac{N^{(1)}N^{(1)}}{EA} + \frac{M^{(1)}M^{(1)}}{EI} + \frac{T^{(1)}T^{(1)}}{KGA} \right) dx} \tag{6.26}$$

In conclusion, the constrain reactions and the internal forces of the Two- Hinged Arch are obtained by the relations (6.25).

From the theory reported above, a script in MATLAB is written in order to resolve the case of the two-hinged arch. This script is essential to have a first result that will be compared with a model created using the finite element theory. After the convalidation of the finite element model, it will be used to study a more complex structure that will require high computational cost by using the virtual working principle.

6.5 Virtual working principle results

By the use of the virtual working principle a two-hinged arch is analyzed. The radius of the arch is 3500 *mm* and is 500 *mm* wide. The type of structure is a sandwich material. The type of material considered for this structure are a carbon fiber laminate for the upper face, a Rohacell 110 WF for the core and a Dyneema laminate for the lower face. The carbon fiber laminate is made of four carbon fiber fabrics layers of 0.28 *mm* each one and oriented [0°/0°/0°/0°]. The core is 80 *mm* thick made with isotropic foam. The Dyneema laminate is made of four unidirectional Dyneema of 0.12 *mm* each one and oriented [0°/90°/90°/0°]. These materials properties and thickness are also based on common values in commerce. Here are reported the material properties

Material	$\mathbf{E}_1$ **(MPa)**	$\mathbf{E}_2$ **(MPa)**	$\mathbf{G}_{12}$ **(MPa)**	ν_{12}	ρ **(kg/m^3)**	σ_U **(traction) (MPa)**	σ_U **(compression) (MPa)**
Carbon fiber fabrics	70000	70000	5000	0.1	1790	600	570
Rohacell 110 WF	180	180	70	0.2	110	3.7	3.6
Unidirectional Dyneema	100000	100	200	0.01	980	3300	-

Table 6.2: Material properties.

On this arch is considered a layer of Martian regolith. The layer is thick 1650 *mm* with a density of 1400 kg/m^3. To calculate the force generated by this layer on the structure, the scheme reported in **Fig. 6.5** is considered. So the regolith volume is divided into different blocks, then the area of each block is calculated and multiplicated by the width of the arch in order to obtain the volume of each block. The volume is multiplicated by the density and Mars gravity acceleration so the force of each volume can be obtained. The script in MATLAB is useful to find the displacement of the top of the arch. The result is reported in **Fig. 6.12**

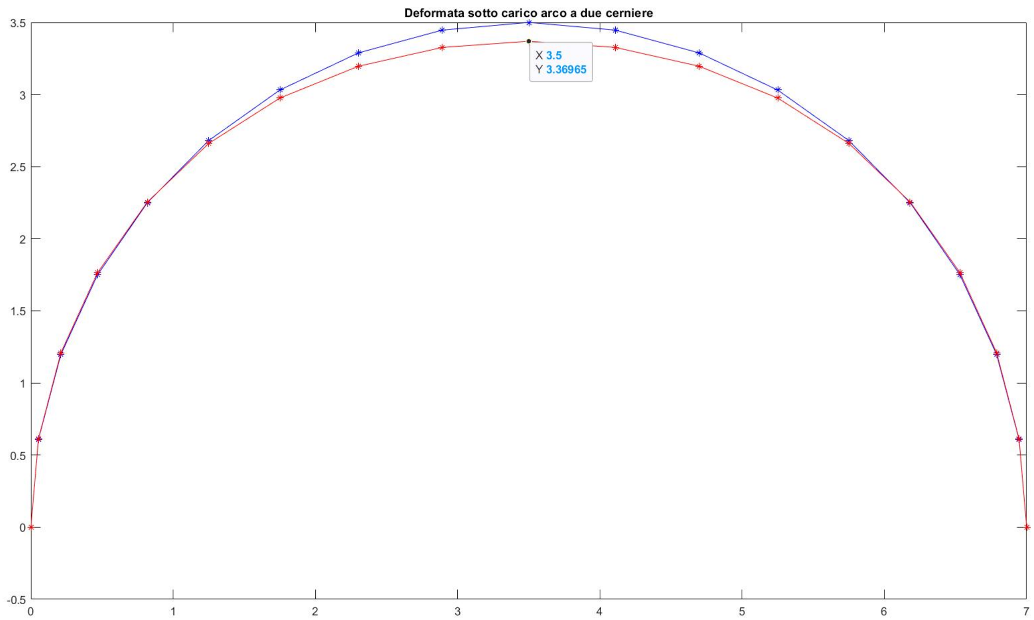

Figure 6.12: Two-hinged arch top displacement by vitual working principle.

The script in MATLAB is useful to find the displacement of the top of the arch. The result is reported in. As it can be seen, the top of the arch moves from 3500 *mm* to 3369 *mm*, so a displacement of 131 *mm*.

6.6 Two-hinged arch FEM model

The two-hinged arch is now analyzed by the use of the finite elements method (FEM) by the use of the software Patran/Nastran. The result will be compared with the one from the virtual working principle in order to validate the FEM model and then continue by using this method to analyze a more complex structure composed of many hinged arches. The model has the same geometry used in the previous calculations, for obvious reasons, and the mesh is a hybrid between 2D and 3D elements. The upper and lower faces are modeled by the use of 2D elements while the core is modeled by the use of 3D elements as shown in **Fig. 6.13**. The structure is divided into 36 elements along the semi-circumference and into 5 elements along the width, and all the elements are of the same dimensions. The core is also divided into three elements along with the thickness. Initially, the mesh was less thin and different divisions of elements were taken into account till the convergence of the results while the increase of mesh refinement.

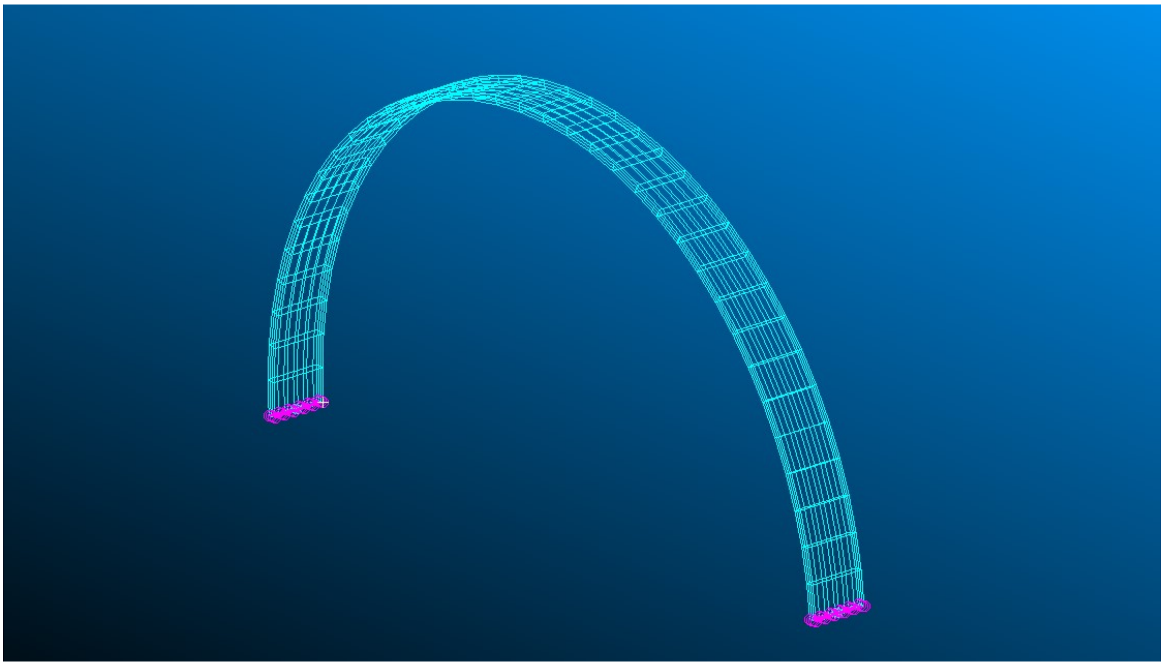

Figure 6.13: Two-hinged arch FEM model.

The hinges at the and of the arch are modeled by the use of rigid elements called RBE2, where the nodes at the extremities are connected to one node where the hinge boundary condition is applied, that let only the rotation about the axis parallel to the width of the arch.

The materials are the same as before and firstly are modeled the 2D orthotropic material, because 2D elements are used for the two faces, such as the carbon fabric and the unidirectional Dyneema and then composite materials are modeled with the same characteristics as before. For the Rohacell foam used for the core, the behavior of isotropic material is used.

The forces, in Newton, are positioned in the same points as in the virtual working principle model wrote in MATLAB. It is important to know that due to the division in five elements along the width of the arch, there will be 6 nodes in which are located forces, so the forces calculated in the MATLAB script are divided by six and used in the FEM model, as shown in **Fig. 6.15**

The problem is analyzed by the use of linear elastic analysis. That because even the script in MATLAB use the linear theory to resolve the problem and in order to have comparable results the same considerations are used in the FEM analysis.

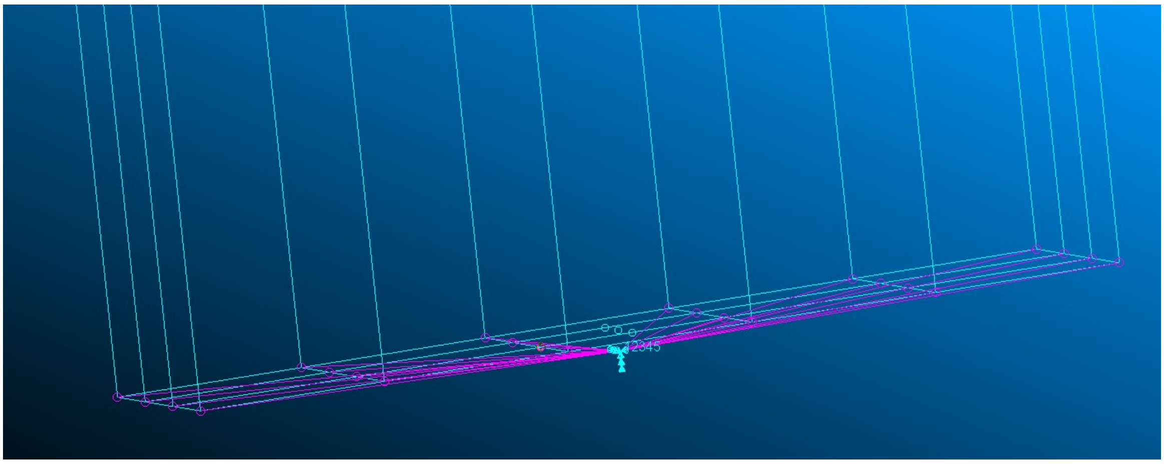

Figure 6.14: Hinge FEM representation.

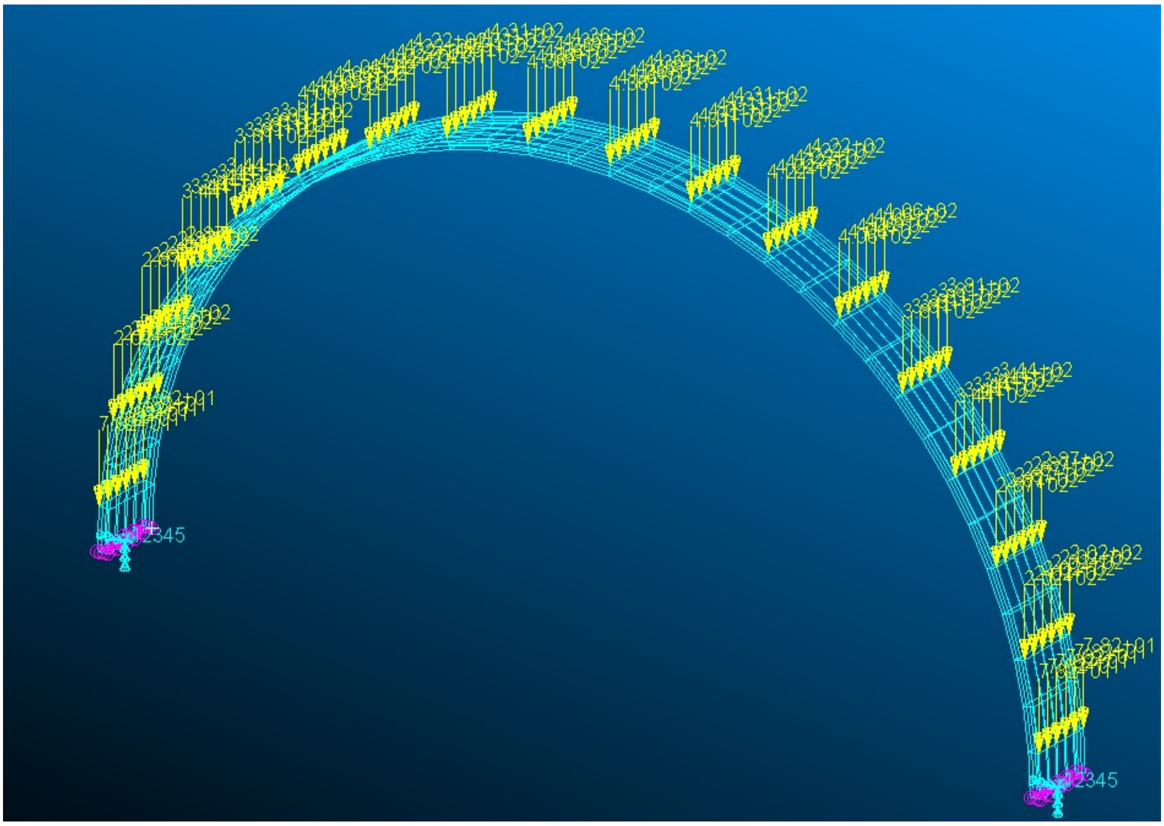

Figure 6.15: Forces FEM representation.

The result of this first analysis is shown in **Fig. 6.16**. As it can be seen the two-hinged arch top displacement is 142 *mm*. The difference between the result from the virtual working principle and FEM model is 11 *mm*, which reasonable because the FEM model is based on a theory more accurate than the theory on which is based the virtual working principle, that is Kirchhoff beam theory. Due to this little difference is notable that the FEM model is accurate and can be used for more complex analysis from here on out.

Once tested the accuracy of the FEM model, the idea is to build a model where the two-hinged arch is actually made of MadFlex. Initially, the problem in the virtual working principle was how to model the MadFlex, which has different behaviors depending on the load case and that means that the

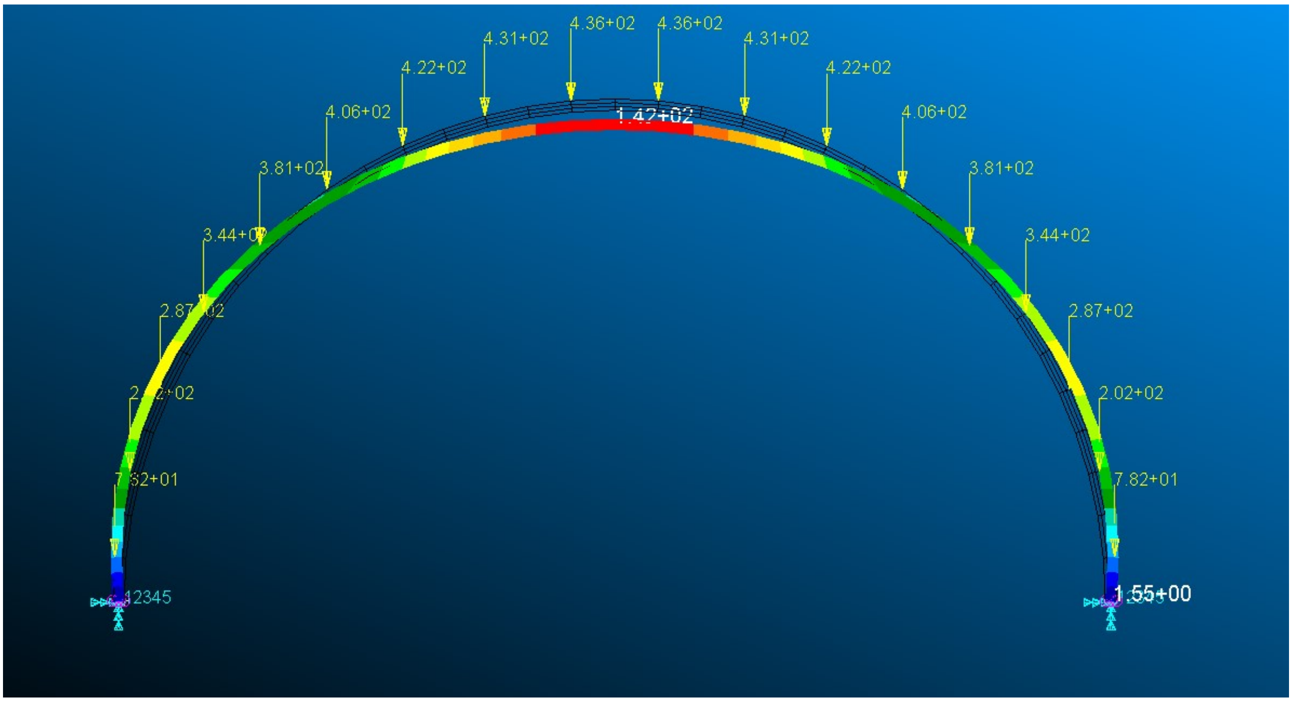

Figure 6.16: FEM model two-hinged arch top displacement

properties in the integral are related to the stress applied to the material. So the difficulty was to model the Dyneema layer, which is highly resistant in traction but no in compression, due to the micro-buckling of the fiber in the material. The idea was to create a non-linear 2D orthotropic material but inside the software Patran that was not possible. So in order to have a material with different behaviors in traction and compression, the best solution was to create a non-linear isotropic material that, with some approximation, could substitute the Dyneema laminate in MadFlex. So in Patran are created two 2D orthotropic materials that represent the unidirectional Dyneema in traction and compression with linear elastic behavior. In **Tab. 6.3** are reported the properties

Material	**E_1 (MPa)**	**E_2 (MPa)**	**G_{12} (MPa)**	ν_{12}	**ρ (kg/m^3)**
Unidirectional Dyneema (traction)	100000	100	200	0.05	980
Unidirectional Dyneema (compression)	10	100	200	0.05	980

Table 6.3: Unidirectional Dyneema properties.

Considering two composite laminate, in the same configuration as reported before, made with these two materials, it is possible thanks to the algorithm in Patran to calculate the equivalent Young modulus and other properties of the laminate, which are shown in **Tab. 6.4**. With these properties, a strain-stress curve is created that shows a bi-modulus behavior, and this curve will be used in Patran in order to have a bi-modulus material.

The strain-stress curve shown in **Fig. 6.17** has the strain on the x-axis and stress in MPa on the y-axis.

Material	E_1 (MPa)	E_2 (MPa)	G_{12} (MPa)	ν_{12}
Equivalent isotropic Dyneema (traction)	50000	50000	200	0.01
Equivalent isotropic Dyneema (compression)	56	56	200	0.01

Table 6.4: Equivalent isotropic Dyneema properties.

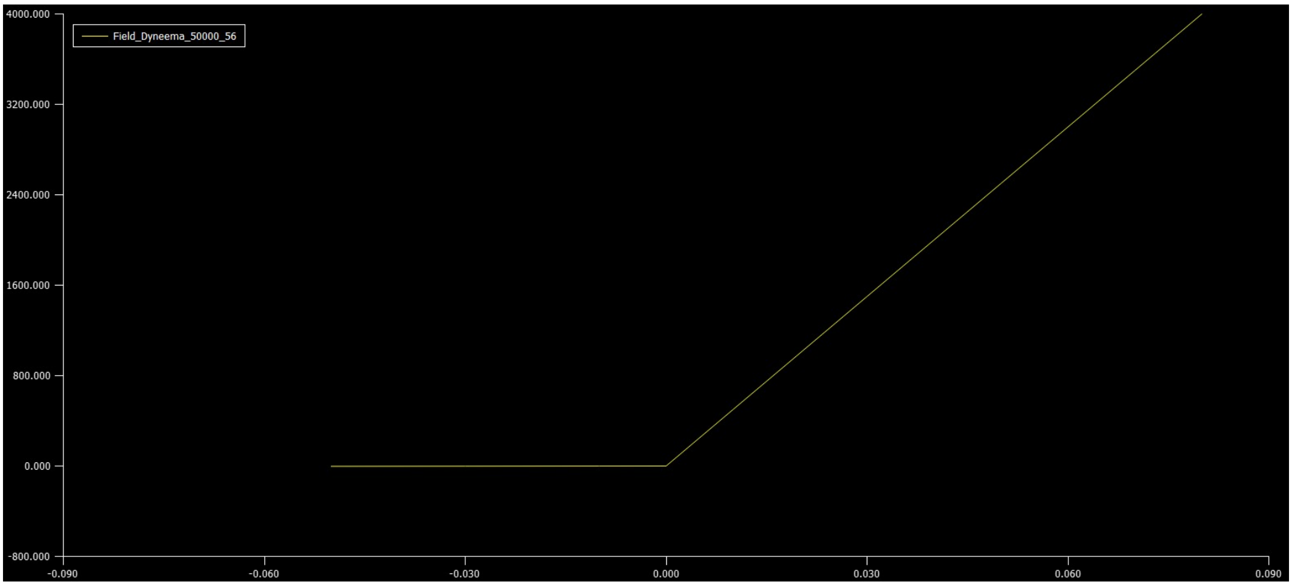

Figure 6.17: Equivalent isotropic Dyneema strain-stress curve.

This material will be used as a substitute for the Dyneema composite laminate. After many analyses, the best thickness for each layer is seen to be 2.8 *mm* for both upper and lower faces and 80 *mm* for the core. The thickness of the two faces must a compromise between flexibility and resistance, to let the folding of the structure.

Then an arch with this material and geometry and the same previous load case is analyzed. The carbon fiber laminate is made of five carbon fiber fabrics of 0.56 *mm* each oriented [0°/0°/0°/0°/0°]. It is important to know that since the material for the lower face is an isotropic non-linear material then a non-linear analysis must be used. Also, the non-linear analysis is useful for large displacement in the structure and the forces follow the displacement. From this analysis is interesting to know how much is the displacement of the top of the arch and the stress inside, in order to know if the stresses are lower than the material's ultimate strength.

From the **Fig. 6.18** is visible that the top of the arch moves 142 *mm* downward. It could be strange that the displacement is the same as the previous analysis, but here the differences are the non-linear material, which is weak in compression, and the higher thickness of both faces. The stresses reported are only the higher stress in each component of the sandwich. The stresses considered are the ones along the x-axis, as in **Fig. 6.19**, of the element of the mesh, which are higher than the stress in the other directions. In the carbon fiber laminate, the highly stressed layer is the upper one, so the outermost.

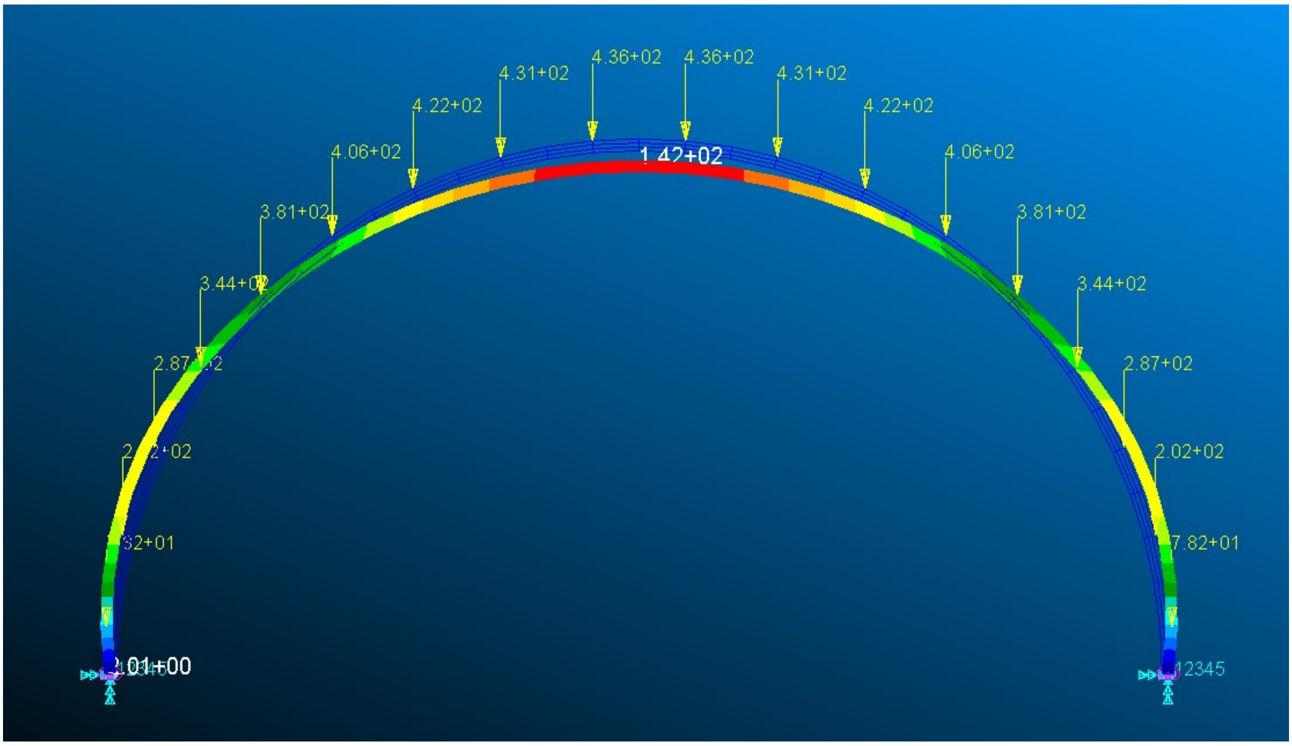

Figure 6.18: FEM model non-linear analysis.

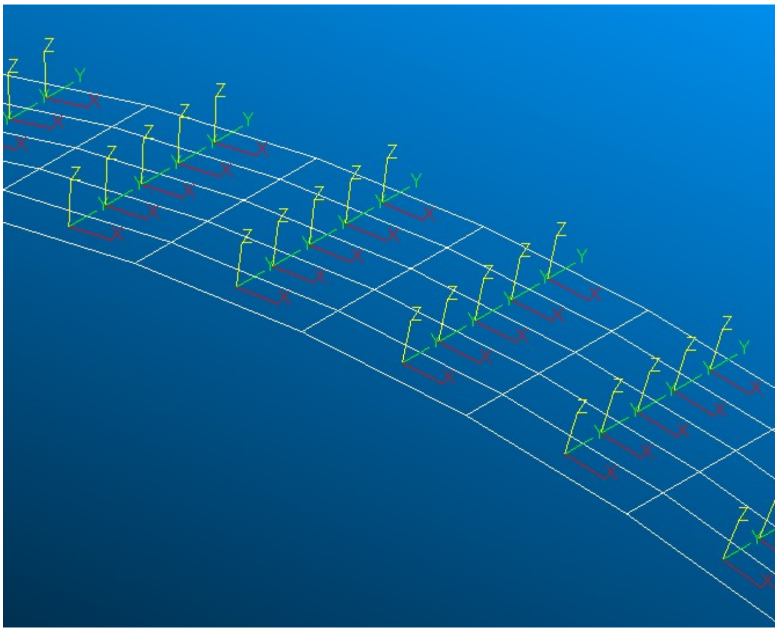

Figure 6.19: Coordinate system on the element.

As it can be seen in **Fig. 6.20**, there is compression on the top of the arch reaching a maximum value of -99.6 *MPa* while gradually moving towards the hinges there is traction reaching a maximum value of 50.3 *MPa*. These are the maximum stresses but in the figure is visible how they change along the arch.

Looking at the stresses in the equivalent Dyneema in **Fig. 6.21**, where the higher stresses are in the inner part of the layer, there is a condiction of traction on the top of the arch with a maximum value of 90 *MPa* while there is compression gradually moving toward to the hinges, with a maximum

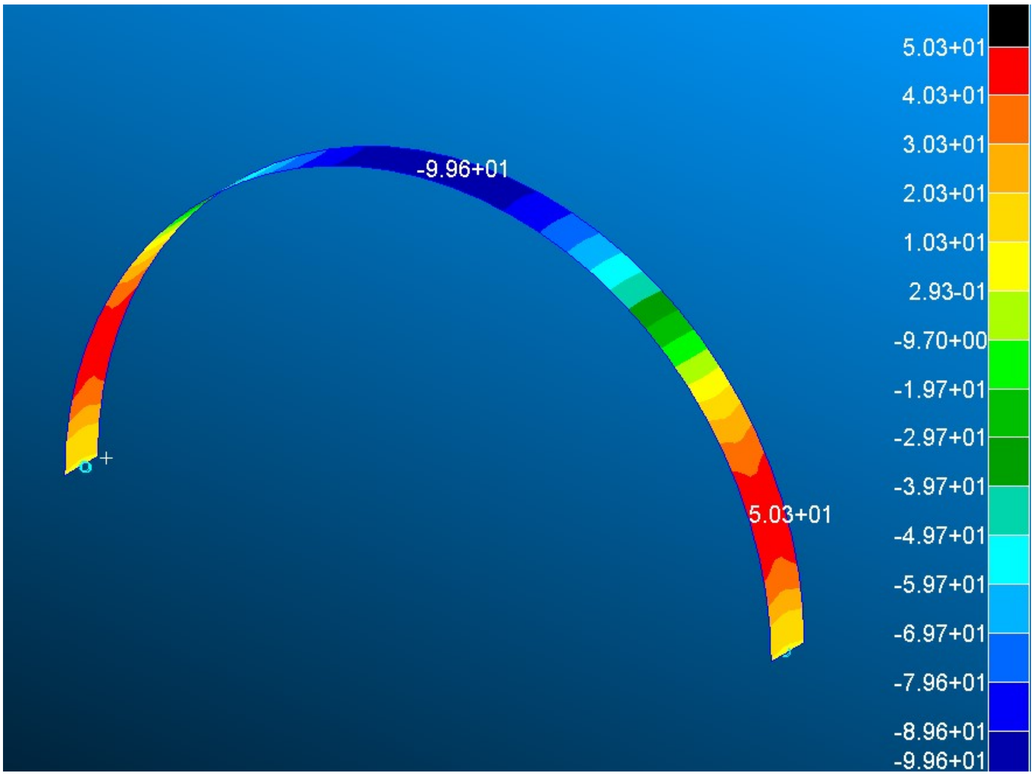

Figure 6.20: Stress in the outermost layer of the carbon laminate.

value of -29 *MPa*. In the condiction of compression, the equivalent Dyneema does not cooperate in the sustaining of the structure. As expected the condiction in the equivalent Dyneema face is specular than in the carbon fiber laminate.

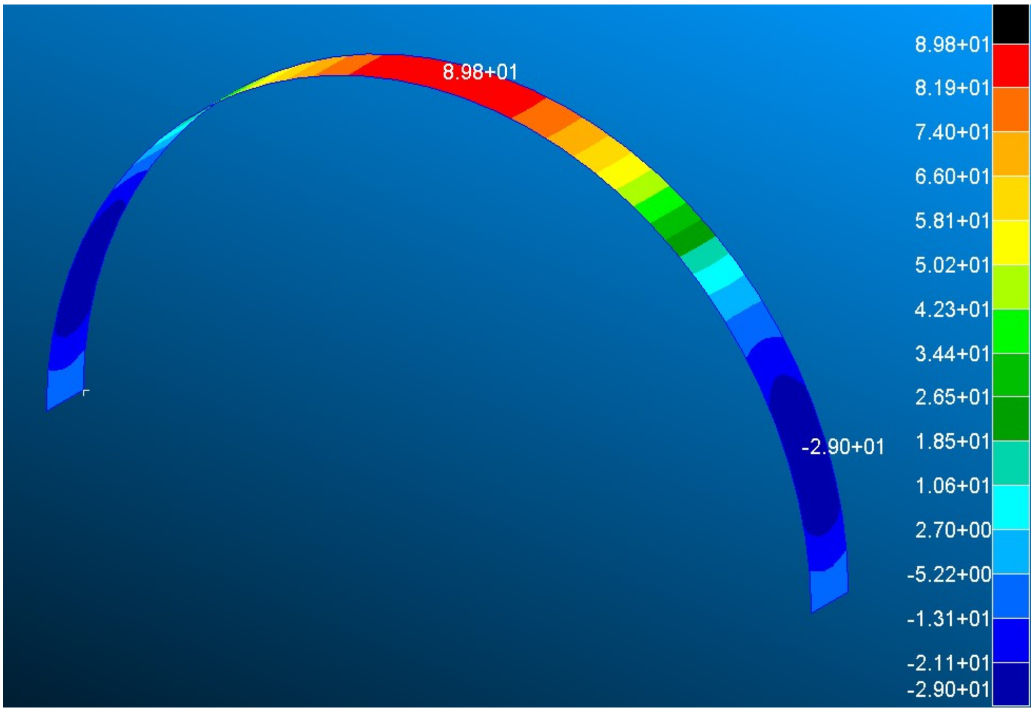

Figure 6.21: Stress in the inner part of the equivalent Dyneema layer.

The stresses inside the core change also along with the thickness, depending on which faces are connected to it. As it can be seen in the picture, on the top of the arch the upper side of the core is compressed due to the connection with the carbon layer while the lower side is in traction due to the connection with the equivalent Dyneema layer. The part of the core near the hinges is totally compressed. In the **Fig. 6.22** is shown that the stresses go from 0.38 *MPa* to -0.26 *MPa*.

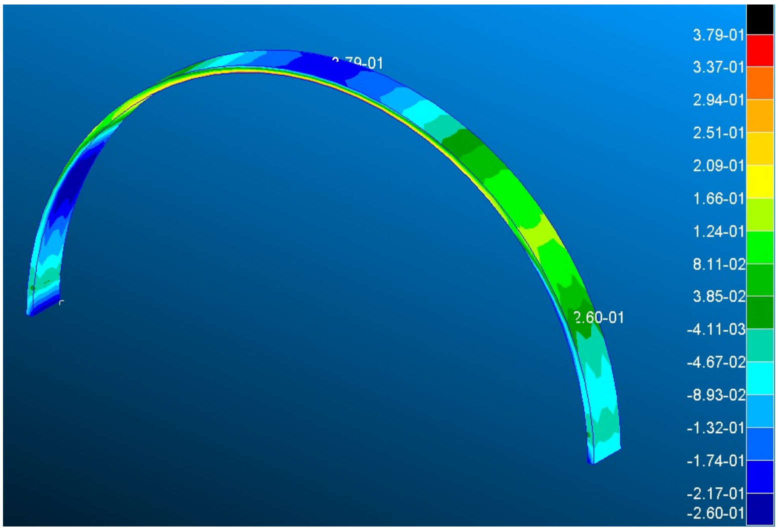

(a)

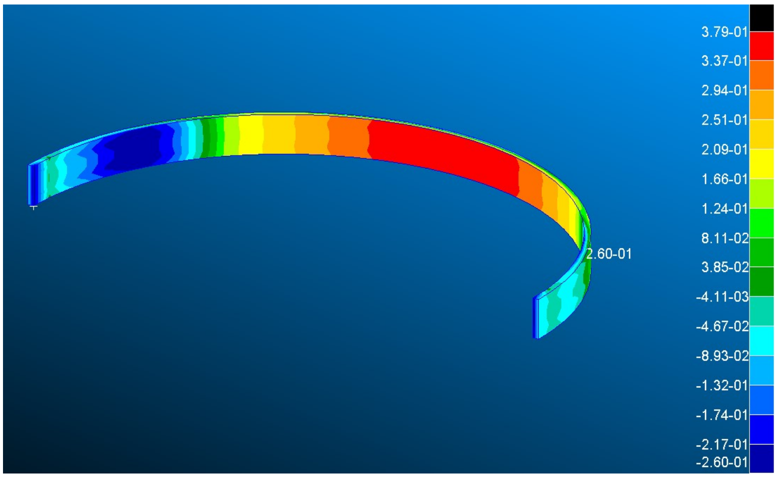

(b)

Figure 6.22: (a) Stresses in the core (Top View) (b) Stresses in the core (Down View)

It is important to notice that all the stresses reported for this analysis are lower than the ultimate stresses of each material.

6.7 Multi-arch FEM model

From the analysis of a single arch then a configuration with more arches is taken into account. This because the final structure is a multi-arch structure where the gaps between each arch are filled with the equivalent Dyneema, in order to have something flexible and resistant at the same time.

The structure is formed by eight semi-arches that are all connected to an octagon with each side long 500 *mm*. The octagon is necessary to have a regular geometry and also a geometry that is easy to create from a technological point of view and where is easy to construct a mesh. Each semi-arches has a radius of 3500 *mm* and width of 500 *mm* as the arches previously analyzed. The structure considered is shown in **Fig. 6.23**

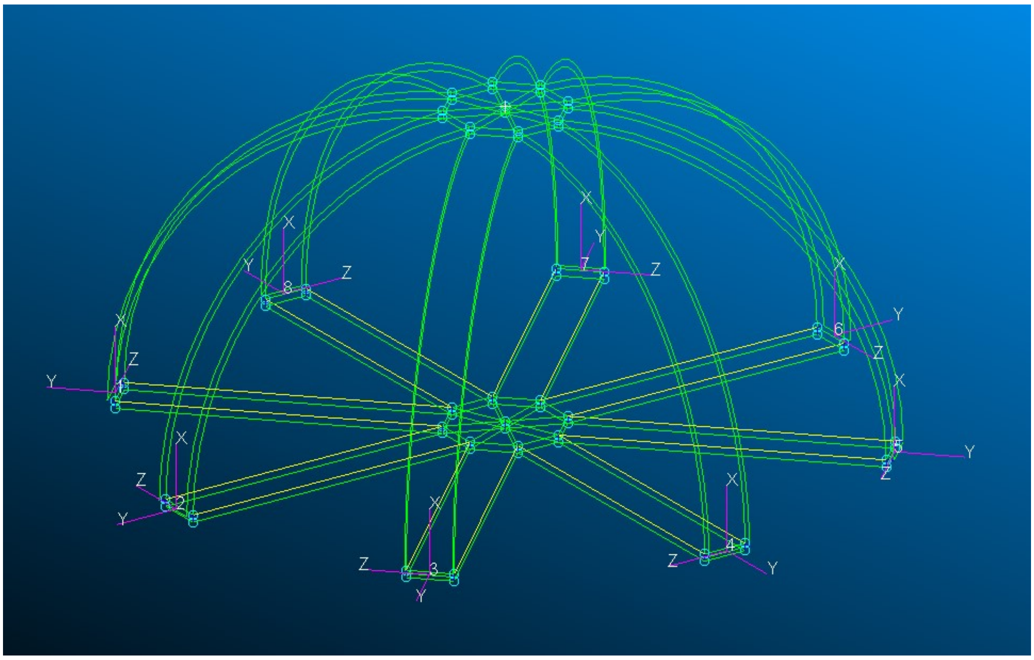

Figure 6.23: Geometry of the multi-arch structure.

The floor is even thought with eight branches connected to the octagon, and they have the same geometry as the upper structure. The floor will be made in MadFlex too, in order to give symmetry and continuity to the whole structure. The upper structure and the floor are connected by the hinges to give movement and to permit the folding of the structure. The mesh for this structure is the same as the previous arches analyzed, except for the octagon that is a new part.

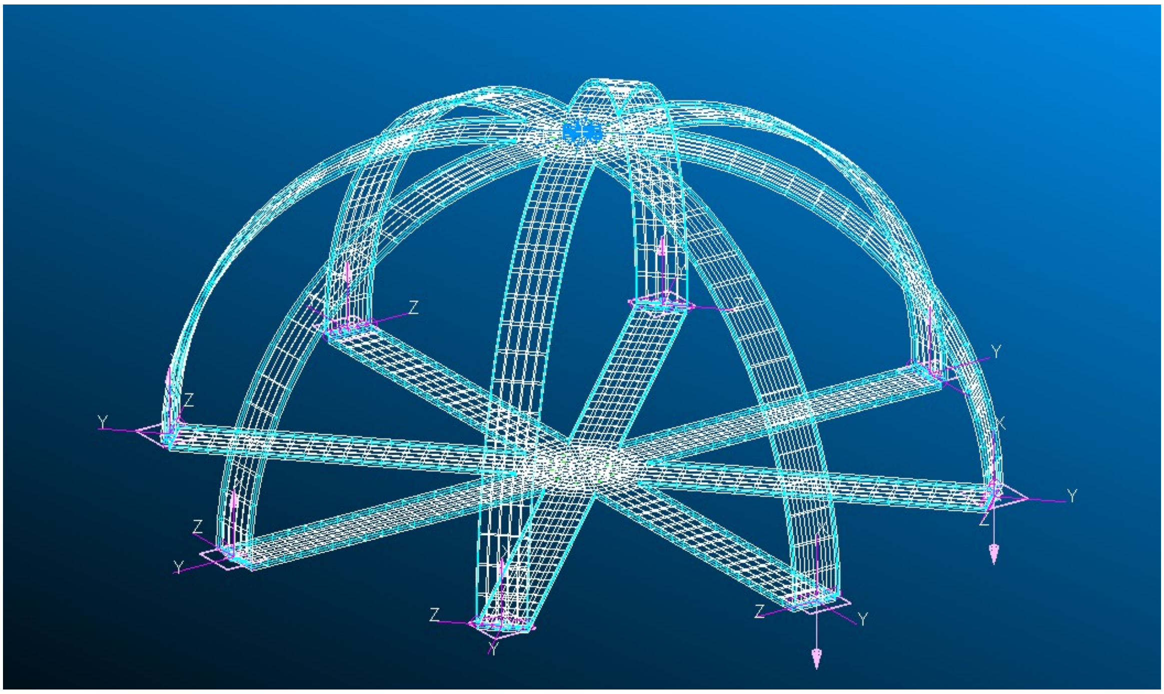

Figure 6.24: Multi-arch mesh.

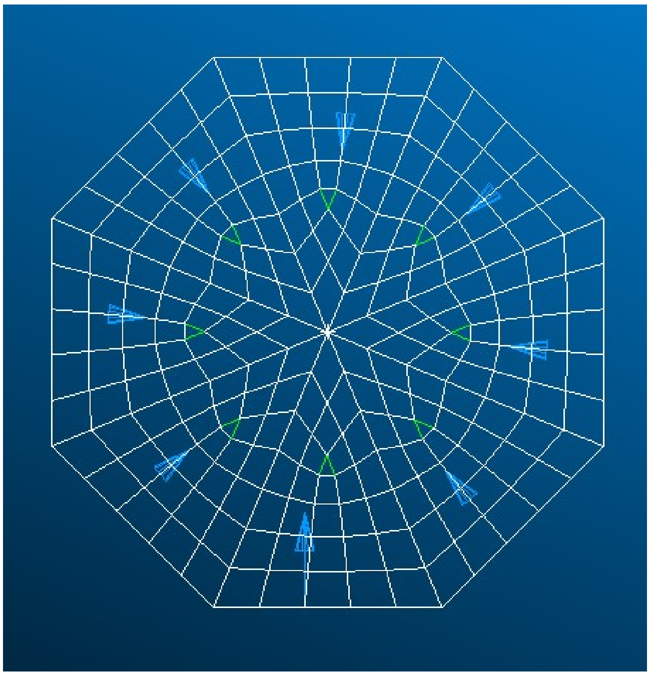

Figure 6.25: Octagon mesh.

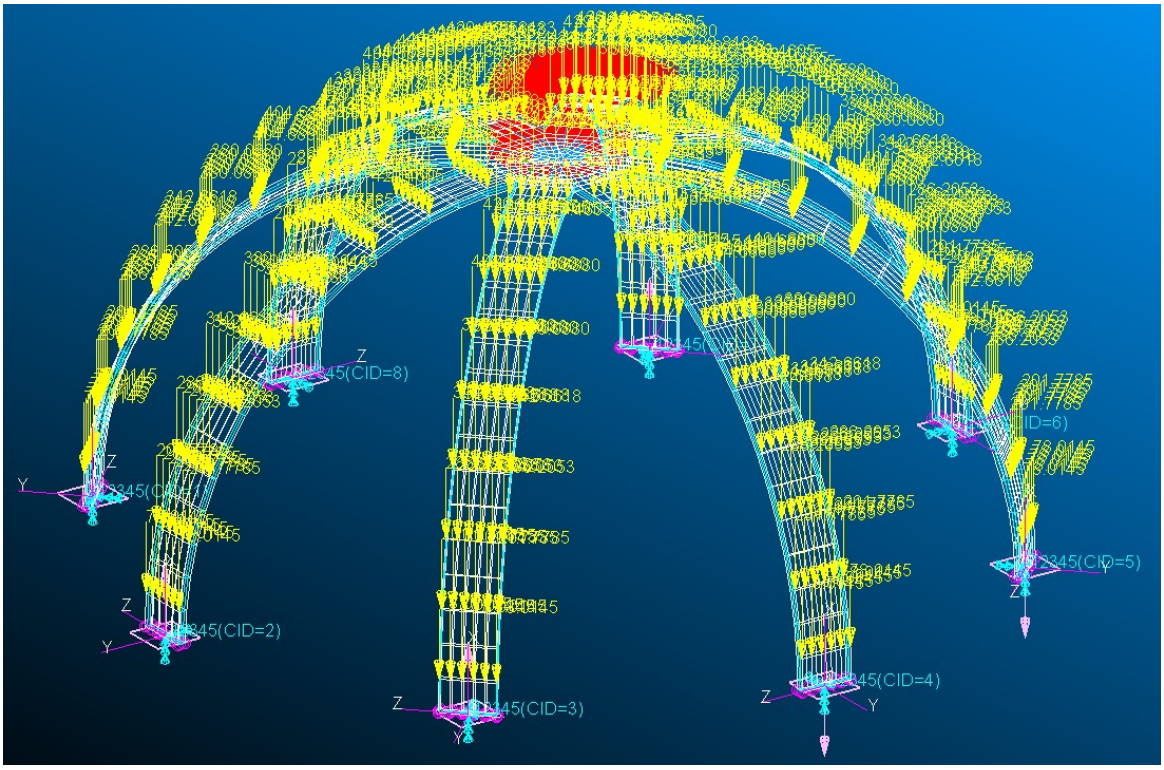

Figure 6.26: Loads on the upper structure.

The load on the semi-arches is the same as considered in the previous analysis. The load on the octagon is calculated by considering the octagon area, 1207000 mm^2, the height of the column of regolith on this octagon, 1650 mm, the density of the regolith, 1400 kg/m^3 and the Mars surface gravity, 3.71 m/s^2. The pressure generated by this volume of regolith is 0.0086 MPa. In **Fig. 6.26** is only shown how the loads appear on the upper structure. In parallel to this multi-arch structure is analyzed also a single arch similar to the arches already studied but with the only difference that there is a rectangular plate, as show in **Fig. 6.27**, which represents a section of the octagon. This in order to have a single arch to compare with the complete structure.

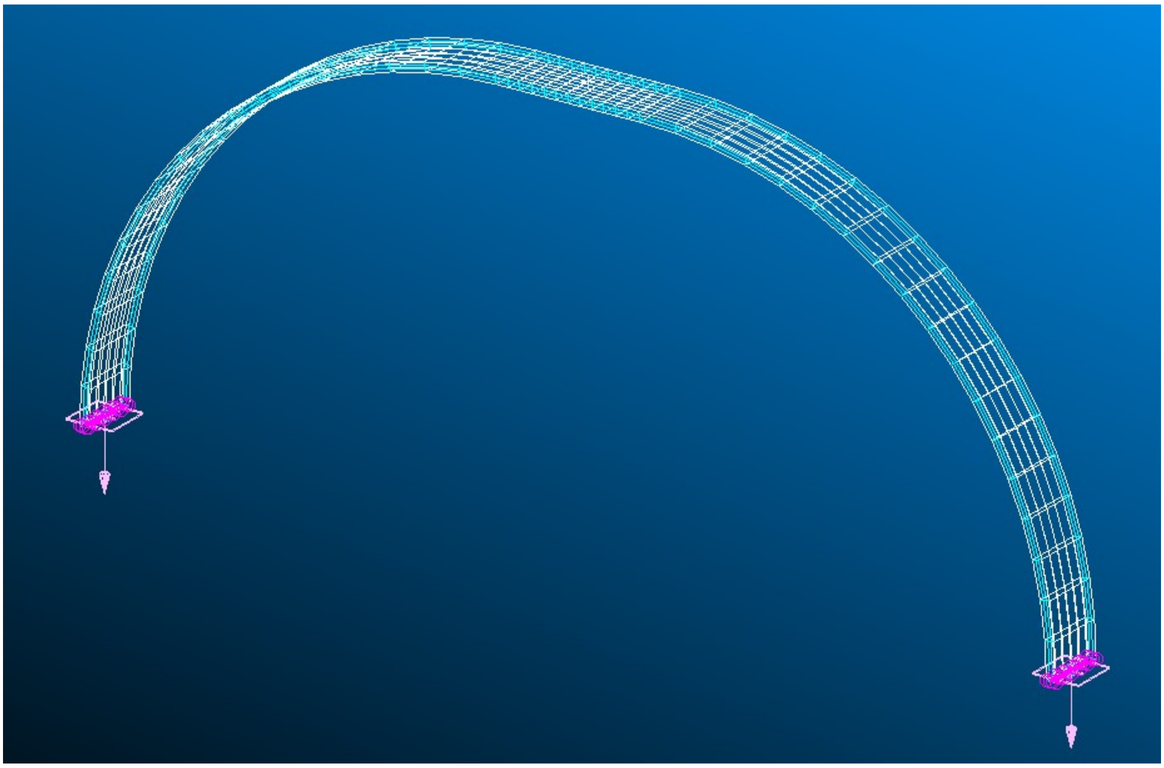

Figure 6.27: Single section of the multi-arch structure.

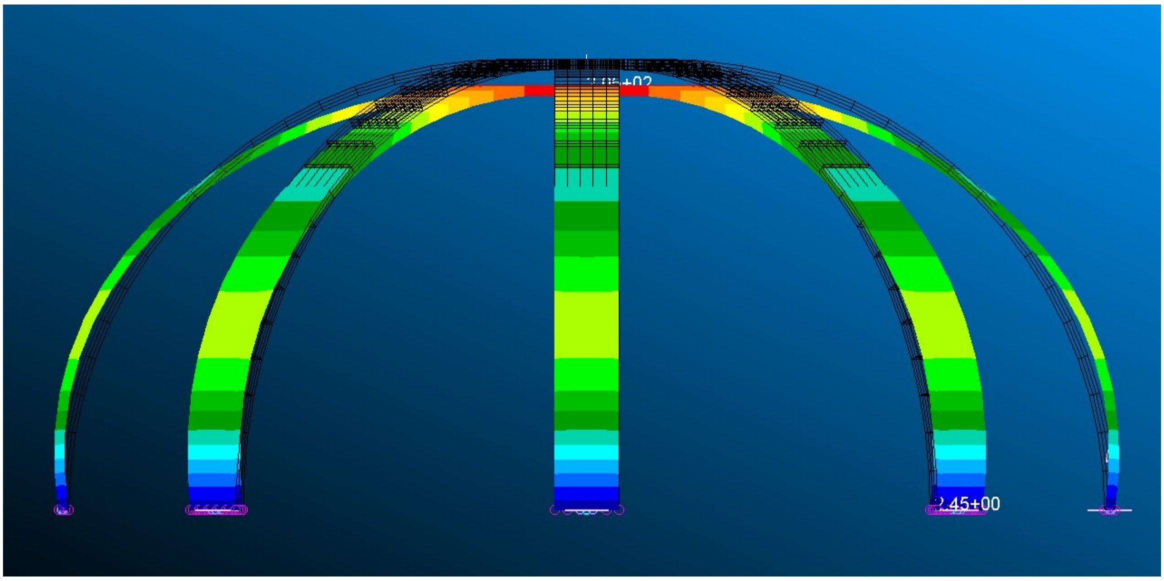

Figure 6.28: Displacement of the multi-arch structure top.

As mentioned the arches are made of MadFlex, while the upper octagon is always a sandwich structure, but the upper and lower faces are made of a carbon fiber laminate with a total thickness of 2.8 *mm* each. The first analysis is only on the upper part of the multi-arch structure. This because in absence of the intern pressure is the most stressed part. The analysis considered all the semi-arches hinged and the displacement of the top of the structure is shown in **Fig. 6.28**, and as it can be seen is 205 *mm*. This result is compared with the displacement of the single arch that considers the presence of the section of the top octagon, and is shown in fig. As it can be seen, the single arch has a top displacement of 264 *mm*, which is higher than the displacement in the multi-arch. This difference is something expected because the multi-arch structure is a more rigid configuration.

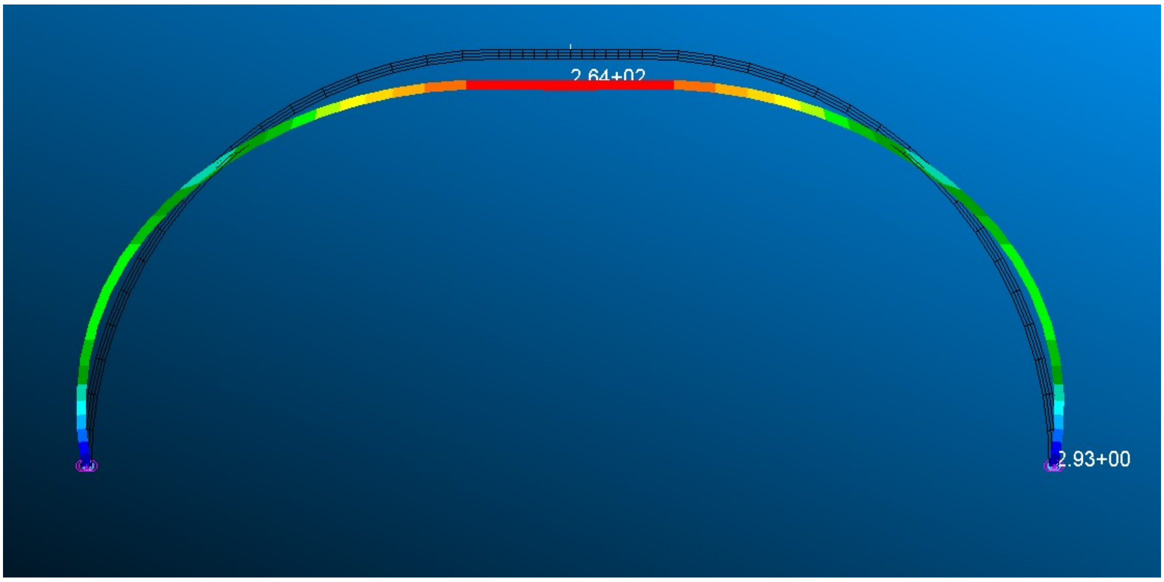

Figure 6.29: Displacement of the top of the multi-arch structure section.

Are now reported the stresses in each part of the structure, only the more stressed part will be shown, which are the outermost layer of the carbon laminate and the inner part of the equivalent Dyneema layer.

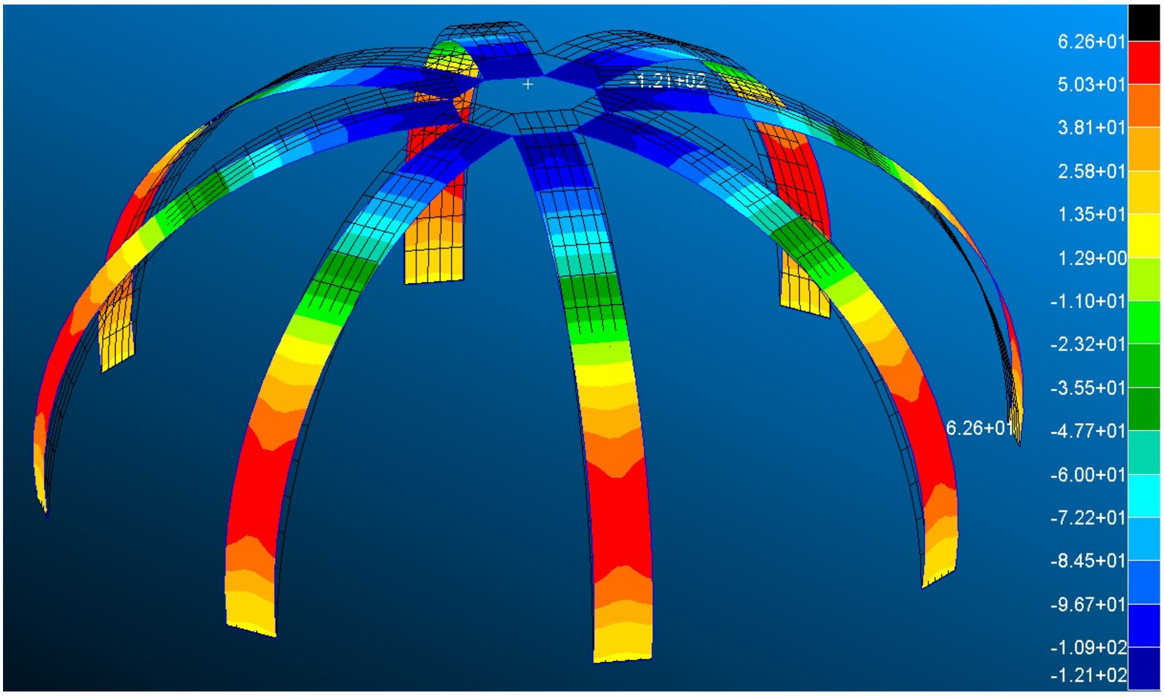

Figure 6.30: Stresses in the outermost layer of the carbon laminate.

The distribution of the stresses in this analysis is the same as in the previous analyses of the single arch. In the outermost carbon layer, the stresses go from -121 *MPa*, in the top of the structure, to 63 *MPa* near the hinges. For the inner part of the equivalent Dyneema layer, the stresses go from 110 *MPa*, in the top of the structure, to -35 *MPa* near the hinges. Similar stresses to the carbon layer and equivalent Dyneema layer are also seen in the faces of the octagon sandwich at the top of the structure.

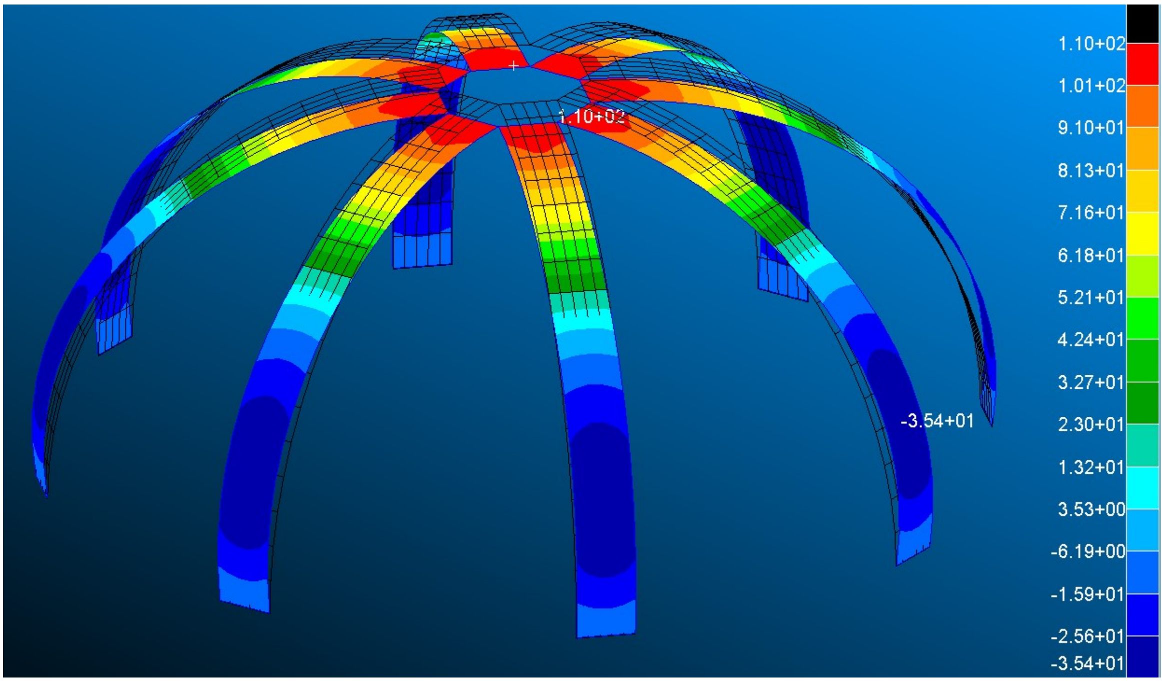

Figure 6.31: Stresses in the inner layer of the equivalent Dyneema face.

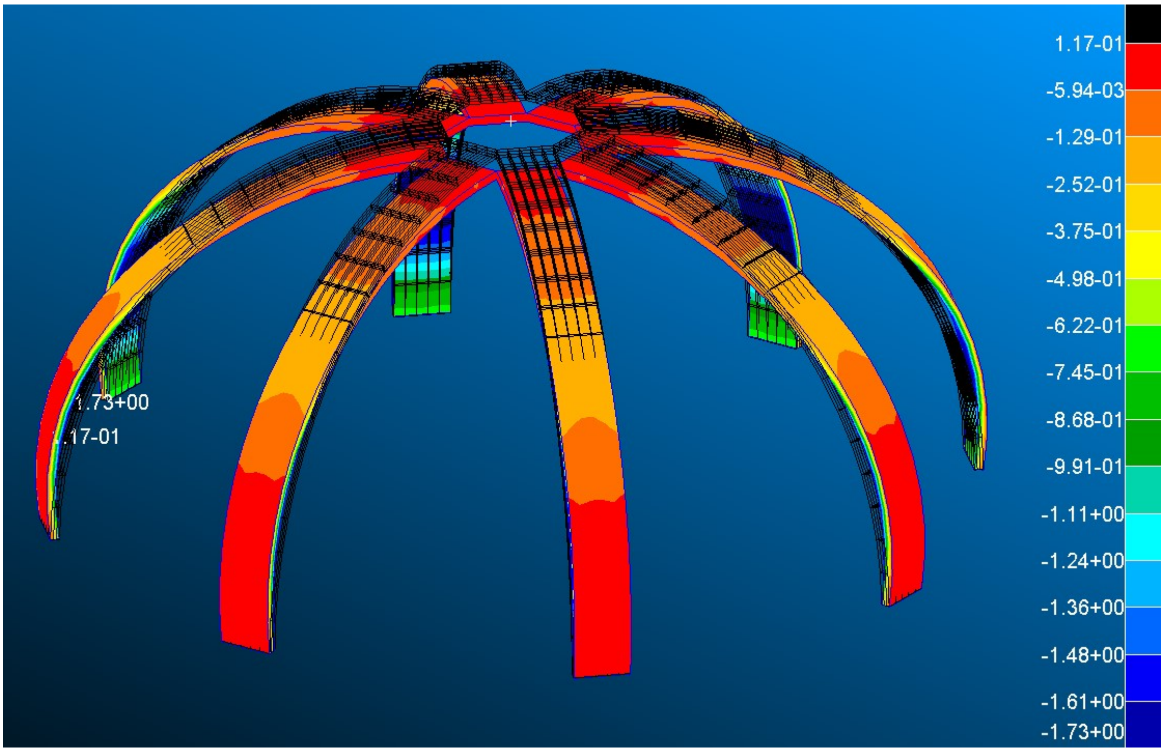

Figure 6.32: Stresses in the Rohacell core of the sandwich.

The stresses in the core change along with the thickness depending on which faces are connected. The stresses go from 0.117 *MPa* to -1.73 *MPa*. The same values are observed in the core of the sandwich octagon.

This configuration has to be analyzed even in the configuration with the inside pressure of 1 *atm*. Which is the real condiction for the habitat. The pressure is applied to the inner part of the structure and the deformation of the structure when both pressure and regolith load are applied is shown in **Fig. 6.33**

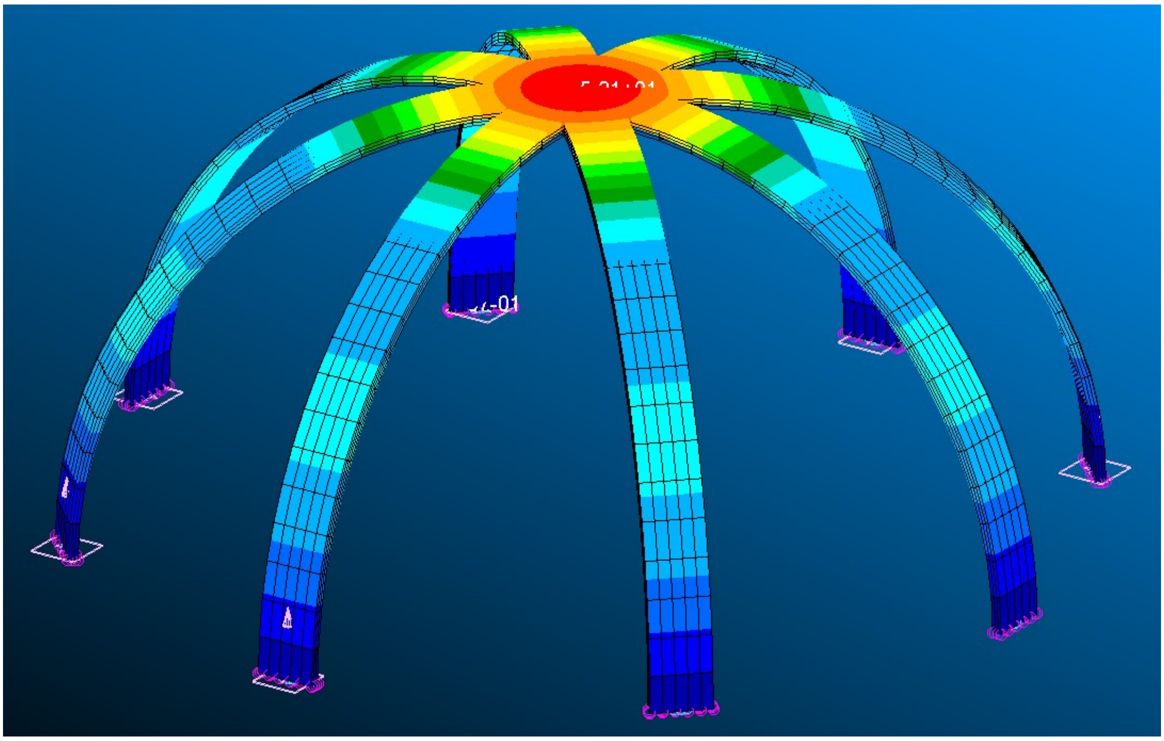

Figure 6.33: Displacement of the top of the multi-arch considering regolith and pressure.

As it can be seen the load generated by the pressure is higher than the one of the Martian regolith, the displacement is upward with a value of 52 *mm*.

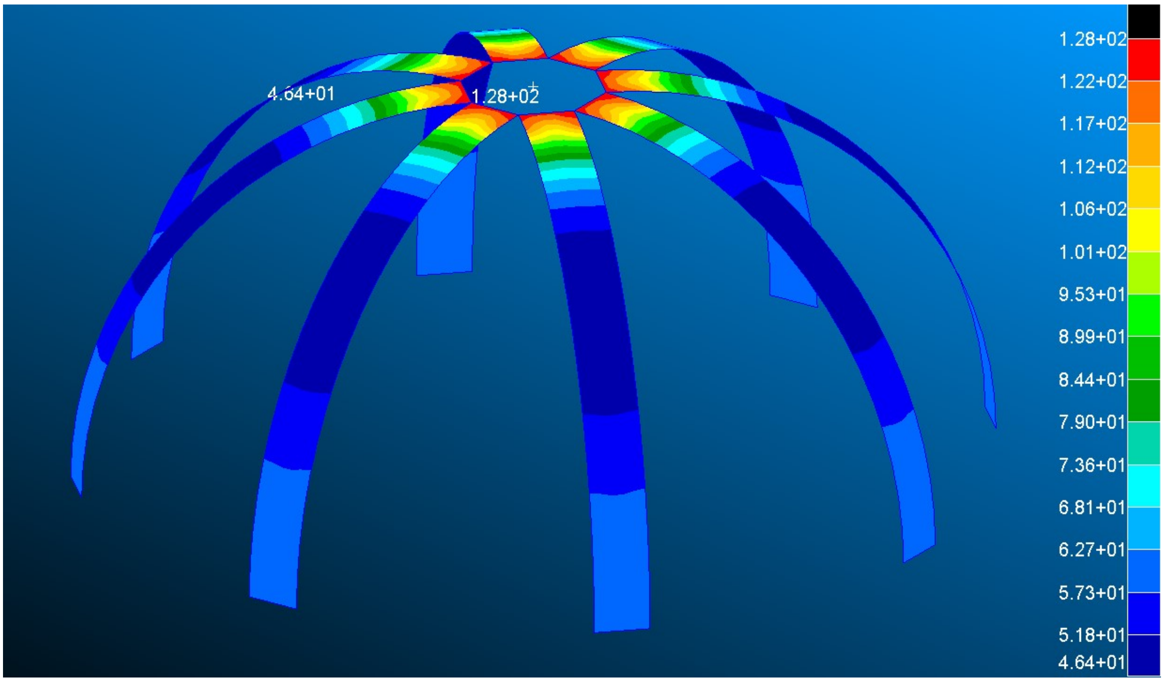

Figure 6.34: Stresses in the outermost carbon layer.

The structure with the inside pressure is almost all in traction condition. As it can be seen in the pictures the outermost carbon layer in the upper face of the sandwich is totally in traction with

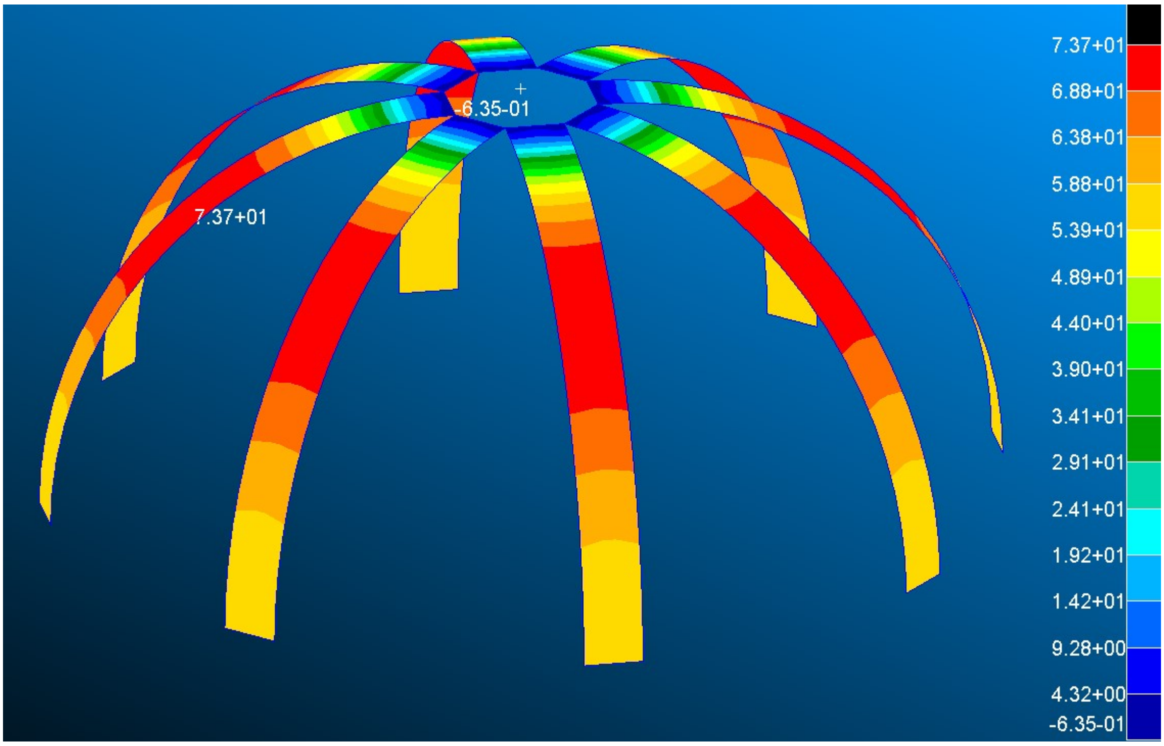

Figure 6.35: Stresses in the inner layer of the equivalent Dyneema.

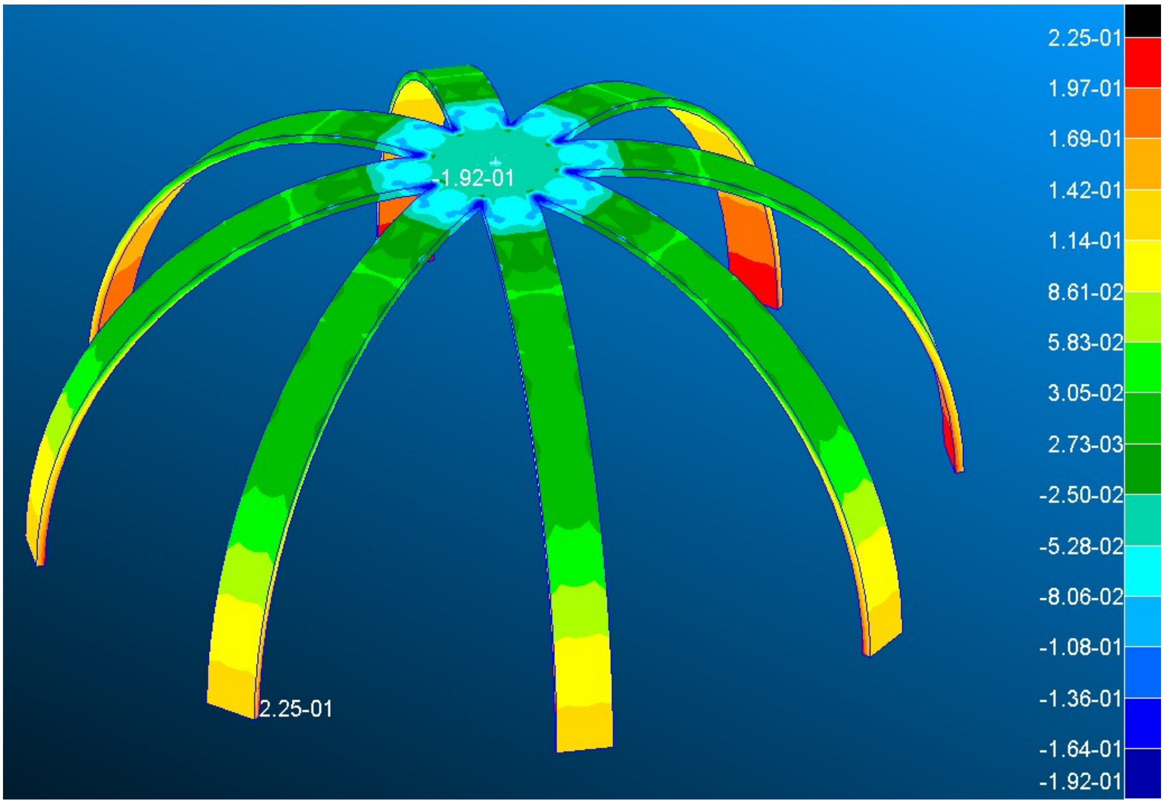

Figure 6.36: Stresses in the Rohacell core of the sandwich.

stresses from 46 to 128 *MPa*. The inner layer of the equivalent Dyneema face is for the most in traction with the exception of a little part near the octagon and the stresses go from 74 to -0.64 *MPa*. The core is also for the most in traction, just in points located near the octagon there is a compression state and

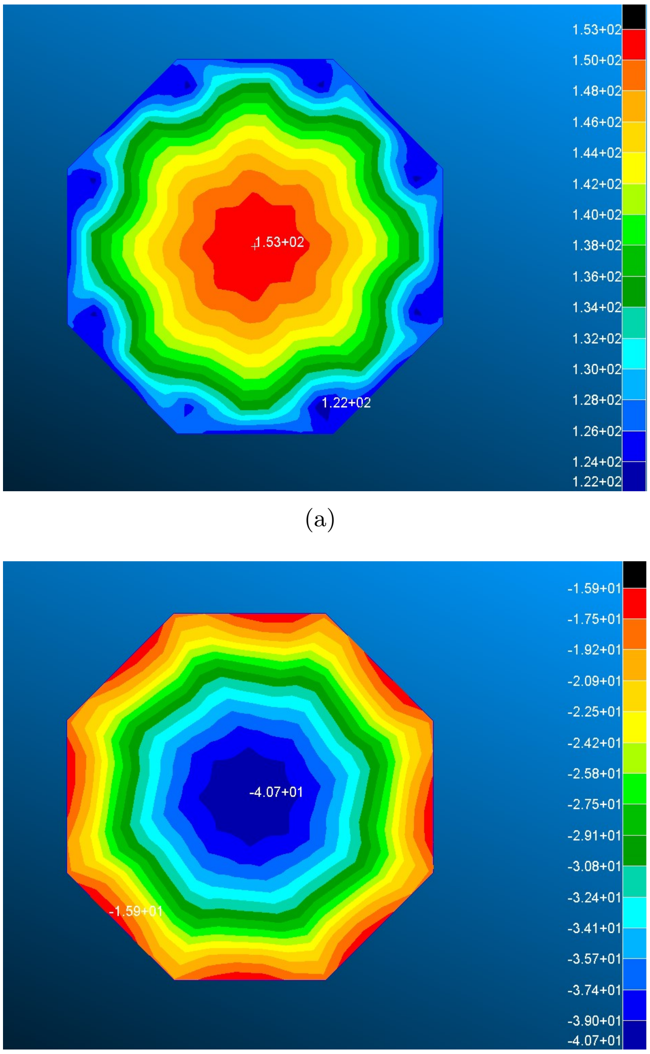

Figure 6.37: (a) Stresses in the octagon outermost carbon layer (b) Stresses in the octagon inner part of the carbon laminate

the stresses go from 0.23 to -0.19 *MPa*. The faces of the octagon have stresses similar to the semi-arches, the upper face is totally in traction while the lower face is compressed with maximum values of 152 *MPa* and -40 *MPa*.

The complete structure will be now considered. The gaps between the arches are now filled with a 5 *mm* layer of equivalent Dyneema. The load case is always the same, and is also considered the regolith on the new layer of equivalent Dyneema. The load on the gaps between the arches are calculated from the volumes of regolith, divided in the same portion as the volume of regolith on the arches, the only difference is that the volumes on the arches have all the same width while the volumes on the gaps have different width ad base area. In the **Fig. 6.38** is shown the subdivision of the volumes

The displacements of the complete structure present a maximum in the displacement for the equivalent Dyneema layer, reaching a value of 153 *mm*. Considering the arches there is also a reduction in the displacement of the top of the structure, it goes down just 48 *mm*. These results show how the complete structure is more rigid than the multi-arch structure without the filled gaps.

Focusing on the stresses in the arches, the distribution of the stresses is the same as in the

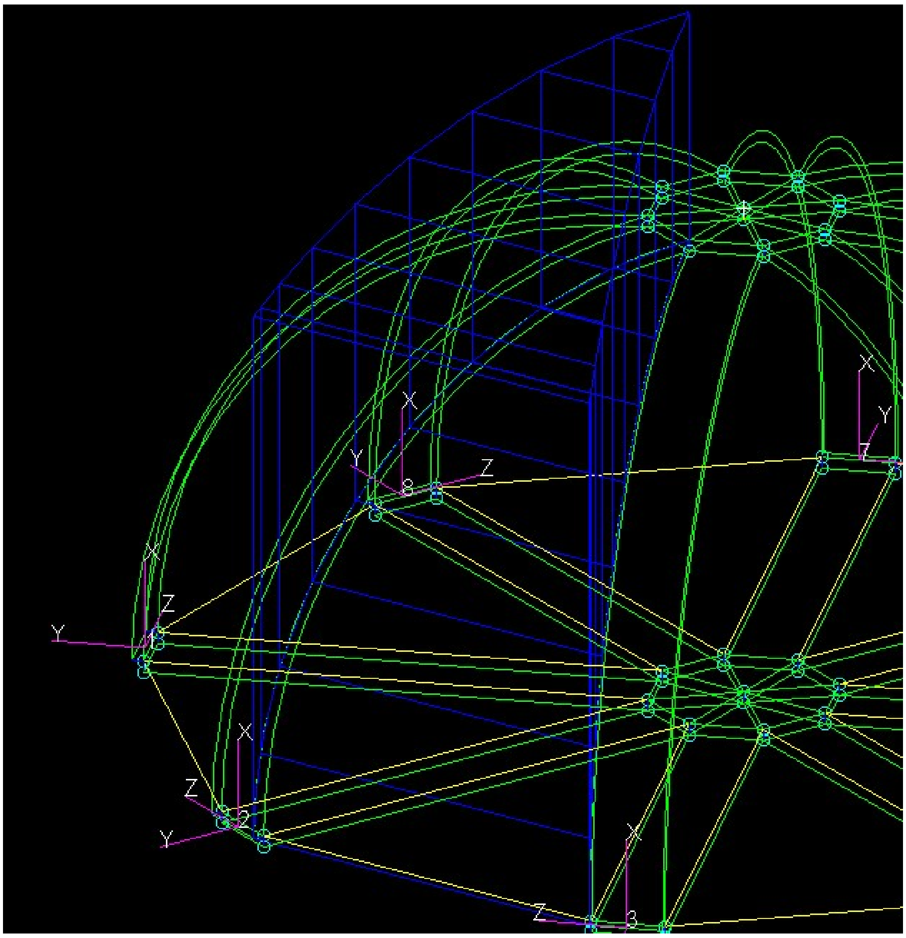

Figure 6.38: Subdivision of the volumes on the gaps.

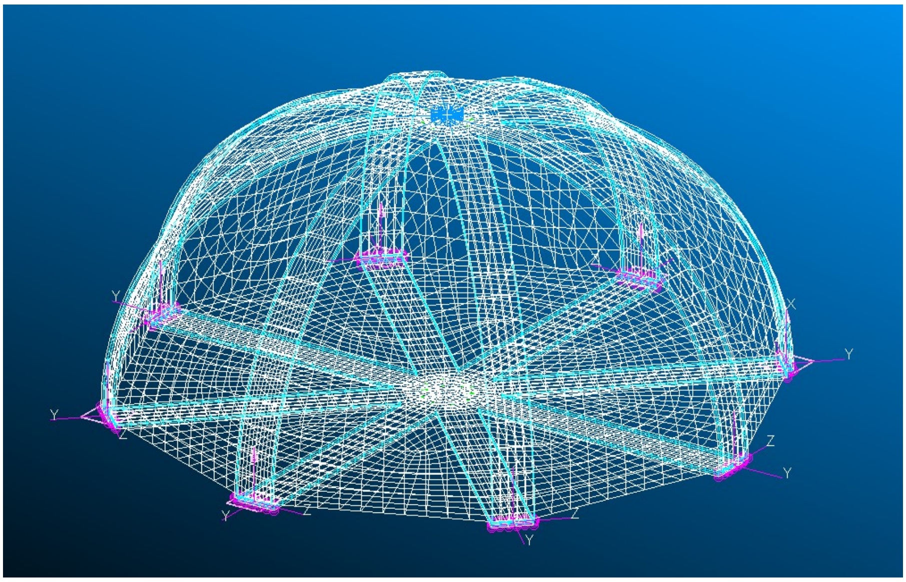

Figure 6.39: Complete multi-arch structure.

previous analysis. In the outermost carbon layer, the stresses go from -32 *MPa*, in the top of the structure, to 15 *MPa* near the hinges. For the inner part of the equivalent Dyneema layer, the stresses go from 28 *MPa*, in the top of the structure, to -9 *MPa* near the hinges. Similar stresses to the carbon layer and equivalent Dyneema layer are also seen in the faces of the octagon sandwich at the top of the structure.

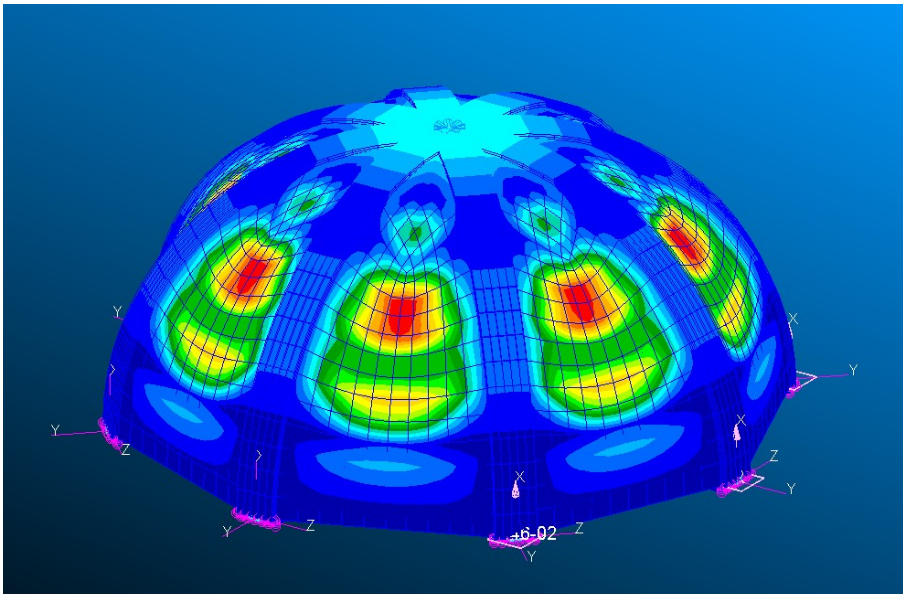

Figure 6.40: Displacements of the complete structure.

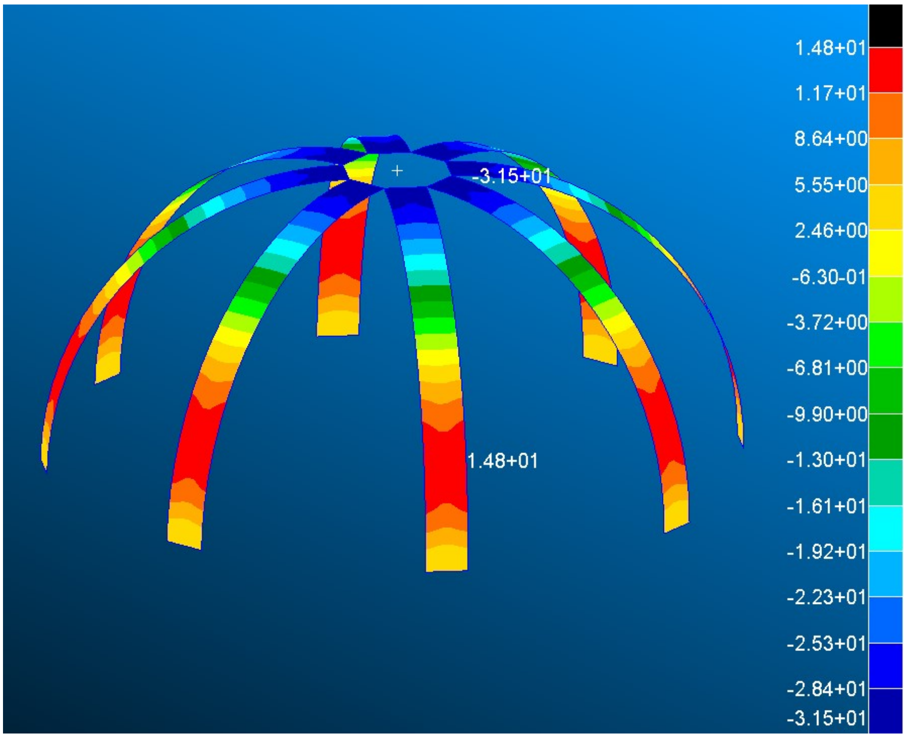

Figure 6.41: Stresses in the outermost carbon layer.

The stresses in the core, for the arches and the octagon, change along with the thickness depending on which faces are connected. The stresses go from 0.12 MPa to -0.1 MPa. The equivalent Dyneema layer in the gaps is entirely in traction reaching a stress of 104 MPa. For the faces of the octagon, the upper face is in compression and the stress is -38 MPa for the outermost layer. The lower face is in traction with a stress of 30 MPa. Considering even in this complete structure, an inside pressure, the displacement is 0.127 mm upwards. While the equivalent Dyneema layer in the gap has a displacement of 14 mm outwards. As it can be seen in the pictures the outermost carbon layer in the upper face of the sandwich is almost all in traction with a maximum stress of 102 MPa while there are some zones with a compression of -134 MPa. The inner layer of the equivalent Dyneema face is for the most in traction

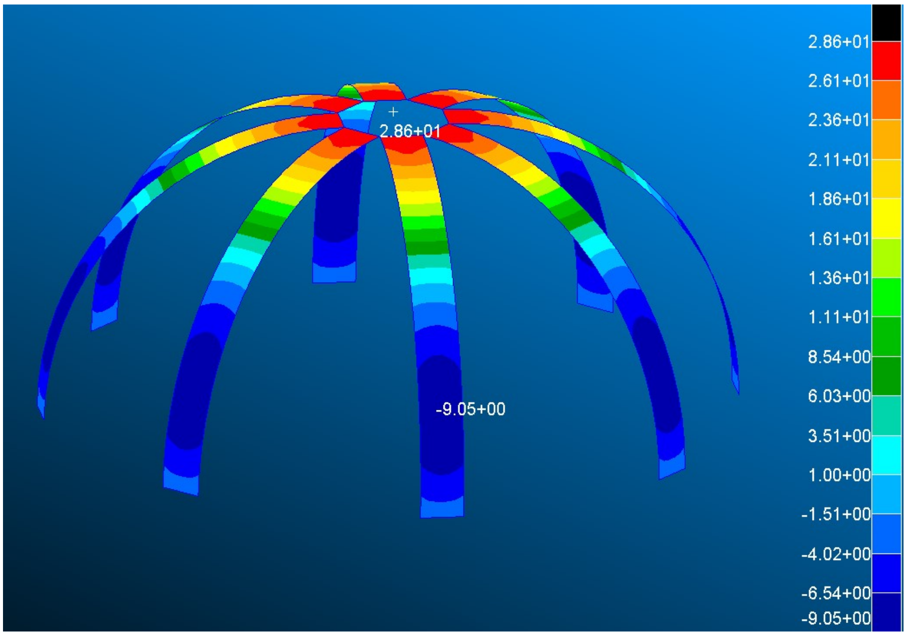

Figure 6.42: Stresses in the inner layer of the equivalent Dyneema.

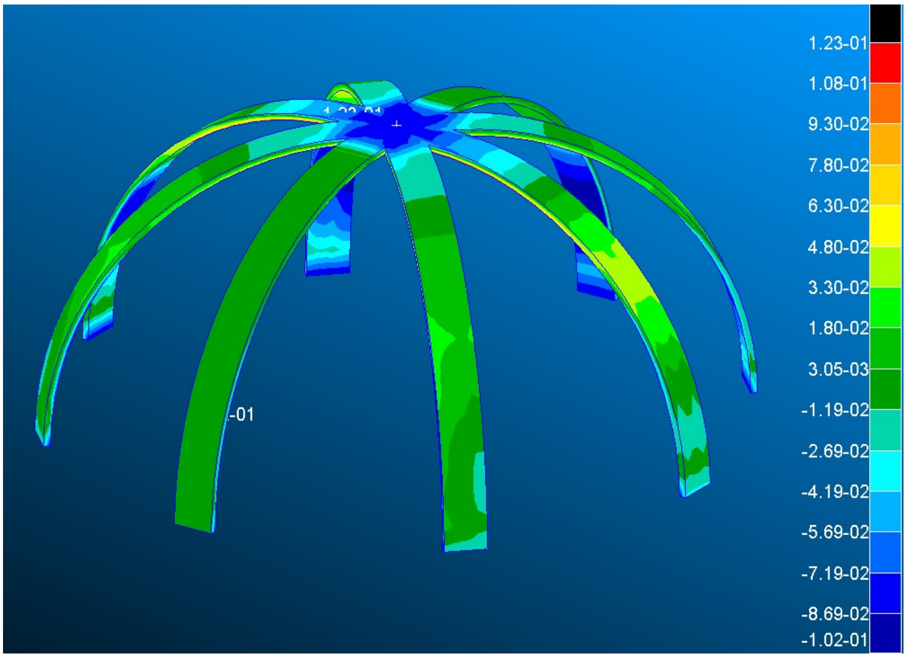

Figure 6.43: Stresses in the Rohacell core of the sandwich.

with the exception of a little part near the octagon and the stresses go from 188 to -40 MPa. The core is also for the most in traction, just in points located near the octagon and in the interface between the gaps and the archs there is a compression state and the stresses go from 0.86 to -0.73 MPa. The faces of the octagon have stresses similar to the semi-arches, the upper face is totally in traction while the lower face is compressed with maximum values of 128 MPa and -2.4 MPa.

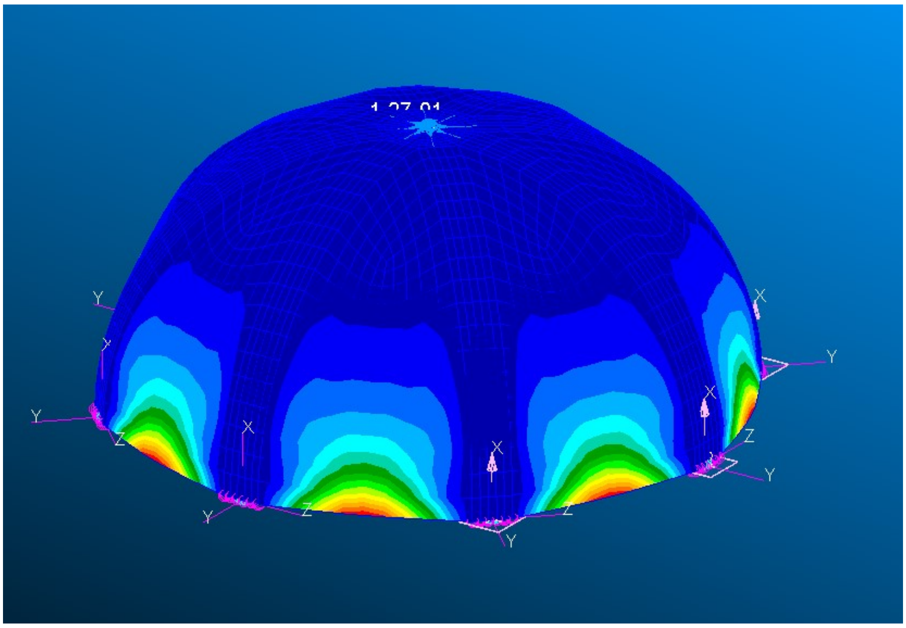

Figure 6.44: Displacements of the complete structure with the inside pressure.

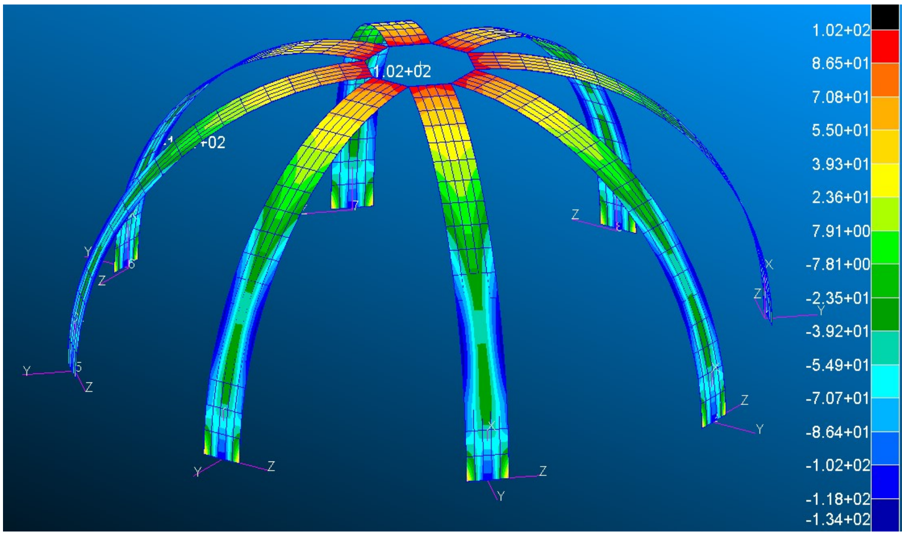

Figure 6.45: Stresses in the outermost carbon layer.

6.8 Safety factor and ultimate loads

Considering the previous results, looking at the stress in the structure, all of them are below the ultimate stress in **Tab. 6.2**. The habitat has to resist a journey to Mars, land on the surface of the planet and protect the astronauts while resisting the regolith and the internal pressure. In order to satisfy this achievement it is necessary the use a safety factor which is the prior knowledge and experience that engineers have on material's behaviors chosen for the structure, and on environmental characteristics which determine the external load conditions. In case of a failure of the structure, it is impossible to repair it and also the habitat will be the first tentative for the colonization of Mars. These thoughts are also based on manual book about lunar exploration. Considering what was reported in [14] "the range for the factor of safety on Earth is [...] approximately between 1.7 and 3.5. All of the problems and uncertainties on the Moon will certainly require higher safety factors, so factors of safety of 4.0 or higher seem reasonable.". From this consideration, a safety factor (SF) of 4 is chosen for this structure.

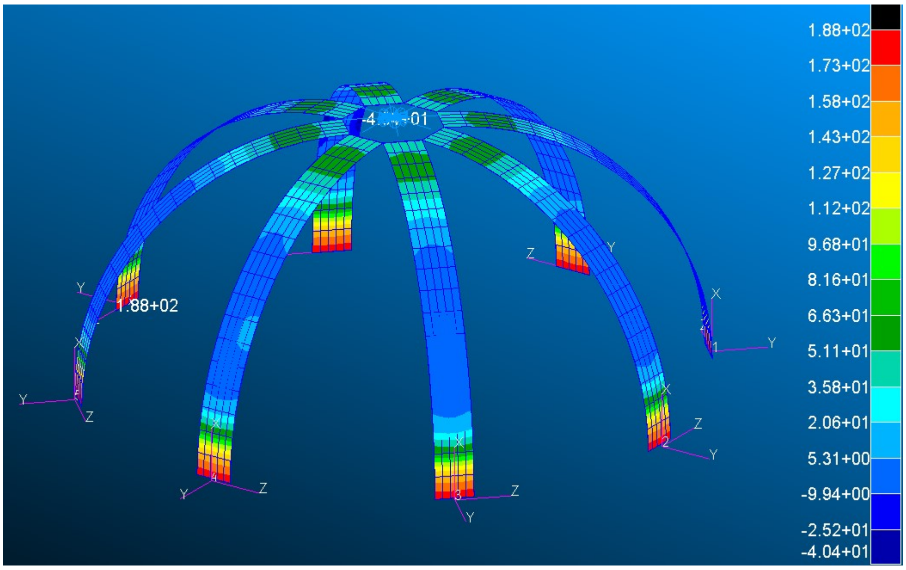

Figure 6.46: Stresses in the inner layer of the equivalent Dyneema.

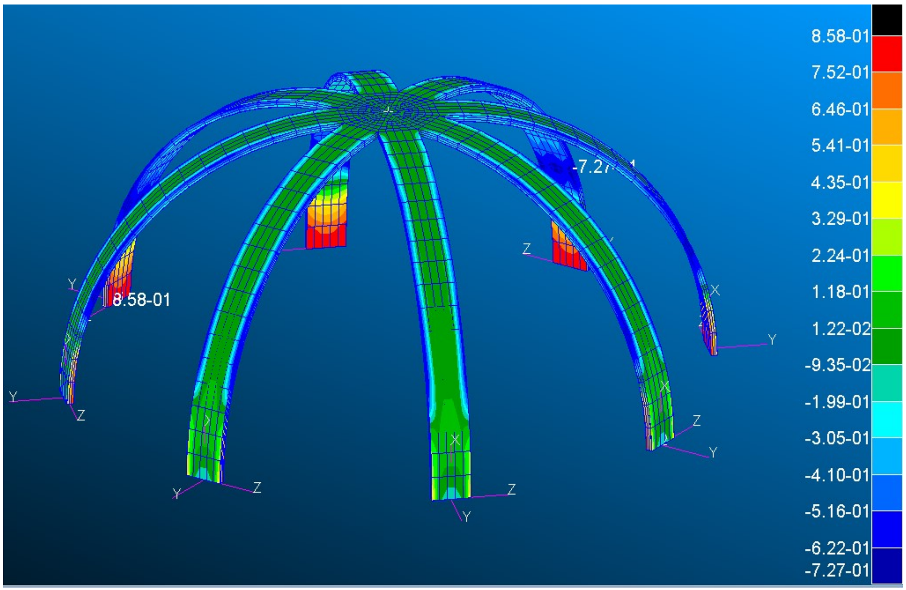

Figure 6.47: Stresses in the Rohacell core of the sandwich.

With this SF the traction stresses in the carbon laminate must be below a value of 150 *MPa*, while the compression stresses must be below 143 *MPa*, considering the ultimate stress in **Tab. 6.2**. In all the previous analyses the stresses are below this value, except for the configuration without the gaps filled with the equivalent Dyneema, but it is not a problem because it is not the final structure thought to be on Mars.

For the Rohacell in the core, the stresses must be below a value of 0.93 *MPa* in traction and 0.9 *MPa* and the stresses in the final structure are below them.

In the equivalent Dyneema, an equivalent ultimate stress of 1000 *MPa* is considered, and with a SF of 4 the stresses must be below 250 *MPa* in traction. While the compression is not considered due to the microbuckling of the Dyneema. In all the cases analyzed the stresses are below 250 *MPa*. So from this point of view the structure is in safety.

6.9 Buckling condition

To assure the safety of the structure is important to know if the structure is in buckling, which can compromise the working of the habitat. Sometimes the buckling load could be lower than the ultimate stress of the material, and that is the reason why the only chacking of the ultimate stresses is not enough to assure the safety of the structure. In chapter 4 the types of buckling for sandwich structures is explained and considering the equations **3.1** and **3.2**, the stress value to avoid the face wrinkling will be calculated for the carbon layer while for the Dyneema layer is not considered because it is already known that the Dyneema is in a microbuckling situation when compression is applied.

From the first empirical equation, the stress value is 488 MPa, while with the second empirical equation the stress value is 512 MPa. From the analyses all the compression stresses in the carbon layer are highly below these values, that is could be also related to the thickness of the carbon, which is high compared to the thickness of the faces of the sandwich structure in commerce.

Once observed in this local buckling condition the attention is turned to the global buckling of the complete structure. The focus is on the arches because the equivalent Dyneema in the gaps between the arches works like a tape and is also in a traction condition. The result from the analysis is the buckling load factor (BLF), which is a value that once multiplied by the load on the structure gives back the load that generates the global buckling of the structure. So this value has to be major than 1, in order to have a load on the structure that is less than the global buckling load.

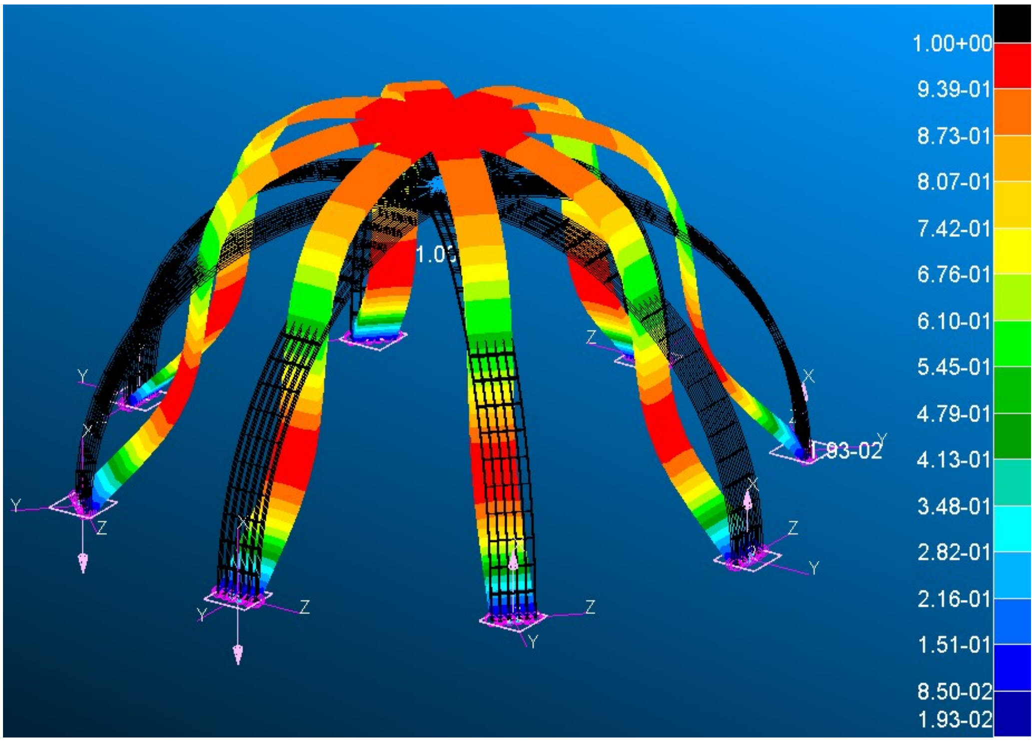

Figure 6.48: First Buckling form.

The image above shows the first buckling form, the deformation is out of scale in order to better show the assumed form. The BLF is 1.22 and this assures that the applied load is far from the critical condition, also since the BLF is far from 1, in the future optimization of the structure it will be possible to lighten the structure acting on the material thickness. The results show what was expected because the parts that first will be in buckling condition are the ones near the hinges.

Chapter 7

Comments and conclusions

In this chapter are analyzed the results previously achieved and comments on them. It is important to remember that this thesis focuses principally on the structural feasibility of the habitat thought. The analysis made in the previous chapter started from a simple configuration and gradually took into account different components in the structure. It is important to have values to compare the results with something because the job done in this thesis is something totally new especially for the material and for the type of structure selected.

7.1 The folding of the habitat

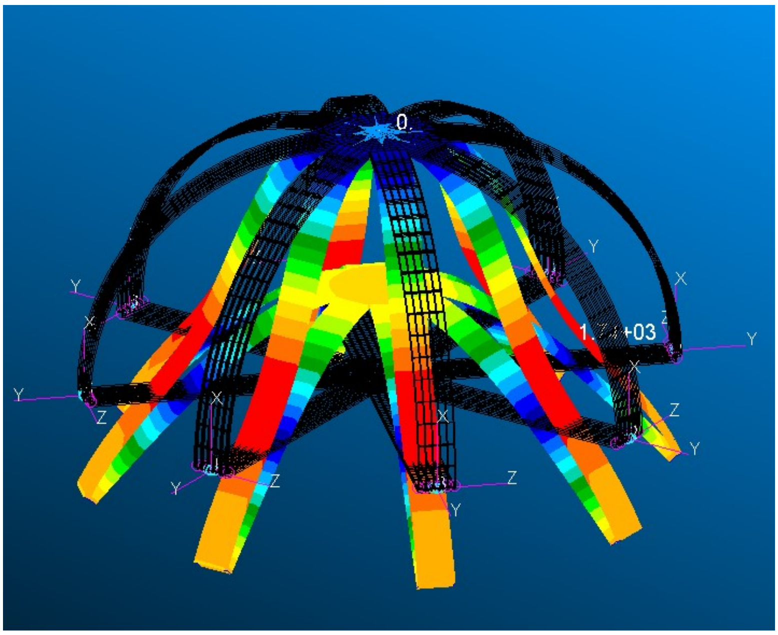

Figure 7.1: Folded structure

The most important characteristic of the habitat is analyzed to understand the volume reduction and the stresses in the structure. As it can be seen in the **Fig. 7.1** the radius of the folded structure is nearly close to half of the radius in the expanded configuration. There is also a reduction in the occupied volume giving the possibility to easily store the habitat in the fairing of a launch vehicle. This is a prevision of the capability in the folding of the structure, it is probably that in reality is more foldable. In the **Fig. 7.1**, the equivalent Dyneema layer between each arch is hidden to better see how the structure is deformed in the folded configuration.

In this configuration there a concentration of high stress in the carbon layer near the top octagon and to the octagon in the floor. This could be avoided by creating little holes in the foam to better flex the MadFlex structure, as suggested also by the MadFlex patent. Also this improvement reduces the stresses inside the core, which in this configuration are higher than the ultimate stress and go from 4.56 to -1.02 MPa but not so far from the ultimate stresses. So this problem could be easily resolved as said before. As it can be seen in the picture, the stresses in the most stressed carbon layer are always below the traction and compression ultimate stresses, but it is better to reduce them in order to respect the constraint imposed by the safety factor.

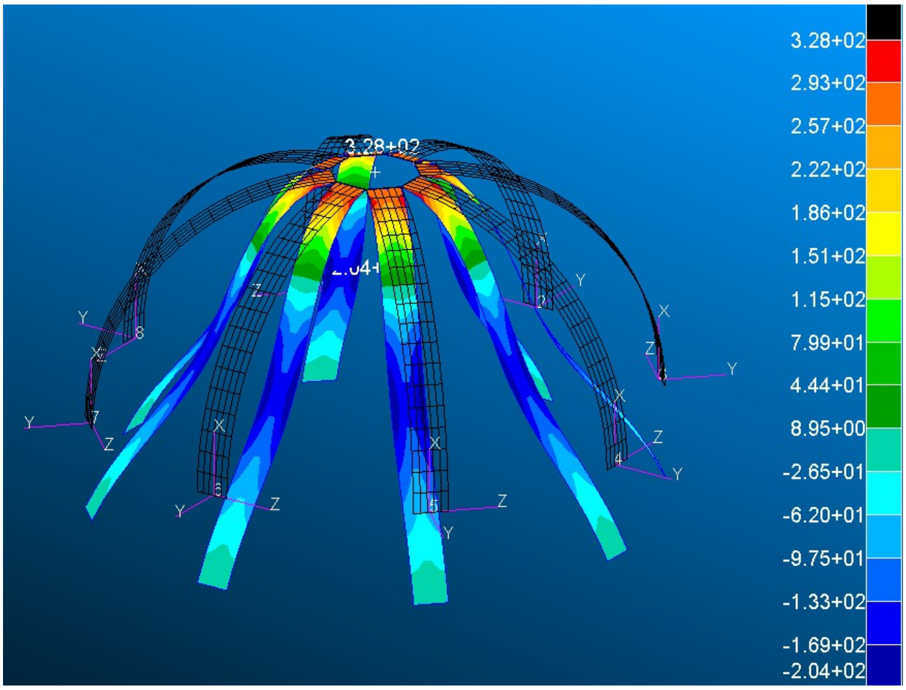

Figure 7.2: Stresses in the most stressed carbon layer in the top structure.

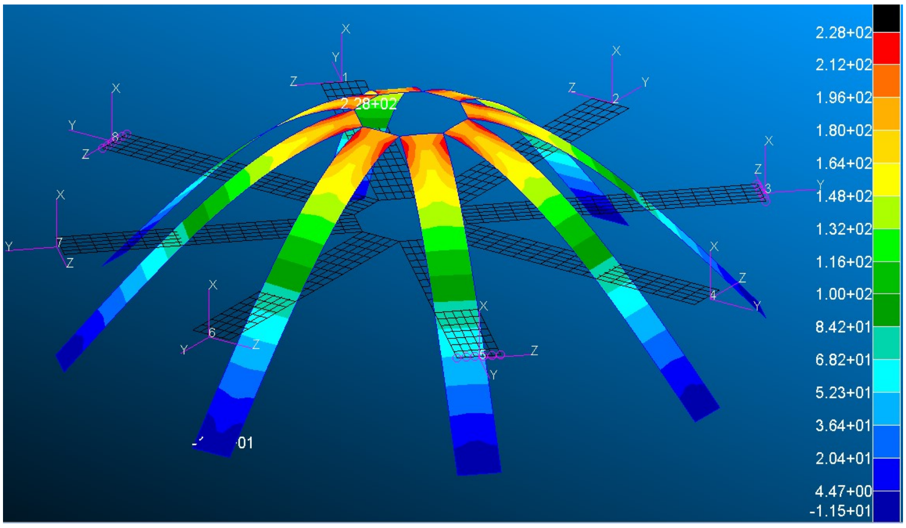

Figure 7.3: Stresses in the most stressed carbon layer in the floor.

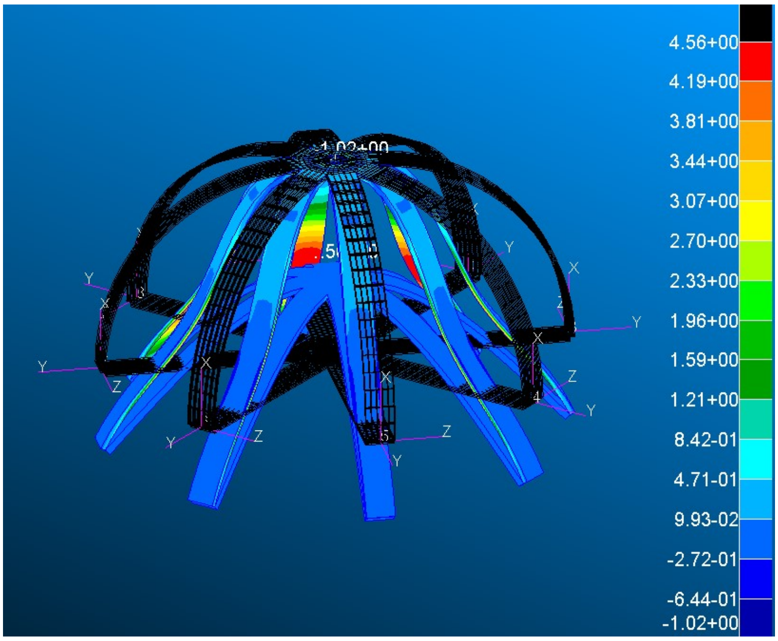

Figure 7.4: Stresses in the core of the MadFlex.

7.2 Mass properties

The whole structure has a mass of 570 kg, which another strong point of this habitat. From this mass, ideally here is reported the SLS launch vehicle how many habitats can transport

- The SLS block 1 cargo can ideally transport 51 habitats
- The SLS block 1B cargo can ideally transport 72 habitats
- The SLS block 2 cargo can ideally transport 90 habitats

So the mainly problem is not the mass but the occupied volume

7.3 Internal pressure

The structure analyzed in the previous chapter has infinite stiffness constraints (hinges) which withdraw the movement of the ends along the horizontal and vertical directions keeping them fixed at the established distance. But in the reality, this kind of constraints do not exist so it necessary a highly rigid floor or a block system that keep fixed the habitat extremity. Without this system, the structure with the internal pressure tend to assume a spherical shape as shown in **Fig. 7.6** even with the regolith on it. This problem has to be resolved with a more accurate future analysis.

7.4 First optimization of the structure

A first optimization of the structure could be done on the equivalent Dyneema layer. Considering that this layer is half compressed, the idea could be to substitute it with a carbon layer that can sustain the

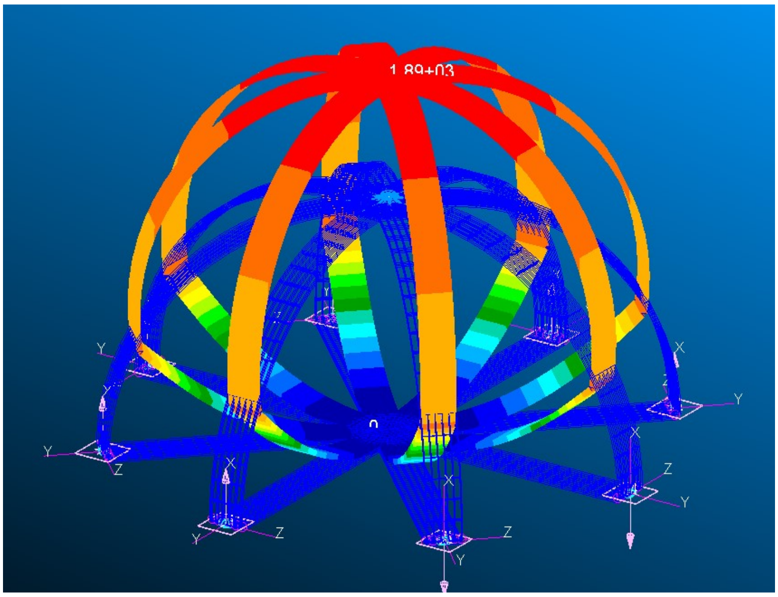

Figure 7.5: Spherical shape due to the internal pressure.

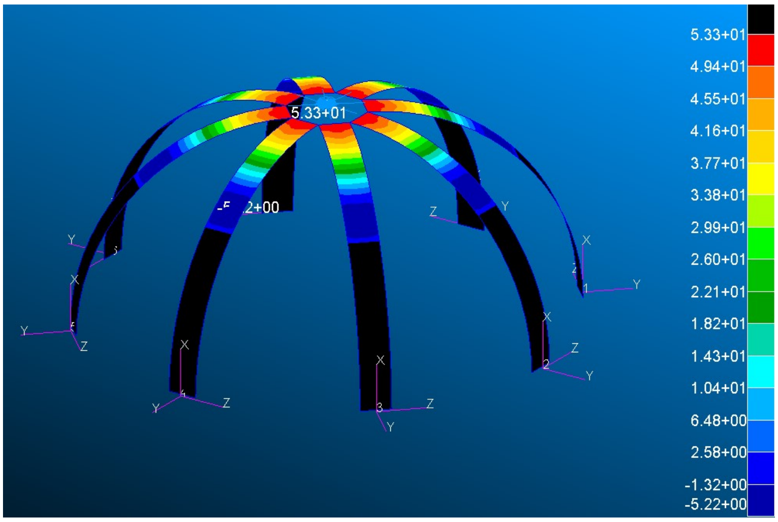

Figure 7.6: Stresses in the equivalent Dyneema layer.

compression that the Dyneema can not due to the microbuckling. After few analyses, the results show that the Dyneema has to be substitute with the carbon laminate for more than 2/3 of the arch length, but compromising the folding of the habitat. A good compromise is to put the carbon laminate for half of the arch from the hinges in the upper and lower faces of the sandwich structure.

To just understand the changes in stresses and displacement the multi-arch structure, without the equivalent Dyneema layer between the arches, is taken into account. In FIG are shown the stresses in the equivalent Dyneema layer in the lower face of the sandwich in the upper part of the arch. While in FIG are shown the stresses in the lower part of the arch where the equivalent Dyneema is replaced with carbon laminate. The carbon laminate is able to absorb the compression differently from the Dyneema. There is also an improvement in the displacement of the top of the habitat, which goes down 61 *mm*.

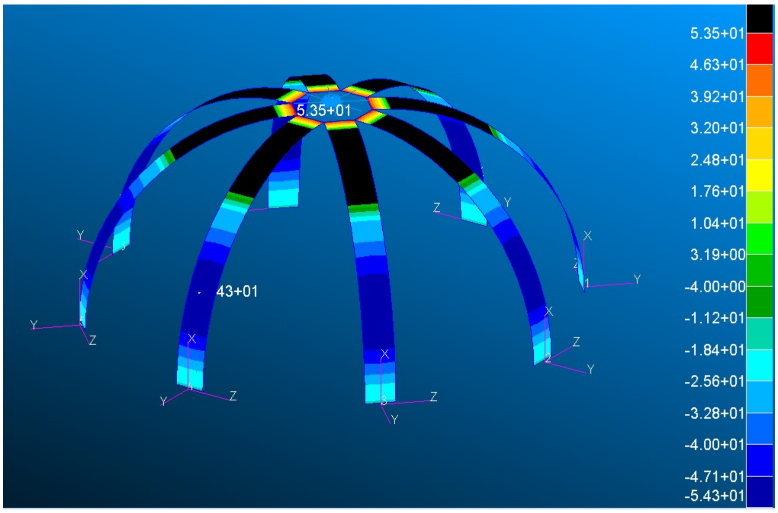

Figure 7.7: Stresses in the most stressed carbon layer.

7.5 Conclusion

This study provides a primary solution for Mars colonization, starting from a revolutionary material. The final structure, with the regolith structure around, is reported in the FIG and demonstrates that once arrived on the planet is possible to supply a place where astronauts can stay. Of course, there are a lot of problems related to the mission organization but from a structural point of view, valid solutions are feasible. The structure will need many optimizations, especially for integration with the other systems that allow the sustaining of life in the habitat.

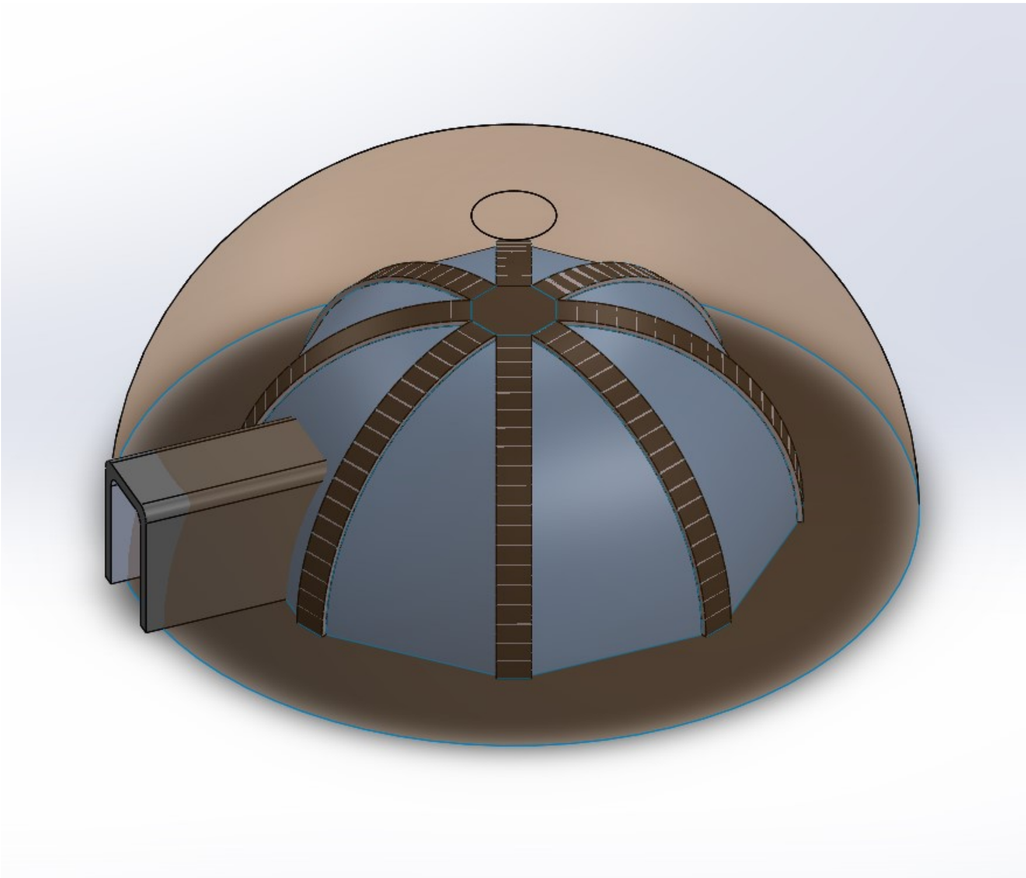

Figure 7.8: Complete structure with regolith shielding.

Bibliography

[1] Michael D. Smith. Spacecraft observationsof the martian atmosphere. 2008.

[2] Dr. David R. Williams. Mars fact sheet. URL https://nssdc.gsfc.nasa.gov/planetary/factsheet/marsfact.html.

[3] R M Haberle. Planetary atmospheres. *NASA/Ames Research Center, Moffett Field, CA, USA*, 2015.

[4] NASA. A natural source of seismic waves, meteorite impacts will be a valuable ally for insight, 2018. URL https://www.seis-insight.eu/en/public-2/martian-science/meteoritical-impacts.

[5] Robin Ramstad. The global current systems of the martian induced magnetosphere. *Nature Astronomy, www.nature.com/natureastronomy*, 2020.

[6] G. DREIBUS1 R. RIEDER H. WÄNKE, J. BRÜCKNER and I. RYABCHIKOV. Chemical composition of rocks and soils at the pathfinder site. *Space Science Reviews*, 2001.

[7] Brigitte Knapmeyer-Endrun Matt Golombek Pierre Delage Philippe Lognonné Sylvain Piqueux Ingrid Daubar Naomi Murdoch Constantinos Charalambous et al. Paul Morgan, Matthias Grott. A pre-landing assessment of regolith properties at the insight landing site. *Space Science Reviews*, 2018.

[8] Bame S. J. Feldman W. C., Ashbridge J. R. and Gosling J. T. Plasma and magnetic fields from the sun. in the solar output and its variation. *Colorado Assoc. Univ., Boulder (O. R White, ed.)*, 1977.

[9] von Rosenvinge T. T. McGuire R. E. and McDonald F. B. The composition of solar energetic particles. *Astrophys. J.*, 1986.

[10] BEVAN M. FRENCH. GRANT H. HEIKEN, DAVID T. VANIMAN. *LUNAR SOURCEBOOK A. User's Guide to the Moon.*

[11] N.F. Pissarenko. Radiation environment during the long space mission (mars) due to galactic cosmic rays. *Space Research Institute Moscow*, 1993.

[12] Robert F. Wimmer-Schweingruber Bent Ehresmann Scot Rafkin Jennifer L. Eigenbrode David E. Brinza Gerald Weigle Stephan Böttcher Eckart Böhm Soenke Burmeister Jingnan Guo Jan Köhler Cesar Martin Guenther Reitz Francis A. Cucinotta Myung-Hee Kim David Grinspoon Mark A. Bullock Arik Posner Javier Gómez-Elvira Ashwin Vasavada John P. Grotzinger MSL Science Team Donald M. Hassler, Cary Zeitlin. Measured with the mars science laboratory's curiosity rover. *SCIENCE, VOL. 343*, 2014.

[13] Saša Banjac Robert F. Wimmer-Schweingruber Lennart Röstel, Jingnan Guo and Bernd Heber. Subsurface radiation environment of mars and its implication for shielding protection of future habitats. *Journal of Geophysical Research: Planets, 125*, 2020.

[14] Haym Benaroya. *Lunar habitats: A brief overview of issues and concepts.*

[15] Sood R Milbury C Melosh HJ Howell KC Freed AM. Blair DM, Chappaz L. Determining the structural stability of lunar lava tubes. *46th Lunar and Planetary Science Conference*, 2015.

[16] Marc Mitchell Cohen. First mars habitat architecture. *AIAA 2015 Space and Astronautics Forum*, 2015.

[17] NASA. Transhab concept, 2003. URL https://spaceflight.nasa.gov/history/station/transhab/transhab_levels.html.

[18] Erin Mahoney. Beam facts, figures, faqs. URL https://www.nasa.gov/feature/beam-facts-figures-faqs.

[19] Wikipedia. Whipple shield, . URL https://en.wikipedia.org/wiki/Whipple_shield.

[20] Marlies Arnhof. Design of a human settlement on mars using in-situ resources. *46th International Conference on Environmental Systems*, 2016.

[21] NASA. Nasa's centennial challenges: 3d-printed habitat challenge, . URL https://www.nasa.gov/directorates/spacetech/centennial_challenges/3DPHab/about.html.

[22] AI SpaceFactory. Marsha. URL https://www.aispacefactory.com/marsha.

[23] Roberts M. Inflatable habitation for the lunar base. *NASAJobnson Space Center Houston*.

[24] NASA-STS-3000. Volume i - man-systems integration standards, architecture, envelope geometry for crew functions.

[25] Kriss Kennedy. *Lunar Architecture Team: Phase 2 Habitat Volume Estimation: "Caution When Using Analogs" "*.

[26] Wikipedia. Mars 500, .

[27] Claudio Leonardid Tatiana Volkovae Anne-Marlene Rüedea, Anton Ivanovb. Systems engineering and design of a mars polar research base with a human crew. *Acta Astronautica*, 2018.

[28] NASA. Mars facts, . URL https://mars.nasa.gov/all-about-mars/facts/.

[29] Pradeep Bhandari Jason Kempenaar Keith Novak Edgardo Farias, Matthew Redmond. Thermal modeling of mars ground for surface missions. *Jet Propulsion Laboratory, California Institute of Technology, Pasadena*, 2017.

[30] Federico Cumino. *Preliminary design of deployable habitat for lunar outpost made by innovative material*. Politecnico di Torino, 2020.

[31] J. Schaenzlin F. Ruess and H. Benaroya. *Structural Design of a Lunar Habitat*.

[32] United States Patent. Panel made of composite material having a layered structure. *Patent No .: US 10,583,638 B2*, Mar. 10 , 2020.

[33] Linus Fagerberg. Wrinkling in sandwich panels for marine applications.

[34] Alicia Dwyer Cianciolo Tara Polsgrove Sharon Jefferies, Tim Collins. Impacts of launch vehicle fairing size on human exploration architectures. *NASA Langley Research Center, NASA Marshall Space Flight Center*.

[35] NASA. Space launch system (sls) overview, . URL https://www.nasa.gov/exploration/systems/sls/overview.html.

[36] Composite Research s.r.l. Madflex book.

[37] Achilles Petras. *Design of Sandwich Structures.* Cambridge University Engineering Department, 1998.

[38] Igor A. Karnovsky. *Theory of Arched Structures.* Springer, 2012.

[39] Marco Gherlone. *Lecture notes of the course "Fundamentals of structural mechanics".*

Acknowledgement

At the end of this thesis, I would like to thank some people that stayed next to and supported me during this important academic career.

My incommensurable thank goes to my parents. They are simply the pillars of every achievement I obtained in these years. There will be never enough words to express my gratitude to them.

My gratitude goes to my professors Giacomo Frulla and Enrico Cestino for their constant presence in guiding me through this work. I wish all students to find professors like them, which can inspire, their life.

A special thanks to my supervisors in Co.Re., Nicola Giulietti and Eugenio Fossat, to have always encouraged all my ideas, advised me at every moment and allowed me to improve as a person and engineer.

I would like to thank my colleague Federico Cumino, that shared with me this important project and all the hard work behind it.

To my friends in Rome: Paolo Zolla, Alessia Maselli, Leandro Lucchese, Andrea Pianalto, Olena Sarabakha, Roberto Lo Bianco and last but not least Ivan Napoli. Thank you I had my best moments in my life, because I shared them with you, and even if these last years we were far away I felt your presence every day.

Thanks to my sincere friend Silvia Grasso to have supported me in my tough times and joyed for my successes in this career.

Thanks to roommates in Turin: Chiara Franco, Marco Ancona, Leonardo Altieri, Irene Cardinali, Ivette Rivas, Danilo Candela and last but not least Simone Dei Rossi. They have supported and encouraged me since we first met, making my days less tough.

Thanks to all my family in Italy and around the world, which always supported this dream of mine.

Thanks to all the other people that I met in these years, because every one of them, in a way contributed to improving me.

Torino, 13/4/2021.